ABSTRACT

Title of Dissertation:	DEVELOPMENT OF ARTIFICIAL INTELLIGENCE AUGMENTED METAL-ORGANIC FRAMEWORK-BASED SYSTEMS AND THEIR APPLICATIONS IN FOOD SECTORS
	Peihua Ma, Doctor of Philosophy, 2022
Dissertation directed by:	Professor Qin Wang
	Department of Nutrition and Food Science

Metal-organic frameworks (MOFs), a type of cutting-edge designable porous scaffolding materials attracted attention in reticular chemistry, which satisfied fundamental demands for delivery research in the past years. In this research, UiO-66 MOF family with different modifications was applied in the food delivery system and freshness monitoring.

First, zirconium (IV) chloride and benzene-1,4-dicarboxylic acid were used to make the Zr-based MOF UiO-66. Then, using a post-synthesis loading process, curcumin was encapsulated in it. The system attained a high loading capacity of 3.45 percent w/w, according to both spectroscopic and thermogravimetric measurements. X-ray diffraction (XRD), physisorption analyzer, scanning electron microscopy (SEM), and energy-dispersive X-ray spectrometer (EDS) were used to characterize the crystal structure, porosity, and morphology of the curcumin delivery system, respectively. Curcumin was shown to be released in a controlled manner in simulated

intestinal fluids using an in vitro digestion test. After 180 minutes of digestion, almost 60% of the curcumin was released.

Second, two types of curcumin-loaded UiO-66 (representative high biocompatibility and water-stable metal-organic framework) deliver systems, curcumin-loaded UiO-66 Pickering emulsion and curcumin loaded UiO-66 high internal-phase Pickering emulsions (HIPPE) were prepared, named curcmin@UiO-66 PE and curcumin@UiO-66 HIPPE, respectively. The loading capacity for the two delivery systems was reached 7.33, and 26.18% w/w respectively. All systems were characterized using X-ray diffraction (XRD), physisorption analyzer, scanning electron microscopy (SEM), and energy-dispersive X-ray spectrometer (EDS), for crystallography, morphology, physicochemical properties, with computer assistant optimization with DFT and GCMC simulation for maximum loading capacity. The result showed that these systems both exhibited extremely high surface area and porosity, as well as strong chemical and thermal stability, which demonstrated their great potential for application as a food delivery system. On this basis, the emulsion system was further optimized using the response surface method. These novel MOF nanoparticle stabilized delivery systems could be practically utilized for other bioactive components and antimicrobial agents, which would find applications in functional food, food safety, and biomedical areas in the future.

Third, incorporating or positioning multi-functional MOFs into the smart package is one of the next steps toward reticular chemistry for commercial application. Here, a cheap and versatile method to incorporate MOFs into smart food packages via generic patterning was developed. Meanwhile, deep convolutional neural networks (DCNN) were combined to form a system for monitoring food freshness that provided scent fingerprint recognition. The ice-template-based UiO-66-Br/chitosan sensor array and MOF-MMM-based UiO-66-OH/PVA sensor array

comprising 6 different dyes absorbed at MOF matrix formed scent fingerprints that were identifiable by DCNN. Several state-of-art DCNN models were trained for shrimp freshness monitoring by using 31584 labeled images and 13537 images for testing. The highest accuracy achieved was up to 99.94% by the Wide-Slice Residual Network 50 (WISeR50). MOF-MMM-based sensor array showed a similar result where chicken freshness estimation achieved up to 98.95%. These platforms are intuitive, fast, accurate, and non-destructive, enabling consumers to monitor food freshness.

DEVELOPMENT OF ARTIFICIAL INTELLIGENCE AUGMENTED METAL-ORGANIC FRAMEWORK-BASED SYSTEMS AND THEIR APPLICATIONS IN FOOD SECTORS

by

Peihua Ma

Dissertation submitted to the Faculty of the Graduate School of the
University of Maryland, College Park, in partial fulfillment
of the requirements for the degree of
Doctor of Philosophy
2022

Advisory Committee:
Dr. Qin Wang, Professor, Chair
Dr. Rohan V. Tikekar, Associate Professor
Dr. Liangli Yu, Professor
Dr. Yifei Mo, Associate Professor
Dr. Yaguang Luo, Research Food Technologist

© Copyright by
Peihua Ma
2022

Acknowledgements

In the last parts of my dissertation, I would like to write my thanks to all the people who contribute or helps me on the way of achieve doctoral graduation. I would like to acknowledge and give my warmest thank you to my supervisor, Dr. Qin Wang, for providing guidance and feedback throughout this project. I would also like to thank my committee members, Dr.Yaguang Luo, Dr.Liangli Yu, Dr.Yifei Mo, and Dr.Rohan V. Tikekar, for letting my defense be an enjoyable moment, especially during the difficult pandemic period. Meanwhile, I would like thanks to my friends on campus who help and support me during the pandemic. I would like to thank Dr. Jinglin Zhang, Dr. Zi Teng, and Dr. Boce Zhang who graduated from Dr. Wang's lab before and provide me with tons of help and instructions both life and academic. Next, my roommate and collaborators, including Zhi Zhang (food science), Xinyang Huang, Junheng Tao (physics), Yuxun Guo (physics), Dr. Zeshu Zhang (BME), Dr.Ning Yu (computer science), Dr. Zhikun Zhang, Dr. An Li (robotic), Dr.Lau Chun Pong (computer science), Shawn Tsai (food science), and Yuan Zhang, Wenhao Xu in the department of chemical engineering, who help me a lot in material preparation and test, I have to say that this multidiscipline work could not achieve without all your help. Besides, I would like to write my special thanks to the professors who provide your knowledge and instruction during my doctoral learning period. Dr. Yuang Fang, Dr. Yanxiang Gao, Dr. Like Mao Dr. Lin Shen, Dr. Hao Zhang, Dr. Hongchao Zhang, Dr. Dong Yang from China Agriculture University, Dr. Jiping Sheng in Renmin University, Dr. Fuguo Liu from Northwest A&F University, Dr. Shuai Chen from Wuhan University, Dr. Yongguang Guan and Dr. Yang Wei from

Shanghai Jiaotong University, Dr. Fang Zhang from Ocean University of China, Dr. Hui Huang from Jilin University, Dr. Ping Lui from Xihua Univeristy and Dr. Pengqun Kuang from Linyi University, And also Dr. Cheng Gong, Dr. Liangbing Hu and Dr. Dongxia Liu on UMD campus provided free equipment for my research. In addition, I would also thank to all my friends around the world, who traveled or played games with me during the past years and waste time together every month, Jiahua Chang in New Zealand, Xilin Lu and Xinyi Wang in Australia, Pengyu Zhou, Xin Yuan Si Liu, Qinghan Zeng, Xiangyi Wu, Xi Yang and Yao Lu in China, Xiaofeng Hong in Hongkong, Mazen Obaid and Sami Obaid from Saudi, Yanqiao Yang Chang Liu and Haoyuan Jiang from German, Yangpeng Liu, Junyi Xiao from France. Yuluo Chen from Canada and last are my friends in the U.S, including Xiaoxue Jia, Kevin Tarwa, Si Fan, Zhenxun Liu, Ke Gong, Chenyu Mao, Shihangyin Zhang, Jiahao Zhan, Yingyue Zhu, Cheung Paul, Kaihui Song, Ying Li. In the end, I cannot miss the thanks to the people in USDA-ARS, Jaspreet Ahuja, Dr. Ying Li, Dr. James Harnly, Kyle McKillop, Dr. Pamela Pehrsson and Dr. Bin Zhou. I would also like to give special thanks to my family for their continuous support and encouragement when undertaking my research and writing my project.

All in all, this tiny work certainly depends on the solitary struggle of individuals, but it is also important to consider the progression of history, which was created by others together. Life is a box of chocolate given by destiny. In this box of chocolate, it contains arduous and mediocrity, frustration, and glory. So, enjoy first and share with others. As when I saw the trouble our world was in, I knew I couldn’t stand by and watch any longer.

Table of Contents

Acknowledgements ii
Table of Contents v
List of Tables viii
List of Figures x
Chapter 1 Introduction 1
1.1 Background of Metal-organic frameworks (MOFs) 1
1.1.1 Overview of MOFs 1
1.1.2 Synthesis of MOF nanoparticles 2
1.1.3 MOF delivery systems 3
1.1.4 MOF and polymer-based mixed-matrix system 6
1.2 Background of UiO-66 and its derivatives 8
1.2.1 Overview of UiO-66 family 8
1.2.2 Application of UiO-66 and its derivatives 9
1.3 Introduction of Pickering emulsion 11
1.3.1 Overview of Pickering emulsions 11
1.3.2 High internal phase Pickering emulsions 13
1.3.3 Key factors for Pickering emulsion stabilization 16
1.4 The colorimetric sensor array 17
1.4.1 Structure and principle of the colorimetric sensor array 17
1.4.2 Data analysis and signal extraction of the colorimetric sensor array 18
1.4.3 Application of colorimetric sensor arrays in the food area 19
1.5 Machine learning and its application in the food area 20
1.5.1 Major categories of machine learning methods 20
1.5.2 Machine learning application for genomic data 22
1.5.3 Machine learning application for computer vision 23
1.5.4 Machine learning application for natural language processing 24
1.6 Research objectives 25
1.6.1 Development of UiO-66 derivatives-based food delivery systems. 25
1.6.2 Development and optimization of UiO-66 derivatives-based emulsion systems for food application. 25
1.6.3 Development and optimization of UiO-66 derivatives-based colorimetric sensor array based on deep learning for food package. 26
Chapter 2 UiO-66 nanoparticles as a carrier for curcumin delivery 27
2.1 Abstract 27
2.2 Introduction 27
2.3 Material & methods 29
2.3.1 Material 29
2.3.2 UiO-66 property simulation 29
2.3.3 Synthesis of UiO-66 30
2.3.4 Preparation of curcumin-loaded UiO-66 30
2.3.5 Porosity and surface area of MOFs 31
2.3.6 Crystal structure of MOFs 31
2.3.7 Morphology of MOFs 32
2.3.8 Thermogravimetric analysis (TGA) 32

2.3.9 Loading capacity (LC) of MOFs 32
2.3.10 In vitro digestion 33
2.3.11 Statistical analysis 34
2.4 Results and discussion 35
2.4.1 Computer simulation of the characteristic of UiO-66 and Cur-UiO-66 35
2.4.2 Porosity and surface area 36
2.4.3 Crystal structures 38
2.4.4 Microstructure 39
2.4.5 Thermogravimetric analysis (TGA) 40
2.4.6 Loading capacity (LC) 41
2.4.7 In vitro digestion 43
2.5 Conclusion 45
Chapter 3 Development of UiO-66 nanoparticles as a stabilizer for curcumin loaded Pickering emulsion delivery system 46
3.1 Abstract 46
3.2 Introduction 47
3.3 Materials & Method 49
3.3.1 Computational calculation 49
3.3.2 Synthesis of UiO-66-NH_2 51
3.3.3 Characterization of UiO-66-NH_2 51
3.3.4 Emulsion preparation 53
3.3.5 Characterization of UiO-66-NH_2 Pickering emulsion 54
3.3.6 Statistical analysis 57
3.4 Results and Discussion 57
3.4.1 Characterization of UiO-66-NH_2 nanoparticles 57
3.4.2 Pickering emulsion stabilized by UiO-66-NH_2 62
3.4.3 Loading capacity of MOF-HIPPE system 68
3.5 Conclusion 70
Chapter 4 Optimization curcumin loaded UiO-66 Pickering emulsion delivery system 72
4.1 Abstract 72
4.2 Introduction 72
4.3 Materials and methods 76
4.3.1 Materials 76
4.3.2 Experimental design 76
4.3.3 Synthesis of UiO-66-NH_2 77
4.3.4 Emulsion Preparation 77
4.3.5 Encapsulation properties 79
4.3.6 Statistical analysis 79
4.4 Results and discussion 79
4.4.1 Mutual effect of parameters 81
4.4.2 Optimization of synthesis conditions 83
4.3.3 Model validation 85
4.5 Conclusion 86
Chapter 5 Development integrated portable shrimp-freshness prediction platform based on UiO-66-loaded ice-template colorimetric combinatorics 88

5.1 Abstract 88
5.2 Introduction 89
5.3 Materials & Methods 91
5.3.1 Materials 91
5.3.2 Computational methods 92
5.3.3 Preparation of UiO-66 and UiO-66-Br 93
5.3.4 Ice-templated Dye@chitosan/UiO-66 monoliths 95
5.3.5 Calculation of amine gas concentration. 96
5.3.6 Material characterization 96
5.4 Results and discussion 100
5.4.1 Identification of materials for selective adsorption 100
5.4.2 Sensor array validation on response to VAC standards 102
5.4.3 Characterization of sensor arrays 109
5.4.4 Deep learning-enabled freshness recognition 112
Chapter 6 Development integrated portable chicken-freshness prediction platform based on UiO-66-loaded MOF-MMM colorimetric combinatorics 119
6.1 Abstract 119
6.2 Introduction 120
6.3 Materials & methods 122
6.3.1Materials 122
6.3.2 Synthesis of UiO-66 and UiO-66-OH 123
6.3.3 Synthesis of dye@UiO-66/PVA and dye@UiO-66-OH/PVA MMM 123
6.3.3 Calculation of amine gas concentration. 124
6.3.4 Scanning electron microscope (SEM) 124
6.3.5 Fourier transform infrared (FT-IR) spectrometry 125
6.3.6 UV−Vis Spectrophotometry 125
6.3.7 Thermogravimetric analysis (TGA) 125
6.3.8 Crystal structure of MOFs 126
6.3.9 Particle size and polydispersity index (PDI) 126
6.3.10 Surface charge 126
6.3.11 Determination of swelling index 126
6.3.12 Solubility Determination for MOF/PVA-MMM 127
6.3.13 Total volatile basic nitrogen (TVB-N) measurement 127
6.3.14 Circular region of interest (CROI) identification 128
6.3.15 Database preparation and images collecting for DCNN training 128
6.3.16 Network architecture 129
6.3.17 Statistical analysis 130
6.4 Result and discussion 130
6.4.1 MOF-MMM materials identification 130
6.4.2 Synthesis and morphologies of UiO-66-OH/PVA sensor array 133
6.4.3Validation and sensitivity of MOF-MMM in standard conditions 141
6.4.4 Deep learning-enabled pattern recognition using DCNN 143
Summary and Future Perspectives 148
Bibliography 150

List of Tables

Table 2-1 Computer simulation output of UiO-66 characteristics

Table 3-1 The 3-factor Box-Behnken design for MOF-HIPPE system

Table 3-2 Computer simulation output of UiO-66-NH2 characteristics

Table 3-3 Fitting results of emulsion rheology analysis based on Ostwald–de Waele model

Table 4-1 Box-Behnken design (3-level-4-factor) for curcumin-loaded Pickering emulsion delivery system and response surface analysis of experimental data

Table 4-2 Analysis of variances for the variables in the preparation of the Pickering emulsion pertaining to response LC and EE

Table 4-3 Analysis of variances for preparation of the delivery system by a joint test

Table 4-4 Model parameters coefficients (and their associated p-value between brackets) for the prediction of the LC and EE of curcumin. Coefficients have to be used with coded levels for each factor

Table 5-1 The list of biocompatible chromophore dyes on the colorimetric sensor array

Table 5-2 The comparison of the range of concentration and equilibrium time between the three kinds of colorimetric sensor arrays

Table 5-3 Comparison between UiO-66 and UiO-66-Br nanoparticles

Table 5-4 The accuracy comparison results between the ED value method and four state-of-art DCNN models

Table 6-1 The list of biocompatible chromophore dyes on the colorimetric sensor array

Table 6-2 Relative binding energy for NH3, methylamine (MA) and trimethylamine (TMA) in UiO-66 as well as functionalized UiO-66 materials determined from periodic PBE-D2 calculations

Table 6-3 Particle size and zeta-potential for UiO-66 and UiO-66-OH particles

Table 6-4 The accuracy comparison results between the ED value method and four state-of-art DCNN models

List of Figures

Figure 1-1 (a) Schematic representation of molecular emulsifiers adsorbed onto the oil-water interface to form emulsion system, (b) particles adsorbed onto the oil-water interface to form Pickering emulsion, and (c) three stabilization mechanisms of Pickering emulsion: interfacial film, network structure in the continuous phase, and depletion interaction

Figure 1-2 (a) Schematic illustration of particle adsorption to the interface by depletion attraction. (b) Photographs of compared emulsions (0.18 vol% of 1 mm-silica particles) formed with the presence of PEG (10,000 g mol 1, left) and the absence of PEG (right), taken after several hours from voltex emulsification (B3,000 r.p.m.). Here, f is the oil fraction of the initial oil–water mixture before emulsifying. Scale bar, 1 cm. (c) Photograph of f ¼ 0.6 emulsion (0.18 vol% silica particles) with oil-soluble fluorescence dyes and its confocal micrograph. Scale bar, 100 mm. (d) Photograph of f ¼ 0.8 high internal phase Pickering emulsion (0.18 vol% silica particles) and its confocal micrographs. Scale bar, 100 mm. (e) Confocal microscope image of fluorescently labelled silica particles (1.08 vol% silica particles) well adsorbed on an oil droplet surface by depletion attraction. Scale bar, 30 mm. All emulsions and HIPPEs (b–e) are produced by the vortexing method

Figure 1-3 The analogy between the biological and colorimetric sensor arrays' systems

Figure 1-4 Examples of machine learning models. (a) A decision boundary plot of k-means clustering with three clusters, with new samples being grouped to a cluster by the colored region it lands on. (b) A line dividing two classes in a support-vector machine with a certain margin. w contains the trainable parameters, and x stands for

the vector representation of a sample. (c) A decision tree with five features. A sample is classified into a certain class following the red arrow. (d) A neural network with two hidden layers; the arrow stands for a connection between units, with transparency indicating the connection strength

Figure 2-1(a)(b) a view of the UiO-66 porous structure; (c)(d) Monte Carlo simulation of nitrogen adsorption site distribution

Figure 2-2 N2 adsorption isotherms at 77 K on UiO-66, Cur-UiO-66 and simulate UiO-66

Figure 2-3 Powder X-ray diffraction (PXRD) patterns of synthesized UiO-66 and Cur-UiO-66 compared with the simulated one for UiO-66

Figure 2-4 SEM images of (a) UiO-66; (b) Cur-UiO-66, (Bar scale = 1 μm)

Figure 2-5 TGA curves of Curcumin, UiO-66 and Cur-UiO-66 under dry N2 gas

Figure 2-6 UV-visible absorption spectra of curcumin in the presence of UiO-66 suspended in ethanol

Figure 2-7 Curcumin release from Cur-UiO-66 during the first 3 hours of in vitro digestion

Figure 3-1 (a) A simulation view of the UiO-66 porous structure Carbon: Grey; Oxygen: Red; Zirconium: Bluegreen; (b) Molecular electrostatic potential maps of UiO-66; (c) Molecular electrostatic potential maps of UiO-66-NH2

Figure 3-2 (a) PXRD patterns of UiO-66-NH2; (b) N2 adsorption isotherms at 77 K on UiO-66-NH2; (c) Thermogravimetric analysis of UiO-66-NH2

Figure 3-3 Particles size distribution of UiO-66-NH2(Top); zeta-potential of UiO-66-NH2 at different pH value (Bottom); (b) SEM images of UiO-66-NH2; (c) WAC of UiO-66-NH2

Figure 3-4 (a) Visual appearance of MOF stabilized emulsions at different O:W ratios. (b) The stabilization of HIPPEs that contain various concentrations of PEG and UiO-66-NH2 particles. Red dot: unstable emulsion; Brown dots: emulsion only; Green dots: HIPPE

Figure 3-5 (a) Apparent viscosity of Pickering emulsions at different O:W ratios. (b) Storage modulus (G′) and loss modulus (G″) as a function of angular frequency for the stabilized Pickering emulsions

Figure 3-6 SEM images of MOF-HIPPE droplets with the theoretical model. The left figure showed the theoretical Pickering droplet model and the right was image from SEM. Middel upper image showed the droplet interface from internal view and middle bottom image showed the droplet interface from outer view

Figure 3-7 Representative confocal laser scanning microscopy (CLSM) images of the HIPPE in different regimes. Upper three images was imaged by CLSM from representative regime and the bottom three images was mapping to their theoretical model

Figure 4-1 Response surface plot showing the effect of ultrasonic power and MOF content on (a) LC; (b) EE

Figure 4-2 Prevision profiler's outputs after maximization of the desirability function for LC and EE: Optimum emulsion preparation conditions are given while curves

show how changes of factors' level affect the response. Greenline for 95% confidence interval and re

Figure 4-3 Validation of the model with experimental data

Figure 5-1 Fabrication of ice-template colorimetric sensor array with DCNN

Figure 5-2 (a) Powder X-ray diffraction (PXRD) patterns of synthesized UiO-66 and UiO-66-Br compared with the simulated one for UiO-66; (b) SEM images of UiO-66 nanoparticles; (c) SEM images of UiO-66-Br nanoparticles

Figure 5-3 (a) The heat map of relative binding energy for four selected amine gases in functionalized UiO-66 materials determined from periodic PBE-D2 calculations; (b) Material Studio simulation indicates the center of mass (COM) probability distribution of the adsorbed NH3 on UiO-66-Br crystal.

Figure 5-4 (a) Photoed images of color changes of Dye@UiO-66-Br/Chitosan sensor arrays exposed to NH3, MA, and TMA as gas concentration increased from 20 to 320 ppm; (b) Photoed images of color changes of Dye@UiO-66/Chitosan and Dye@Chitosan sensor arrays exposed to NH3.

Figure 5-5 Boxplot of the ED distribution of different dyes based on UiO-66-Br/Chitosan for NH3, MA, TMA at different gas concentrations (from 20 to 320 ppm, n = 10)

Figure 5-6 (a) Clusters of three sensor array systems: Dye@UiO-66-Br/Chitosan (red), Dye@UiO-66/Chitosan (blue), Dye@chitosan (yellow) via 2D PCA score plot. The color shade of the dot represents the concentration of ammonia gas concentration. The two dimensions plotted only encompass 44.73% of the total variance; (b) PCA score plot, the number of eigenvectors (i.e. principal components)

need to reach cumulative percentage (i.e. total variance); (c) Cluster tree produced by hierarchical cluster analysis showed three colorimetric sensor array systems can be distinguished treated by different ammonia gas concentration
Figure 5-7 (a) SEM image of ice-templated methyl red@UiO-66-Br/Chitosan monolith with EDS result (left); and UiO-66-Br nanoparticles (right); (b) Infrared spectra of UiO-66 and UiO-66-Br nanoparticles (left). Infrared spectra of chitosan monoliths and UiO-66-Br/ Chitosan monoliths (right)
Figure 5-8 (a) The shrimp with sensor array images database structure. The database contained 31584 images for model training and 13537 images for testing labeled with reference TVB-N result; (b) The DCNN models were used for shrimp freshness classification
Figure 5-9 The pattern change of TVB-N content in Penaeus monodon during cold storage
Figure 5-10 (a) The relation between DCNN models training loss with the increase of training epoch; (b) The confusion matrix of four DCNN models
Figure 6-1 X-ray diffraction (XRD) patterns of synthesized UiO-66-OH@PVA MMM, UiO-66 and UiO-66-OH compared with the simulated one for UiO-66
Figure 6-2 Fabrication and characterization of colorimetric sensor array. (a) Schematic of sensor array in 3D printing mold. Each pore filled with six types of dyes with UiO-66-OH/PVA solution. (b) Schematic showing the fabrication of dye@UiO-66-OH/PVA sensor array. UiO-66-OH are cross-linked with PVA via hydrogen bond, and dye was adopted to the surface of UiO-66-OH. (c)Scanning electron microscopy image of UiO-66-OH NPs and pH2 (left), UiO-66-OH NPs at pH 7(middle) and UiO-

66-OH/PVA film. (d) Infrared spectra of UiO-66 NPs, UiO-66@PVA film and UiO-66-OH@PVA film. (3) Spectral scanning of six different dye loaded in UiO-66-OH@PVA film. Scanning range from 300-650 nm

Figure 6-3 Thermogravimetric analysis, UiO-66 and UiO-66-OH NPs (left) and UiO-66/PVA and UiO-66-OH/PVA (right)

Figure 6-4 Swelling index (%) and solubility of PVA film with two MOF-MMM film in an aqueous environment

Figure 6-5 (a) Photoed images of color changes of dye@UiO-66-OH/PVA sensor array exposed to methylamine gas as gas concentration increased from 40 ppm to 320 ppm. (b) Schematic of Hough transform ROI extraction processing

Figure 6-6 Boxplot of the ED distribution of different dyes based on UiO-66-OH/PVA MOF-MMM for NH3, MA, TMA at different gas concentrations (from 40 to 320 ppm, n = 10)

Figure 6-7 (a) The pattern changes of TVB-N content in chicken breast sample during cold storage. (b) The chicken breast sample with sensor array images database structure. The database contained 4492 images for model training and 1927 images for testing labeled with reference TVB-N result; (c) The DCNN models were used for chicken breast freshness classification

Figure 6-8 The confusion matrix of four DCNN models

Chapter 1 Introduction

1.1 Background of Metal-organic frameworks (MOFs)

1.1.1 Overview of MOFs

The creation of very porous materials, such as metal-organic frameworks (MOFs), zeolite, and covalent organic frameworks (COFs), has lately made a breakthrough, with MOFs drawing the most interest(Horcajada et al., 2010; Moghadam et al., 2017). As defined, MOF is a material "*with a transition metal bonded to an oxygen or nitrogen atom via a polymeric bond*". The basic guideline of "*polymeric bonds*" is "*bonds between repeating units*"(Horcajada et al., 2010). The structure of MOF can be seen as organic linkers that connect vertices or inorganic nodes in the framework consisting of metal ions. Organic linkers, which often include phosphonate, carboxylate, pyridyl, imidazolate, or other azolate functional groups, connect the nodes, or clusters named secondary building units (SBUs), via coordination bonds. Bi-, tri-, and tetratopic organic linkers can be used, although they are not obligatory(Ji et al., 2020). A broad number of framework topologies may be created by combining various linkers with metal nodes or SBUs with variable shapes and connectivities. SBUs that define or encompass structural nodes that are made up of metal ions and non-metals (usually oxygen or nitrogen) provide complementary variety in topology, connection, and function. In these units, the number of metal atoms varies from one to eight or more. Because of their ease of tuning, atomic-level structural uniformity, compositional (elemental) variety, and high porosity, MOFs differ from other porous materials such as activated carbon, porous organic polymers, and zeolites(Xu et al., 2019). MOFs have gotten a lot of attention in the last two decades because they can be used to make a wide range of visually appealing structures that can be used in a number of sectors, including storage,

separation, catalysis, and biomedical applications or sensor materials, based on the pore size, shape and the host-guest interactions involved(Qiu et al., 2014).

Howarth et al. published a highly cited review on the physicochemical properties of MOFs, which summarized the progress of high stability MOFs, such as chemical stable MOFs, thermal stable MOFs, hydrothermal stable MOFs, and mechanical stable MOFs, which were typically perceived as problematic comparing to industrially applied relevant zeolites(Howarth et al., 2016). MOFs, as a type of porous material, have progressed from being "typically fragile" and "generally moisture-sensitive" to being practically universally designable to survive extreme physical and chemical conditions(O'Keeffe & Yaghi, 2012). This modification will undoubtedly hasten the research and application of MOFs to face scientifically and technologically critical challenges in novel ways.

1.1.2 Synthesis of MOF nanoparticles

The term "design" has been used frequently in the context of MOF synthesis, although it is controversial(Stock & Biswas, 2012). The term and its ramifications have aided in the advancement of the area. Comprehending alternative topologies, the activity of multitopic organic linker molecules, as well as typical metal coordination environments or the formation circumstances of common inorganic building blocks (also known as bricks) aids in understanding and directing synthesis operations. A thorough understanding of the principles behind MOF synthesis is critical for customizing structures with the required chemical and physical characteristics (Giannakoudakis & Bandosz, 2019). Many investigations on MOFs using diverse synthetic techniques have been published during the last two decades. Stock and Biswas published an excellent review in 2012 for a full introduction to MOF synthesis (Stock & Biswas, 2012). The review discussed a variety of MOF synthesis methods, including the

traditional solvothermal/hydrothermal approach as well as mechanochemical and sonochemical synthesis (e.g. microwave, ionothermal, interfacial assembly methods, etc). The porosity of the MOF as a result of its synthesis was typically used to measure its efficacy, with larger porosity suggesting better synthetic conditions. The creation of MOFs has been proved to be possible using methods based on coordination chemistry(Düren et al., 2009). This contains both the precursor and in situ linker synthesis methods.

MOFs have traditionally been synthesized using hydrothermal or solvothermal synthesis techniques on small scales, with reaction time ranging from several hours to days(Safaei et al., 2019). Ren et al. published a review on MOF pilot-scale manufacturing that covered typical MOFs e.g. MIL101(Cr), HKUST-1, UiO-66, and MOF-5, among others. The methods employed to make these MOFs differed from the standard solvothermal synthesis performed in the lab (Ren et al., 2017). They explored the regulation of MOF shape and particle size, the formation of MOF membranes and thin films, and the creation of MOF-based composites in addition to synthetic approaches. Concepts from other study areas, particularly zeolite chemistry, have made their way into MOF synthesis(Férey, 2008). When compared to zeolites, MOFs provide far more opportunities. Because of the wide spectrum of organic linkers available, certain positively and negatively charged framework compounds have been developed. MOFs with zwitterionic linker molecules can therefore be envisioned. Furthermore, using charged linkers in conjunction with structure-directing agents might lead to the identification of novel molecules.

1.1.3 MOF delivery systems

In the past decades, MOFs have been highlighted in the field of controllable drug release. Individual MOFs, stimuli-responsive MOFs, and multifunctional MOFs make up these drug nanocarriers and theragnostic platforms(Orellana-Tavra et al., 2015; Wu & Yang, 2017).

Considering the need for food delivery systems, only individual MOFs, stimuli-responsive MOFs delivery systems are reviewed below.

The first report of the MOF-based drug delivery system was published by Ferey and co-workers in 2006(Horcajada et al., 2006). They applied two low toxicity and high water stability Cr-based MOFs, named MIL-100 and MIL-101, to load ibuprofen (hereafter IBU). The structure of MIL-100 series MOF nanoparticles are formed by trimers of metal octahedra, here are Cr nodes, with a dicarboxylic acid. The result showed remarkable IBU loading capacity and encapsulation efficiency, up to 35% w/w for IBU@dehydrated MIL-100 and 140% w/w of IBU@dehydrated MIL-101, respectively. The large cage size of MIL-101 and its strong interaction with IBU led to controlled release up to 6 days when tested in simulated body fluid at 37^{o}C(Horcajada et al., 2008). However, taking into consideration the toxicity of chromium compounds, various low toxicity MOFs have been applied for medicine delivery. Among them, research has been focused on three groups of MOF families, Fe-based MOFs, Zn-based MOFs, and Zr-based MOFs. The first Fe-based MOF delivery system was reported in 2008(Horcajada et al., 2008). MIL-53(Fe), which chelating by trans chains of Fe (III) octahedra and terephthalate anions, was applied to adsorb IBU in hexane solution and achieved a loading capacity of 20% w/w(Horcajada et al., 2008). Zn-based MOFs, including Zn-TATAT, Zn_2(1,3-bdc)$_2$(dabco), and Zn-CDDB have also been tested for IBU loading and targeting in different cells lines (e.g. J774, $HepG_2$, HuH_7, and Ovarian cancer cells). The loading capacity was in the range between 15% to 53% w/w with insignificant acute toxicity. Recently, Zr-based MOFs, especially UiO-66 (named by the University of Oslo) have received increasing attention. UiO-66 is an example of eminent MOFs, which can be effortlessly synthesized from various conditions(Cavka et al., 2008). Cavka et al. first reported the synthesis of UiO-66 in 2008, which gradually attracted much attention

due to its high thermal, chemical, and mechanical stability. It was prepared by a solvothermal reaction of $ZrCl_4$ with terephthalic acid (H_2BDC) in dimethylformamide (DMF) at 120°C for 24 h(Cavka et al., 2008). The as-prepared UiO-66 particles consisted of intergrown cubic crystals of ca. 1−2 μm, and it was determined that UiO-66 could be consistently duplicated as it had the thermodynamically favored structure (Winarta et al., 2019). IBU, caffeine, and 5-fu were encapsulated by simple immersion and reached up to 27% w/w of loading capacity, indicating UiO-66 was promising carriers for these drugs (Winarta et al., 2019).

According to the requirement of an ideal delivery system, smart materials, especially stimuli-responsive materials have aroused extensive attention. Generally, stimuli-responsive MOF delivery systems can be further divided into two categories: single-stimulus- and multiple-stimuli responsive MOFs (Jarai et al., 2020). The stimuli here could be pH, temperature, light, pressure, ions strength, and magnetic field. pH-responsive MOFs are the most frequently studied in bio-applications, particularly for cancer therapy and digestive system therapy (Liu et al., 2017). This is because of the sensitivity of coordination bonds to pH, acidic tumor microenvironment, and different pH environments in the gastrointestinal tract. Also, considering that this paper focuses on the future application of MOF in the food field, the focus here is only on the pH-stimulated controlled delivery system. One of the most classic designs of the pH-stimuli MOF delivery system was to select pH-response organic ligands to fabricate MOF nanoparticles. For example, Huang and co-workers reported a Fe-1,1’-(1,4-butanediyl)bis(imidazole) MOF by deposition method (Gao et al., 2013). DOX was loaded in the delivery system by in situ encapsulation and as expected, the DOX could be released in a low pH environment due to the sensitivity of the ferrous ions coordination bond to the acidic environment. Furthermore, to protect the fast decomposition of carrier material for effective

control release of DOX, a layer of silica was coated on the surface of MOF nanoparticles and conjugated with folic acid for targeted delivery. The result proved that Fe-based MOF carriers demonstrated a pH-dependent release behavior and significant anticancer ability *in vivo* (Fu et al., 2017). Another strategy to develop a pH-stimuli delivery system was to leverage the natural drug anchorages of MOF particles. Shi and coworkers utilized Zr-O clusters natural anchorages achieved control release of alendronate (Zhu et al., 2014). The high loaded capacity of alendronate was achieved up to 106% w/w due to the strong complexation of Zr-O-P bonds. However, with the environment pH value decreasing, the complexation of Zr-O-P bonds turns weak and 59% loaded alendronate released during pH value of PBS buffer decreased from 7.4 to 5.5 in 37ºC, thus achieving a pH-stimuli release behavior.

Besides the pH-stimuli delivery system, the temperature-stimuli delivery system also shows interesting applications in the food industry (McClements & Li, 2010). Temperature-stimuli delivery systems, in general, are materials that are sensitive to minor temperature changes in the room temperature to body temperature range (Roy et al., 2013). Sada and coworkers reported a switchable poly(N-isopropyl acrylamide) (PNIPAM) UiO-66 delivery system, which loaded with resorufin, caffeine, and procainamide and then controlled release from 25ºC to 40ºC. PNIPAM exhibited hydrophilicity and tends to dissolve in water when the environment is below 32ºC and forms aggregate when above (Nagata et al., 2015). As expected, drug release increased at 25°C and almost stopped at 40°C, suggesting that controlled release is driven by temperature changes (Nagata et al., 2015).

1.1.4 MOF and polymer-based mixed-matrix system

Since MOFs have been identified as an outstanding material with tremendous promise due to their high porosity, customizable pore networks, and chemical flexibility of their

structures, it has been introduced to prepare mixed matrix membranes, called MOF-MMM. The controllable molecular sieving property allows MOF-MMM for better performance or the avoidance of flaws at the polymer/particle interface (Dechnik et al., 2017). Incorporating MOF particles into polymers might be a potential strategy to address the trade-off between polymer membrane permeability and selectivity and the brittleness of inorganic films (Ghalei et al., 2017). The first report on MOF-MMM manufacturing was published in 2004. Yehia and colleagues integrated a copper(II) biphenyl dicarboxylate–triethylenediamine MOF into poly(3-acetoxyethylthiophene) (PEAT) matrix for gas separation, and the membrane showed enhanced CH_4 selectivity (Yehia et al., 2004). Since then, a slew of MOF MMMs with promising results have been reported. According to their shapes, MOF MMMs may be divided into symmetric dense membranes and asymmetric membranes. Polymer membranes with scattered MOF particles make up symmetric dense MOF-based MMMs. Asymmetric membranes are made of a thin polymer layer with MOF fillers that is supported by porous support (Zhang et al., 2016).

To build symmetric dense MOF MMMs, the general development method was a film-casting method (solvent-casting method). MOF particles were first dispersed in a solvent by stirring and/or sonication, and then polymer powders or solvent were added to generate a homogeneously dispersed MOF/polymer solution in a typical process. The polymer-MOF solution was thereafter cast on a flat surface, commonly using a doctor blade system, and the solvent was allowed to evaporate before being heated under vacuum or freeze-dried to remove the solvent completely. The skin layer in an asymmetric membrane serves as a selective function in most circumstances, while the substrate serves as mechanical support. Asymmetric membranes have lower gas resistance and larger particle loadings in the top layer compared to symmetric membranes. The phase inversion approach, which involves casting a polymer/MOF

solution onto the support followed by a solvent exchange procedure, is commonly used to create flat asymmetric membranes (Kalaj et al., 2020).

1.2 Background of UiO-66 and its derivatives

1.2.1 Overview of UiO-66 family

UiO-66 is an example of an eminent MOF, which can be effortlessly synthesized from various conditions (Wu & Yang, 2017). In 2008, Lillerud et al. published the first report on the synthesis of UiO-66, which drew a lot of attention due to its great chemical, thermal, and mechanical stability. A solvothermal reaction of $ZrCl_4$ with terephthalic acid (H_2BDC) in dimethylformamide (DMF) at 120°C for 24 hours was used to make it. The UiO-66 particles were made up of intergrown cubic crystals with a diameter of around 120 nm. Because UiO-66 had the thermodynamically preferred structure, it was confirmed that it could be reliably replicated (Cavka et al., 2008). Even if the $H_2BDC/ZrCl_4$ ratio was in the range of 0.5 to 3, or the reactant concentrations were tripled, crystalline UiO-66 samples could be formed. A family of isoreticular MOFs of UiO-66, UiO-66-X (consisting of UiO-66-Br, UiO-66-2,5-Br_2, UiO-66-NH_2, UiO-66-2,5-NH_2, UiO-66-NO_2, UiO-66-F, UiO-66-2,5-F_2, UiO-66-F_4, UiO-66-1,4-Naph, UiO-66-Cl, UiO-66-2,5-Cl_2, UiO66-I, UiO-66-CH_3, UiO-66-2,5-$(CH_3)_2$, UiO-66-CF_3, UiO-66-2,5-$(CF_3)_2$, UiO-66-OH, UiO-66-2,5-$(OH)_2$, UiO-66-OCH_3, UiO-66-COOH, UiO-66−2,5-$(COOH)_2$, UiO-66-$(COOH)_4$, UiO-66-2,5-$(OMe)_2$, UiO-66-SO_3H, and UiO-66-2,5-$(OCH_2H3)_2$) have been synthesized by reaction of $ZrOCl_2 \cdot 8H_2O$ or $ZrCl_4$, and the functionalized H_2BDC-X ligands under similar reaction conditions (Winarta et al., 2019). In a separate study, Schaate et al. showed that adding a modulating agent to the synthesis of UiO-66 and its derivatives, such as benzoic or acetic acid, improved the crystallinity of the products and the reproducibility of the reactions, resulting in the formation of large isolated crystals with clear morphology (Schaate et

al., 2011). By varying the quantity of acetic acid modulator in the reaction mixture and modifying the reaction period, Wu et al. discovered that severely faulty UiO-66 (missing-linker defects) could be generated. Pore volumes in the faulty UiO-66 samples ranged from 0.44 cm^3/g to 1.0 cm^2/g, with BET surface areas of 1000-1600 m^2/g (Wu et al., 2013). Katz et al. discovered that adding HCl to a $ZrCl_4$ and H_2BDC reaction in DMF at 80°C increased the synthesis of UiO-66 at lower temperatures and shorter reaction periods (Katz et al., 2013). The synthesis was also successfully scaled up 50 times. The produced sample of UiO-66's BET surface area was compared to a theoretical plot, revealing that the synthesized UiO-66 nanoparticles were extremely faulty. The calculated BET surface area of defect-free UiO-66 (ideal 3D 12-connected framework) was 1100 m^2/g, whereas the experimentally observed BET surface area of the UiO-66 sample produced by an HCl-assisted method was 1580 m^2/g, which is close to the calculated BET surface area of a defective UiO-66 with a 3D 8-connected framework (1400 m^2/g). Highly crystalline UiO-66 was collected by stirring the obtained Zr(IV) precursor solution with H_2BDC at room temperature. BET surface area was tested to be 1450 m^2/g (DeCoste et al., 2015). In addition, using a solution of $Zr(NO_3)_4$ and H_2BDC in a combination of water and acetic acid (3:2 v/v ratio) and refluxing for 24 hours, it was found that UiO-66 was generated by a regulated hydrothermal reaction (Katz et al., 2014). All these works suggest the facile synthesis of UiO-66.

1.2.2 Application of UiO-66 and its derivatives

The primary application for MOFs was gas adsorption with influence in separation and purification, including water purification, toxic gas removal, gas storage, and acidic gas adsorption(Wang et al., 2018). In a recent review by Fang et al, UiO-66 was analyzed for catalysis, doping processes, sensors, and biomedicine (Fang et al., 2020). For MOFs employed in catalysis, stability was a key worry; nevertheless, UiO-66, which has high structural robustness,

was one of several potential MOFs. In virtually every case, using UiO-66 or one of its derivatives increased the overall reaction's conversion efficiency. With octahedral cages (~11 Å) and tetrahedral cages (~8 Å) joined by open triangular windows (5-7 Å) UiO-66 has a rather large surface area. In water, UiO-66 has excellent thermal and chemical stability, and it is even stable in very acidic aqueous solutions. UiO-66 was shown to have a high adsorption capacity for polar analytes. UiO-66 has been successfully applied in the determination of veterinary residues, environmental contaminants, pesticide residues, and other samples using solid-phase extraction (SPE), magnetic SPE (MSPE), dispersive SPE (DSPE), solid-phase microextraction (SPME), and stir-bar sorptive extraction (SBSE) adsorbents (Cheng et al., 2021; Zhang et al., 2021).

The utilization of UiO-66 nanoparticles (NPs) as innovative pulmonary drug delivery vehicles is investigated by Jarai et al. This discovery is essential because it shows that UiO-66 has a high level of consistency, which is important for pulmonary medication delivery plagued by fluctuating doses. Furthermore, UiO-66 NPs showed pH-dependent stability, with resistance to extracellular degradation and disintegration in intracellular settings (Jarai et al., 2020). Additionally, the UiO-66 delivery systems showed great *in vitro* biocompatibility and minimal cytotoxicity, while *in vivo* mouse studies of orotracheally delivered UiO-66 NPs showed that they were well tolerated. UiO-66 MMMs were used in the automated flow-through SPE of phenols, a recognized environmental contaminant, by Ghani et al (Ghani et al., 2017). UiO-66 MMMs were made by combining mechanically stable polyvinylidene difluoride (PVDF) with UiO-66 or UiO-66-NH_2 (90 to 300 nm) in DMF, yielding UiO-66 MMMs with a thickness of 0.1 mm. The approach of sequential injection analysis was used to assess the MOF-MMMs' performance for automated SPE of seven substituted phenolic compounds prior to HPLC analysis. A MMM made with 90 nm UiO-66-NH_2 crystals yielded the greatest extraction

efficiency. The incorporation of the chosen MOF-MMMs in the extraction process achieved limit of detection (LODs) ranging from 0.1 to 0.2 g/L (Ghani et al., 2017). The adsorption of methylchlorophenoxypropionic acid (MCPP, a herbicide chemical) from dilute aqueous solution was demonstrated using ice-templated UiO-66/Chitosan composite monoliths. The freeze-dried monoliths were treated with a NaOH solution for solvent swapped. The adsorption capacity of the treated chitosan/UiO-66 monolith was 34.33 mg/g. Tweezers were used to readily recycle the composite monolith, and after three further cycles, over 80% of the adsorption capacity was achieved (Fu et al., 2017).

1.3 Introduction of Pickering emulsion

1.3.1 Overview of Pickering emulsions

Emulsifiers are critical for the development and stabilization of food emulsions. Molecular-based emulsifiers, which are surface-active chemicals that situate onto the oil-water interface, lower interfacial tension, and produce droplets, were widely applied in the food sector. However, under specific environmental conditions, such as particular ionic strength, pH, mechanical, and temperature settings, molecular emulsifiers were ineffective in preventing emulsion flocculation (Boire et al., 2019). This may restrict their usefulness in commercial food items, which are subjected to a wide range of environmental conditions.

Over the last several years, there has been a lot of study on developing "Pickering emulsions" by replacing molecular-based emulsifiers with particle-based equivalents (Sarkar & Dickinson, 2020; Y. Wu et al., 2019). Inorganic particles, such as metal oxide, metal hydroxide, silica, metal sulfate, clay, and carbon-based particles, have traditionally been utilized for this purpose(Lv et al., 2021). These solid particles adsorb on the oil-water interface, inhibiting droplet coalescence to a large extent. Molecular-based and particle-based emulsifiers behave

quite differently during the creation and stabilization of Pickering emulsions (**Figure 1-1a** and **1-1b**). During the emulsification process, molecular emulsifiers tend to swiftly adsorb onto surfaces and then reside in equilibrium with the non-adsorbed form, whereas particle emulsifiers adsorb slowly and permanently. Molecular emulsifiers also help to stabilize emulsions by lowering the interfacial tension between the continuous and dispersed phases, which makes droplet deformation and disruption easier during homogenization. Small droplets are developed as a result, which are subsequently coated by a layer of emulsifier molecules, providing a strong repulsive force (typically steric or electrostatic) that prevents droplet aggregation. Particle emulsifiers that are partly wetted by both continuous and dispersed phases, unlike molecular emulsifiers, tend to adsorb onto interfaces without creating a significant drop in the interfacial tension. As a result, because the interfacial tension is quite high, it is more difficult to generate tiny droplets during homogenization. Pickering emulsions may be stabilized by three mechanisms summarized in **Figure 1-1c** (Zhu, 2019):

a. Particles forms a dense layer at the interface of the droplets, which prevents droplets from coalescence through steric repulsion;

b. Aggregated particles in continuous phase are formed, which inhibit droplets movement;

c. Depletion interactions between particles provide another attraction force, which further inhibits droplets' movement.

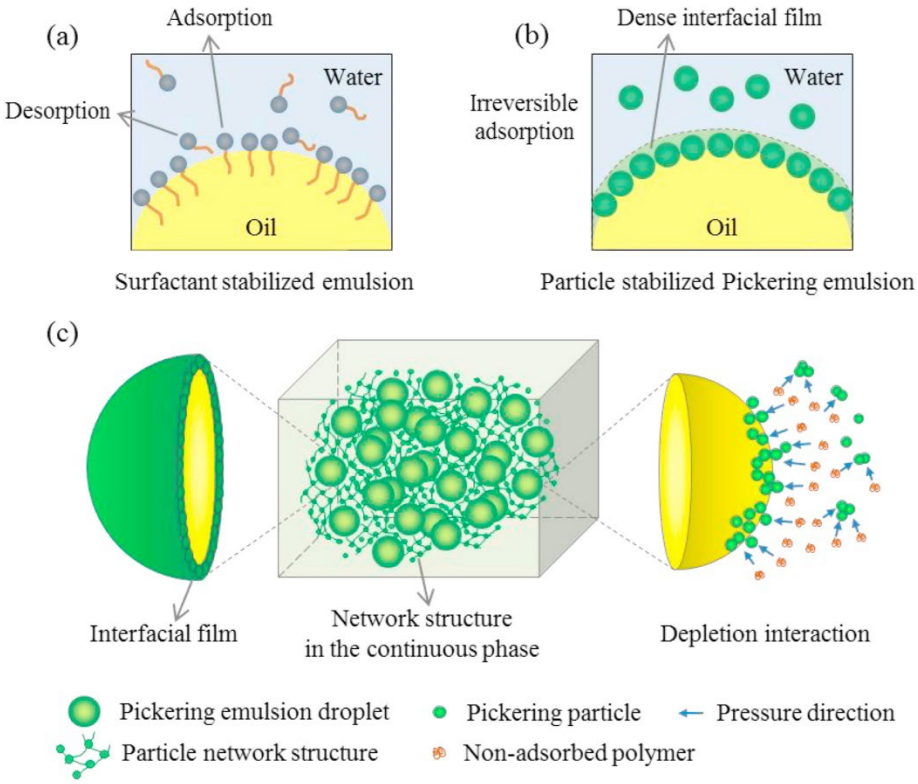


Figure 1-1(a) Schematic representation of molecular emulsifiers adsorbed onto the oil-water interface to form emulsion system, (b) particles adsorbed onto the oil-water interface to form Pickering emulsion, and (c) three stabilization mechanisms of Pickering emulsion: interfacial film, network structure in the continuous phase, and depletion interaction

1.3.2 High internal phase Pickering emulsions

Pickering emulsions with a high internal phase (HIPPE), commonly known as gel emulsions, are a special kind of Pickering emulsion. Lissant initially described the HIPPE system in 1966 as an emulsion system with a minimum internal phase volume ratio (ϕ) of 0.7. (Lissant, 1966). HIPPEs are now often defined by a random close packing index of greater than 0.64 or a close hexagonal packing index of greater than 0.74 (Ikem et al., 2008). HIPPE offers several unique properties, including excellent physicochemical stability and high loading capacity for encapsulation systems. HIPPEs have been employed in a variety of applications, including organic semiconductors, filter membranes, and drug delivery systems (Xu et al., 2018). The creation and stabilization of HIPPEs are explained by a variety of ideas. According to one

theory, phase inversion is essential for the creation of HIPPEs, probably because the homogenization process is involved, which enhances particle homogeneity. In another one, HIPPEs are maintained by raising the continuous phase's viscosity or altering the surface of colloids, preventing particle absorption onto the interface and hence the creation of atypical Pickering emulsions (Ikem et al., 2008). The third theory predicts that HIPPE systems are mechanically stabilized against phase inversion and sedimentation (Menner et al., 2007). So far, there are no clear conclusions on the stabilization mechanism of HIPPE systems. Because of the irreversible adsorption of particles to the interface, HIPPEs stabilized by colloidal particles outperform HIPEs stabilized by low molecular surfactants. However, because phase inversion happens at $\phi > 0.7$, as predicted by theory and proven in tests, creating HIPPEs has been assumed to be exceedingly difficult. This phase inversion might be avoided by using particles that are evenly scattered in a continuous phase but do not readily adsorb to the interface, making Pickering emulsions even difficult to be stabilized. Nonetheless, via meticulous surface modification of colloids or the use of synthetic colloids with the right surface qualities, numerous researchers have succeeded in producing HIPPEs under extremely constrained settings (**Figure 1-2** (Kim et al., 2017)).

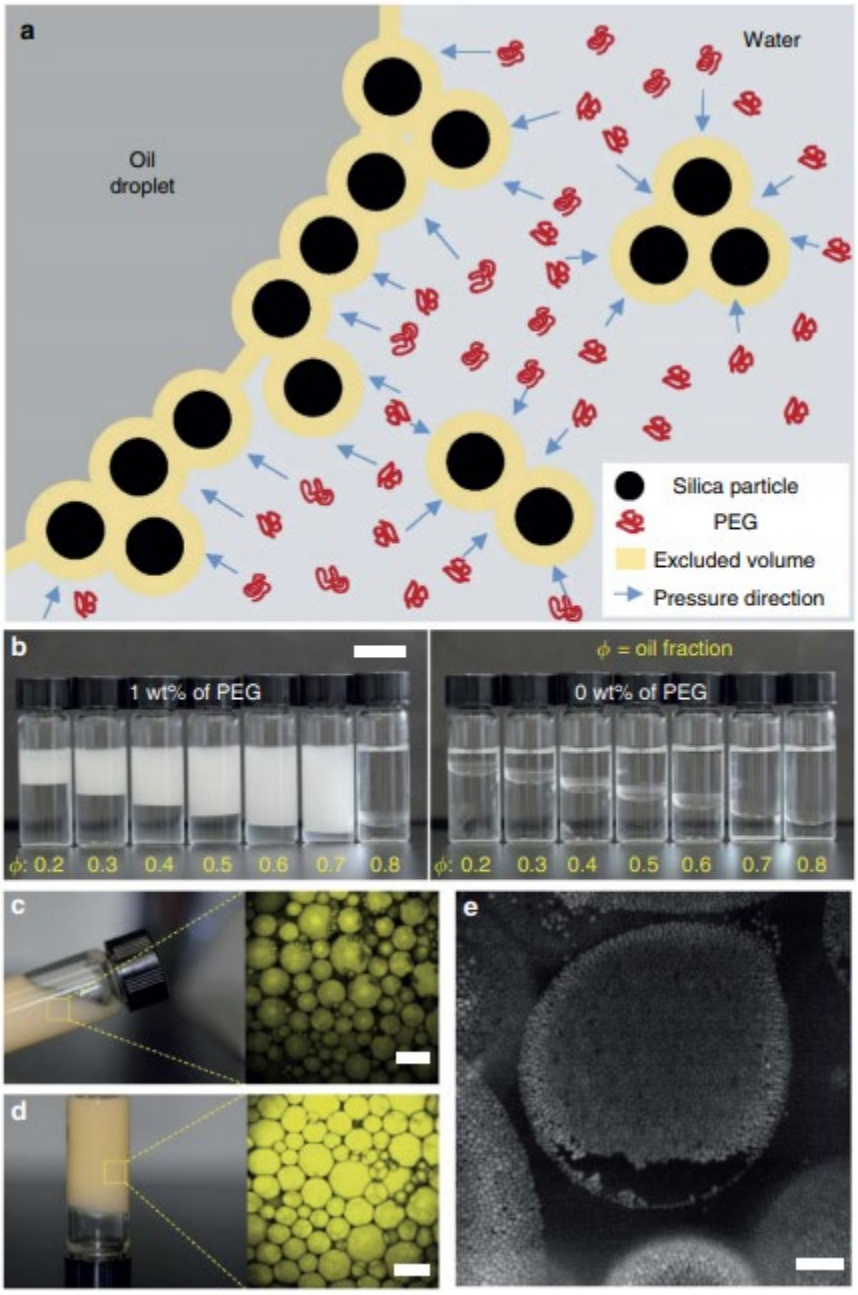


Figure 1-2 (a) Schematic illustration of particle adsorption to the interface by depletion attraction. (b) Photographs of compared emulsions (0.18 vol% of 1 mm-silica particles) formed with the presence of PEG (10,000 g mol 1, left) and the absence of PEG (right), taken after several hours from voltex emulsification (B3,000 r.p.m.). Here, f is the oil fraction of the initial oil–water mixture before emulsifying. Scale bar, 1 cm. (c) Photograph of f ¼ 0.6 emulsion (0.18 vol% silica particles) with oil-soluble fluorescence dyes and its confocal micrograph. Scale bar, 100 mm. (d) Photograph of f ¼ 0.8 high internal phase Pickering emulsion (0.18 vol% silica particles) and its confocal micrographs. Scale bar, 100 mm. (e) Confocal microscope image of fluorescently labelled silica particles (1.08 vol% silica particles) well adsorbed on an oil droplet surface by depletion attraction. Scale bar, 30 mm. All emulsions and HIPPEs (b–e) are produced by the vortexing method

1.3.3 Key factors for Pickering emulsion stabilization

Interfacial particle adsorption is the main stabilizing process in Pickering emulsions. Whey protein isolate (WPI) and zein particles, which are adsorbed to the emulsion droplet surfaces, can prevent coalescence in Pickering emulsions. This coating consists of a single layer or many layers of colloidal particles adsorbed to the oil-water interface, resulting in a strong steric repulsion that prevents droplet aggregation (Murray, 2019). Furthermore, charged colloidal particles provide an electrostatic repulsion between droplets, which prevents them from aggregating (Gurkov et al., 1998; Tcholakova et al., 2008). The particle layer may also improve the physical stability of Pickering emulsions by steric repulsion and depletion interaction, resulting in the formation of smaller droplets during homogenization (Harman & Uphoff, 2019).

Pickering emulsions can also be made more stable by forming a three-dimensional viscoelastic network of colloidal particles in the continuous phase. This stabilizing mechanism requires a sufficiently high concentration of non-adsorbed protein particles in the continuous liquid phase, as well as an appropriately attractive force occurring between them. The presence of this 3D viscoelastic particle network increases emulsion stability by preventing oil droplets from migrating. Pickering emulsions made by peanut protein isolate microgels were shown to stabilize over 85% of the oil phase, which was attributed to the combined effect of the adsorbed particle layer and the formation of a 3D-particle network (Araiza-Calahorra et al., 2018).

Pickering emulsions can also be stabilized in the continuous phase by a depletion mechanism employing non-adsorbing polymers (Kim et al., 2017; Yan et al., 2020). By producing osmotic stress, the presence of a sufficiently high concentration of non-absorbing polymer molecules in the Pickering emulsion causes the emulsion droplets and colloidal particles to flocculate (Bai et al., 2018; McClements & Decker, 2000). According to several studies, protein fibrils may be added to colloidal dispersions as non-absorbing polymers to improve

depletion stability in oil-in-water emulsions (Blijdenstein et al., 2004; Peng et al., 2016). So far, only a few research have employed this technique to increase the stability of Pickering emulsions.

1.4 The colorimetric sensor array

1.4.1 Structure and principle of the colorimetric sensor array

Different techniques that replicate the mammalian olfactory system have recently been widely explored and developed for explosives, narcotics, and food detection. Colorimetric sensor array technology is one of them. It could detect and differentiate complex components (Janzen et al., 2006). By providing individual reactions to each odorant, this cross-responsive sensor technology tries to emulate the mammalian olfactory system. A colorimetric change is generated by intermolecular interactions between the active center and analytes, which can be caused by strong chemical interactions or simple physical adsorption (i.e., chemo-responsive). A colorimetric sensor array provides a unique fingerprint for any odorant using chemo-responsive colorants. As shown in **Figure 1-3** (Xiao-wei et al., 2018), colorimetric sensor arrays use cross-sensitive, chemically responsive dyes to provide a composite, olfactory-like response that is specific to a single odorant and can be measured and evaluated via digital photography. The colorimetric sensor arrays have been applied in many fields including chemical sensors (Janzen et al., 2006) and food science(Qin et al., 2013). The colorimetric system has numerous advantages:

1. Colorimetric approaches allow for *in-situ* detection of color changes.

2. Colorimetric sensor arrays use digital photography to give an accurate, efficient, and sensitive method for detecting chemical substrates in real-time.

3. Colorimetric sensor arrays might be easily downsized, allowing many studies to be performed with a single apparatus at a central location.

4. Colorimetric sensor arrays are competent for detecting flammable, explosive, and toxic compounds.

Therefore, the colorimetric sensor array technology shows extraordinary potentials in food "odor visualization". There are massively researchers who have an interest in it.

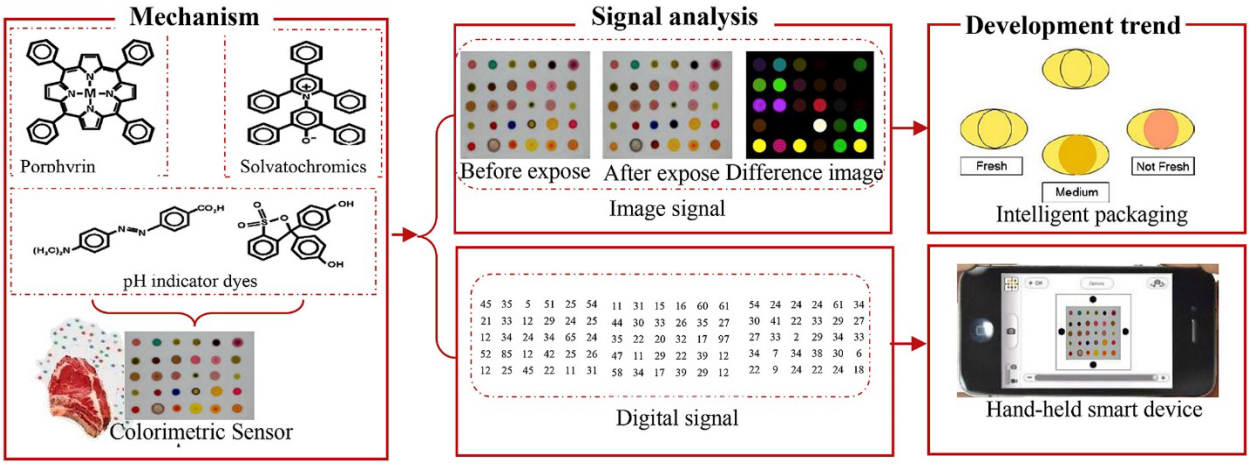


Figure 1-3 The analogy between the biological and colorimetric sensor arrays' systems

1.4.2 Data analysis and signal extraction of the colorimetric sensor array

Cross-reactive sensing and fingerprint pattern recognition are two inseparable components of an accurate and portable artificial smell screening. In these artificial smell systems, cross-reactive sensing is accomplished by mixing metal oxides or colorimetric dyes with sensor arrays that may target distinct molecules to form a fingerprint pattern (Guo et al., 2020). Due to a variety of factors, only a few systems have been commercialized so far. Traditional statistical approaches, such as linear discriminant analysis (LDA), principal component analysis (PCA), and hierarchical cluster analysis (HCA), were constrained by the high complexity of the image-based pattern-recognition technology. Second, low adsorption

rates and poor selectivity for targeting volatile aroma compounds (VACs) plagued these sensors' systems, resulting in low accuracy and sensitivity (Imam & Cleland, 2020).

To depict the colorimetric sensor signal, the main (i.e., red green blue, RGB) imaging approach was usually used. By subtracting the before-exposure picture from the post-exposure image, i.e., the red value after exposure to the VACs of the sample minus red value before exposure, and the same for green and blue, a difference image that exhibited color changes of the sensor array could be obtained (C. Wu et al., 2019). After averaging the findings at the center of each dye spot to reduce variance owing to color non-uniformity, the results at the center of each dye spot are reported. Because they cannot be recognized by naked eyes, it is essential to increase the color-difference range to 0–255 to display the color shift. As a result, a 3N dimensional vector (N dyes * 3 color component difference) might be used to characterize the response of a colorimetric sensor array with a dye spot number of N to the detected analyte. Certain chemometric approaches, such as PCA, LDA, and HCA, might be used to examine the resulting 3N-dimensional matrix. In most chemometrics datasets, a high number of color-difference variables predict a complex dependent variable; however, the difficulty may be mitigated by using appropriate projection or selection procedures (Xiao-wei et al., 2018; Xiao-wei et al., 2016).

1.4.3 Application of colorimetric sensor arrays in the food area

Colorimetric sensor arrays may overcome chromatography's limitations, which are proved to be a perfect method for detecting VACs. Kim et al. chose ammonia (20 ppm), methylamine (20 ppm), hydrazine (30 ppm), and TMA (20 ppm) as target gases, and created an array with 10 distinct pH indicators using a printing approach. The smartphone transmits the image of the detected gas to the central control system, allowing for a speedy real-time response

to gas leaking (Kim et al., 2018; Park et al., 2018). To monitor the VACs in rice during storage, Lin et al. developed a colorimetric sensor array based on boron-dipyrromethene (BODIPY) dyes (Lin & Buccella, 2018). GC–MS and multivariate analysis results showed that the chemical 18-crown-6 rose surged considerably during the rice aging process. Yang et al. developed a pathogen identification system using a paper colorimetric sensor array and machine learning (Yang et al., 2021). The color changes were collected digitally and serve to train a multi-layer neural network (NN), endowing it with high-accuracy (91–95%) strain-specific pathogen identification and quantification capabilities. The trained PCA–NN system can discriminate between live *E. coli* O157:H7 and other viable pathogens, and detect both *Listeria* and *E. coli* O157:H7 on fresh-cut romaine lettuce, simulating a realistic and complicated environment in practice.

1.5 Machine learning and its application in the food area

1.5.1 Major categories of machine learning methods

Many sophisticated machine learning algorithms have been created to address issues of various levels of complexity. The following are four representative and essential learning algorithms.

K-means is an unsupervised technique for dynamically grouping comparable data into clusters. It allocated geometric centers of observations (centroids) to prototype clusters, and observations were assigned to clusters if they were closer to the centroid than any other centroids (**Figure 1-4a**)(Likas et al., 2003). By encoding observations of different classes as points, the support vector machine (SVM) employs planes to best divide them. A fresh observation is projected into space, and its class is determined by the side of the plane it falls on. SVM is most effective with data that are well-separated into multiple classes (**Figure 1-4b**)(Joachims, 1998).

Through the interplay of characteristics, decision trees seek to partition instances into distinct classes recursively. A fresh sample follows certain branches indicated by the characteristics until it lands on a leaf that determines the sample's predicted class. It is feasible to randomize this process by averaging the outcomes of several separate trees (random forest) and to develop branches by using a more measurable criterion by using an objective function (gradient boosting) (**Figure 1-4c**)(Quinlan, 1986). Ensemble learning encompasses all of the strategies discussed above. By covering layers of interconnected artificial neurons known as processing units, an artificial neural network (ANN) replicates organic brain networks. These nodes take in data and process it using a system that contains a nonlinear activation function, a linear weights-input combination, and output signals to the next layer of nodes. Each ANN has at least one input layer, several intermediate levels known as hidden layers, and a single output layer. They might work together to turn raw data into regression or classification results (**Figure 1-4d**, (Deng et al., 2021)). A deep neural network is an ANN structure with numerous hidden layers that is at the heart of deep learning(Hassoun, 1995).

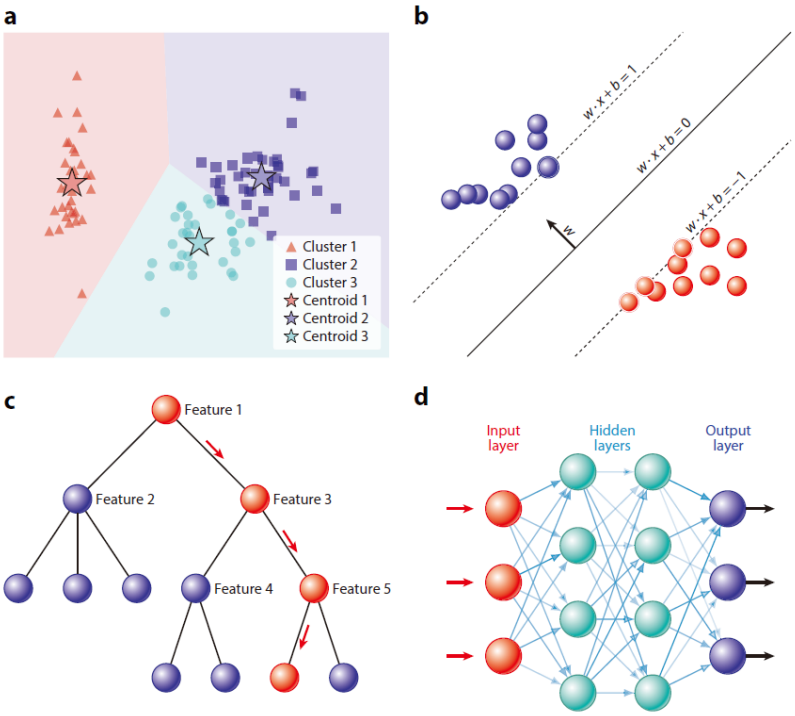


Figure 1-4 Examples of machine learning models. (a) A decision boundary plot of k-means clustering with three clusters, with new samples being grouped to a cluster by the colored region it lands on. (b) A line dividing two classes in a support-vector machine with a certain margin. w contains the trainable parameters, and x stands for the vector representation of a sample. (c) A decision tree with five features. A sample is classified into a certain class following the red arrow. (d) A neural network with two hidden layers; the arrow stands for a connection between units, with transparency indicating the connection strength

1.5.2 Machine learning application for genomic data

Machine learning shows potential in genomics, genetics, and medicine for generating biological discoveries and predictions from vast genomic data sets(Mamoshina et al., 2016). Sequence annotation is the process of teaching machine learning algorithms to detect elements and patterns in DNA sequences(Shi et al., 2019). Machine learning models have found genomic fingerprints (e.g. biomarkers) to aid in clinical decision-making, illness diagnosis, and medication discovery and development(He et al., 2019). Due to the infections' comparably short genomes, one may presume that the machine learning study of their genomes is an iteration or extension of existing methods. However, as machine learning is increasingly tapped into the

rapidly developing genomes of foodborne pathogens and associated information resources, domain-specific problems will continuously emergence. The genetic source attribution or antimicrobial resistance (AMR) prediction for specific diseases is particularly noteworthy (Libbrecht & Noble, 2015).

1.5.3 Machine learning application for computer vision

Food identification and classification are critical activities that aid in people's daily dietary records. Food images are one of the most important bits of information for imitating food qualities. The Food-101 database is the most widely used dataset for food recognition. It contains 101 food types, each with 1000 photos (Ege & Yanai, 2018). Many deep-learning-based food classifiers have been trained using this database after it was published(Bossard et al., 2014). In food classification research, top-1 classification estimate accuracy (top-1) and top-5 classification estimation accuracy (top-5) are two significant assessment markers. Tatsuma and Aono (2016) were the first to use the Food-101 database to train a CNN model. They used the covariances of learned CNN features as picture representation and obtained a top-1 accuracy of 58.65 % (Tatsuma & Aono, 2016). Following that, fine-tuned DeepFood, AlexNet, Inception v3, ResNet, and WISeR increased top-1 accuracy to 70.41 %, 76.30 %, 76.17 %, 80.60 %, and 89.58 %, respectively(Zhou et al., 2019). The top-5 was also improved at the same time as the top-1, rising from 92.00 % (DeepFood) to 99.23 % (WISeR)(Zhou et al., 2019). Matsuda originally released UECFood-100 in 2012, which included 100 Japanese food courses and 100 photographs for each class(Matsuda et al., 2012). Because the study drew a lot of interest when it was published, UECFood-256 was released in 2014, featuring 256 classes of Japanese cuisine and 100 photos in each class(Ciocca et al., 2018). The UECFood-256 database's accuracy improvement pattern is comparable to that of the Food-101 database. The UECFood-256

database was used to test DeepFood, ResNet, Inception v3, and WISeR models. The top-1 accuracy increased from 54.70 % to 83.15 % (WISeR), while the top-5 accuracy increased from 81.50 % to 95.45 % (DeepFood) (WISeR)(Kuo et al., 2019).

Apart from food picture identification, image-based sensing is a relatively simple and low-cost data collecting approach for food appearance study. Yu, et al., (2019) investigated how to use deep learning to correlate hyperspectral data for measuring total volatile basic nitrogen (TVB-N) concentration in shrimp(Yu et al., 2019). For TVB-N content prediction, three types of regression algorithms were used: least-squares support vector machine (LS-SVM), partial least squares regression (PLSR), and multiple linear regression (MLR). It was discovered that the combination of SAEs and the LS-SVM model produced the greatest results (RP2 = 0.921, RMSEP = 6.22 mg/100g, RPD = 3.58) while consuming the least amount of time (3.9 ms, RP2 = 0.921, RMSEP = 6.22 mg/100g, RPD = 3.58).

1.5.4 Machine learning application for natural language processing

Rapid food analysis and personal dietary records may benefit from automatic, accurate, and robust food attribute prediction utilizing new machine learning approaches such as artificial intelligence. Ma et al assessed five machine learning models for quantitatively predicting nutrients from meals based on their constituents for the first time(Ma et al., 2021). A machine-readable dataset for two domains - nutrient and ingredient - was created using the USDA Global Branded Food Products Database (BFPD). Five notable models were studied based on these datasets to predict 13 label nutrients contained in BFPD based on their constituents, including AdaBoost, Bayesians, Linear Support Vector Machine (SVM), Multi-Layer Perceptron (MLP), and one tailored-improved MLP termed MLPcr. In this article, three different nutrients – carbs, protein, and salt – were described. The neural network model, MLP, and MLPcr predictions had

the highest accuracy, reaching 0.900 for carbs. The data distribution and multi-factor complexity have a significant influence on the accuracy of the final forecast, according to a comprehensive analysis of the prediction findings.

1.6 Research objectives

1.6.1 Development of UiO-66 derivatives-based food delivery systems.

In this section, a type of curcumin-loaded UiO-66 (representative high biocompatibility and water-stable metal-organic framework) deliver systems was prepared, named curcmin@UiO-66. A unique metal-organic framework-based delivery method for food bioactive phytochemicals was developed to investigate the applicability of the UiO-66 family in the food industry. The UiO-66 family was discovered by atomic simulations of electronegativity and amphiphilic characteristics, both of which are important for food delivery system stability. After the synthesis of UiO-66, the objective was to assess the physicochemical characteristics of UiO-66 NPs and their derivatives under a variety of food environmental circumstances, including pH, temperature, and the interaction of UiO-66 NPs with phytochemicals. This research aims to demonstrate that stable MOFs might have the potential in constructing efficient delivery systems.

1.6.2 Development and optimization of UiO-66 derivatives-based emulsion systems for food application.

In this section, a novel UiO-66-NH_2 stabilized HIPPE delivery method was developed and optimized. Based on the simulation result from the first objective. Solvothermal syncretization was used to make the majority of the monodispersed UiO-66-NH_2 NPs. The objective was to prepare PE and HIPPE via i*n situ* high-pressure homogenization and evaluate their physicochemical features, such as crystallography, morphology, and rheology, which were systematically studied. Another objective of this section was to optimize MOF-PE by a four-factor, three-level Box-Behnken design (BBD) and response surface methodology (RSM)

analysis and systematically evaluate the effect of various experimental parameters (such as ultrasonic power, ultrasonic time, oil content, and MOF content) on curcumin loading capacity (LC) and encapsulation efficiency (EE). This result aims to demonstrate that MOF nanoparticle stabilized HIPPE delivery system could be practically utilized for other bioactive components and antimicrobial agents, which would find applications in food safety and biomedical areas in the future due to their high loading capacity and stability.

1.6.3 Development and optimization of UiO-66 derivatives-based colorimetric sensor array based on deep learning for food package.

In this section, the objective is to develop two integrated portable food freshness prediction platforms, one using an ice-template UiO-66-Br sensor array and the other using a MOF-MMM-based UiO-66-OH sensor array system. After creating sensor arrays, the physicochemical characteristics and morphologies were comprehensively examined, including FT-IR, SEM, and stability. In addition, another objective is to evaluate the effectivity of DCNN, a deep learning algorithm family, was also leveraged to monitor shrimp and chicken freshness by detecting the fragrance. This research aims to demonstrate UiO-66-based sensor array platform is integrated, sensitive, and non-destructive, enabling consumers to monitor shrimp freshness in real-time conveniently.

Chapter 2 UiO-66 nanoparticles as a carrier for curcumin delivery

2.1 Abstract

In this study, a novel metal-organic framework (MOF) delivery system for a food bioactive was developed. A series of molecular simulations tools, reported in recent years, have been applied to predict and optimize the delivery system. First, Zr-based MOF UiO-66 was synthesized with Zirconium (IV) chloride and benzene-1,4-dicarboxylic acid. Then, curcumin was encapsulated in it using a post-synthesis loading method. Both spectroscopy and thermogravimetric analysis showed that the system achieved a high loading capacity of 3.45% w/w. The crystal structure, porosity, morphology of the curcumin delivery system were characterized using X-ray diffraction (XRD), physisorption analyzer, scanning electron microscopy (SEM), and energy-dispersive X-ray spectrometer (EDS), respectively. An *in vitro* digestive test showed control release of curcumin in the simulated intestinal fluids (SIF). Around sixty percent of curcumin was released after 180 min of digestion. This research demonstrated that stable MOFs might have the potential in constructing efficient delivery systems.

2.2 Introduction

Recently, various delivery systems have been developed for controlled release of food bioactive, including nanoemulsion, nanoparticle, organic micelles, liposomes, and inorganic porous materials (Fu et al., 2014; Kittitheeranun et al., 2015; Ma et al., 2017, 2018; Sun et al., 2015; Tian et al., 2018). However, these delivery systems have intrinsic limitations in food applications. For example, nanoemulsion suffered from undesirable loading capacity and stability (Imanifard et al., 2017). Organic micelles and liposomes have also shown poor loading capacity (He & Shi, 2011). Inorganic porous materials showed unacceptable toxicity and low stability (Fu et al., 2014). Ideally, the food delivery systems should have a large loading capacity,

nanoscale particle size, high biocompatibility, and controllable gastrointestinal stability (Wu & Yang, 2017). As a result, metal-organic frameworks (MOFs) have been attempted to design food delivery systems since they show exceptionally high surface area, low toxicity, and tunable porosity.

MOFs and other porous coordination polymer systems self-assembled by metal-connecting ions and polydentate bridging ligands have drawn considerable research attention as a new class of hybrid material(Liu & Peng, 2017; Tai et al., 2016; Zhang et al., 2015). The majority of these structures are believed to be conceptual because the reversible nature of coordination bonds leads to poor stability. The structures include divalent MOF (Zn^{2+}, Cu^{2+}) and trivalent MOF (Al^{3+}, Cr^{3+})(Bai et al., 2016). Recently, a remarkable step to improve the structural stability of the MOF system was achieved by the discovery of $Zr_6(m_3\text{-}O)_4(m_3\text{-}OH)_4(BDC)_6$ (UiO-66, UiO for University of Oslo) with 12-coordinated $Zr_6(m_3\text{-}O)_4(m_3\text{-}OH)_4(CO_2)_{12}$ clusters(Cavka et al., 2008). This material shows very low toxicity (Zirconyl acetate lethal dose LD_{50} is ~ 4.1 mg/mL in rats and human body contain amount ~ 3.5 mg per day ingested (Grimmer et al., 2000). LD_{50} of Mg, Ca, Fe, Zn is 8.1, 1.0, 0.45, 0.35 mg/mL, respectively (Horcajada et al., 2012)) and excellent stability. Afterward, many new structures have been reported based on Zr (IV) ions, especially Zr (IV) carboxylates with different ligands (Orellana-Tavra et al., 2015). Meanwhile, there is some research focusing on edible MOFs, such as MOFs prepared by γ-cyclodextrin and potassium (Smaldone et al., 2010). Therefore, it is expected that MOFs have the potential to be applied in the food industry.

In a previous study, we have developed a facile post-synthesis loading method for Zn–MOF with thymol, which showed enhanced antimicrobial activity against E. coli for 24 hours(Y. Wu et al., 2019). In the current study, we first constructed a simple surfactant-free delivery

system for encapsulating curcumin being serving as a model bioactive compound. Meanwhile, the emergence of machine learning tools such as deep learning provides a new possibility to predict the interaction between metal ions and organic compounds quickly and simply. The results of the data simulation also helped us to explore the relevant mechanisms in a more depth way. Although this research is still in the early stage of development, we want to explore a novel application of Zr-based MOF with high stability, high loading capability, which could build a delivery system representing a potential breakthrough in the food research area.

2.3 Material & methods

2.3.1 Material

Zirconium tetrachloride (99.5 %), benzene-1,4-dicarboxylic acid (BDC, 98.0%), N,N-dimethylformamide (DMF, 99.0%), hydrochloric acid (HCl, 37.0%), Tween-80, dextrose, sodium chloride (NaCl, 99.5%), potassium chloride (KCl, 99.0%), disodium hydrogen phosphate (Na_2HPO_4, 99.0%), sodium phosphate monobasic (NaH_2PO_4, 99.0%) and acetic acid (99.9%) were purchased from Sigma-Aldrich (St. Louis, MO, USA). All the chemicals are in analytical grade.

2.3.2 UiO-66 property simulation

Crystal structural units were obtained from the Cambridge Crystallographic Data Center database (CCDC, https://www.ccdc.cam.ac.uk/). Then the structural units were used to reduce the structure to eight-unit cell (2*2*2) in Material Studio (version 7.6). The crystal structure file was calculated using the RASPA2 simulation to obtain the mass, the density of UiO-66(Dubbeldam et al., 2018). The XRD pattern simulation was calculated by a simulation tool, VESTA, with wave angle from 1 to 30 degrees and relative intensity was set to 1(Tayal et al., 2018). The accessible pore volume, gravimetric surface area (nitrogen), geometric surface area,

windows diameter were analyzed by a pyWINDOW package(Miklitz & Jelfs, 2018). Grand canonical Monte Carlo (GCMC) simulations were used to calculate N_2 isotherms at 77 K for UiO-66. At each pressure, the parameter of the equilibration step was 10,000,000 and this number was set as a computer ensemble average. The framework atom was taken from the Universal Force Field (UFF)(RAPPE et al., 1992). A charge of -0.482 was placed on the N nuclei and +0.964 at the center of mass. Ewald & Group summation method was used for all interactions with atom-based van der Walls. All calculations mentioned above were based on the sorption isotherm module in Materials Studio. The parameters mentioned above were taken from a previous study with some modifications (Katz et al., 2013).

2.3.3 Synthesis of UiO-66

The UiO-66 was synthesized according to a previous report with a little modification(Katz et al., 2013). First, $ZrCl_4$ (1.17 g, 5 mmol) and 1,4-benzenedicarboxylic acid (BDC) (0.83 g, 5mmol), acetic acid 1.0 mL were dissolved in dimethylformamide (DMF) (10 mL) at room temperature. Then, the mixture was placed in a teflon-lined stainless-steel autoclave after adding 2 ml of de-ionized water and mixed completely. The autoclave was placed in an oil bath at 120^{o}C for 24 hours. After the solution was cooled to room temperature for 30 min, the resulting UiO-66 particles were separated via centrifugation at 15000 rpm for 10 min at room temperature and washed three times with ethanol. The resulting white powder was dried under vacuum for 4 hours.

2.3.4 Preparation of curcumin-loaded UiO-66

The loading process was modified from previous research(Orellana-Tavra et al., 2015). After collecting the dried UiO-66, curcumin was loaded by soaking UiO66 in a 500 mg/mL curcumin-ethanol solution overnight with stirring in sealed glass bottles. Next, the curcumin-

loaded UiO-66 (Cur-UiO-66) was washed three times by centrifugation using fresh ethanol and the remaining solvent was evaporated in a 50°C fume hood for 3 hours.

2.3.5 Porosity and surface area of MOFs

The porosity and surface area of MOFs were determined using an ASAP 2020 Physisorption Analyzer (Micromeritics Instrument Corporation, Norcross, GA, USA) following a previous study(Y. Wu et al., 2019). Sample tubes were cleaned ultrasonically and dried at 110°C. The MOFs samples were loaded into the sample tube by degassing for 24 hours. The sample tube with MOFs was then transferred to the analysis port with N_2 as the adsorptive gas and liquid nitrogen as the cold media. Nitrogen monolayer saturated adsorption capacity and surface area were calculated following the **equation 2-1** and **2-2**:

Equation 2-1

$$V_m = \frac{1}{\mathrm{A+I}}$$

Equation 2-2

$$S_g = 4.325 \times V_m$$

I: The slope of adsorption isotherm fit line when P / P_0 was from 0.35 to 0.5;

A: The intercept of adsorption isotherm fit line when P / P_0 was from 0h

35 to 0.5;

V_m: Monolayer adsorbed nitrogen quantity;

S_g: BET surface area.

2.3.6 Crystal structure of MOFs

X-ray powder diffraction (XRD) patterns were obtained from an XRD diffractometer (C2 Discover Bruker Diffractometer, Madison, WI, USA) with CuKα radiation to evaluate the crystal structure of MOFs. X-ray scan ranged from (2θ) 3.5° to 30°, step size at 0.02°(Y. Wu et al., 2019).

2.3.7 Morphology of MOFs

Scanning electron microscopy (SEM, Tescan GAIA FIB/SEM, PA, USA) and energy-dispersive X-ray spectroscopy (EDS) characterizations were used to examine the morphology and elemental analysis of UiO-66 and curcumin loaded UiO-66 (Cur-UiO-66). Dried MOFs crystals were adhered to silica tapes and mounted onto specimen stubs. The stubs were coated with a thin layer of carbon. Digital images of the samples were obtained, and representative images were reported(Mei et al., 2017).

2.3.8 Thermogravimetric analysis (TGA)

Thermal analysis of the MOFs samples was performed using a TGA instrument (2950, TA Instruments, Inc.). The parameters were modified from a previous study, under a mixed air and N_2 flow of 100 mL min^{-1} (40% air, 60% N_2) with a heating rate of 10 K min^{-1} from 308 K to 1073 K(Oh et al., 2016).

2.3.9 Loading capacity (LC) of MOFs

Curcumin LC was performed following previous research with some modifications (Orellana-Tavra et al., 2015). The standard curve was prepared by dissolving 6 mg of curcumin in 100 mL of alcohol firstly. Then 0.25, 0.5, 1, 2, 3, and 4 mL of the solution were taken and volume to 15 mL with alcohol respectively. The standard curve was obtained using the content of curcumin as X-axis and the absorbance at 426 nm as Y-axis. 100 mg curcumin loaded UiO-66 was soaked into 20 mL of ethanol at room temperature under orbital agitation for 24 hours. The loaded materials were collected by centrifugation at 5,000 rpm for 15 mins. The loaded materials were washed triple times with ethanol centrifuged again and dried overnight at 60°C to remove the solvent. All treatments were performed in triplicate. The loading capacity of curcumin was quantified by using a UV-vis spectrophotometer (Beckman Coulter, Brea, CA, USA). The

absorbance of the supernatant at 426 nm after first centrifugation was measured to calculate curcumin content. The loading capacity was given by the **equation 2-3**:

Equation 2-3

$$\text{LC (wt. \%)} = \frac{\text{Curcumin}_{\text{added}}\ \text{(mg)}}{\text{Curcumin}_{\text{added}}\ \text{(mg)} + \text{material (mg)}}$$

2.3.10 In vitro digestion

Simulated digestion fluids consisted of gastric and intestinal fluids in the present work. The method was based on the description of a previous study with some modifications(Sun et al., 2017).

Stomach: 20 mL simulated gastric fluid (SGF), in which pH was adjusted to 2.0 using 0.1 M HCl. Then, 3 mg of curcumin-loaded UIO-66 was placed into the SGF and incubated in a shaking water bath at 37.0 °C with continuous swirling at a speed of 100 rpm for 60 min. The digestion mixture was collected for analysis at 10 min intervals. Gastric digestion was stopped by adjusting pH to 7.5 using 0.5 M NaOH. The amount of curcumin released was measured by using a UV-vis spectrophotometer at 426 nm.

Small intestine: To simulate the physiological condition, a curcumin release experiment was performed in an incubator at 37°C with orbital agitation and using phosphate-buffered saline (PBS, 0.01 M) at pH 7.4. PBS was prepared following a previous study, NaCl (8.0 g), KCl (0.2 g), NaH_2PO_4 (3.6 g), Na_2HPO_4 (0.2 g), Tween-80 (0.5 g), and glucose (50.0 g) were dissolved in water, and volume to 1.0 L without any enzyme or pH adjustment. Every 10 min of gastrointestinal incubation, 10 mL of the digestion dispersions were taken out and neutralized by adding 1 M NaOH to reach an end pH of 7.5. The amount of curcumin released was measured by using its absorbance at 426 nm.

For the crystalline materials, the hyperbola model was used to adjust for release properties in the equation 2-4(Horcajada et al., 2010).

Equation 2-4

$$\mathrm{N(wt.\%)} = \frac{N_{max}t}{(t_{\frac{1}{2}}+t)}$$

N is the amount released from the total drug-loaded amount;

N_{max} is the maximum amount released;

t is time in minutes;

$t_{1/2}$ is the time of half the maximum amount released.

2.3.11 Statistical analysis

The data reported as mean ± standard error was from experiments conducted in triplicate. Experimental statistics were performed using SAS software (Version 9.2, SAS Institute Inc., Cary, NC, USA). The analysis of variance (ANOVA) was used to compare the treatment with $p < 0.05$.

Table 2- 1 Computer simulation output of UiO-66 characteristics

Property	**Simulation output**
Mass	8720.29 g / mol
Density	1664.06 kg / m^3
Accessible pore volume	0.41836 cm^3 / g
Gravimetric surface area (nitrogen)	1280.36 m^2 / g
Geometric surface area	1550.73 m^2 / g
Stimulate BET surface area	1367.74 m^2 / g
Cavities	11 Å (large)
	8 Å (small)

2.4 Results and discussion

2.4.1 Computer simulation of the characteristic of UiO-66 and Cur-UiO-66

The result from computer simulations was summarized in **table 2-1** and the simulated crystal structure of UiO-66 MOF was shown in **figure 2-1**. Theoretically, UiO-66 formed lattices structure linked by $Zr_6O_4(OH)_4$ octahedron and 1,4-benzene-dicarboxylate (BDC) with 12-fold connection(Valenzano et al., 2011). Recently, UiO-66 has been reported to be able to encapsulate and deliver drugs efficiently by adsorbing drugs because it has a highly porous structure and possesses great thermal and chemical stability(Katz et al., 2013). Many researchers reported high loading capacity (LC) of UiO-66, such as caffeine, calcein, etc. LC of these delivery systems was from 1.3 to 22.4 wt. %, which is much higher than those of mesoporous silica and organic carriers usually having LC less than 0.3 wt. %(Orellana-Tavra et al., 2015). Meanwhile, previous research has proven the feasibility of Zr-MOFs as a stable drug carrier with high loading capacity by grand canonical Monte Carlo (GCMC) simulations(Bernini et al., 2014). The Geometric analysis showed that UiO-66 had two groups of cavities, the large one is octahedral (11 Å) and the small one is tetrahedral (8 Å). The ratio of two cavities is 1:2, which would give storage space to curcumin. Moreover, according to **figure 2-1**, each octahedron was 12-fold connected to adjacent octahedra, resulting in a highly packed crystal structure (fcc), which gave UiO-66 unique stability compared to other MOFs. These simulation results were consistent with the simulation data of previous studies on UiO-66 and further supported that UiO-66 may be able to be constructed to an ideal delivery system.

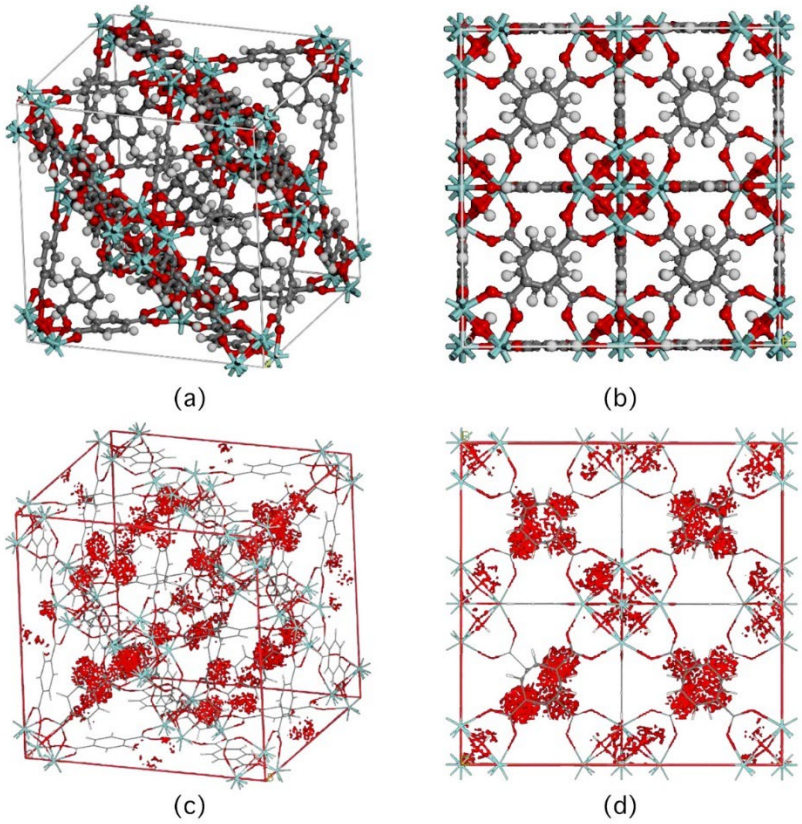


Figure 2-5(a)(b) a view of the UiO-66 porous structure; (c)(d) Monte Carlo simulation of nitrogen adsorption site distribution

2.4.2 Porosity and surface area

Figure 2-2 illustrated comparisons between data from simulation and experiment for N_2 adsorption at 77 K in UiO-66 and Cur-UiO-66. The data from the simulation and the experiment agreed very well. The N_2 adsorption-desorption isotherms of the UiO-66 and Cur-UiO-66 revealed the intraparticle porous structure. The absorption of N_2 increased logarithmically with the environmental pressure(Katz et al., 2013). The BET surface area (1259.74 m^2/g) obtained in this study was larger than those of other types of MOFs prepared by different metal ions and organic linkers, such as MOF-5 (584 m^2/g) and Zn@MOF (617 m^2/g) (Muller et al., 2009; Y. Wu et al., 2019). After loading curcumin, the BET surface area decreased to 290.86 m^2/g. This was caused by the curcumin occupying the interior space and surface window area of MOF,

supporting that curcumin has been loaded in the UiO-66. These characteristics of the porous UiO-66 suggested that it could hold a large number of curcumin molecules. Meanwhile, we saw deviations when comparing different simulations and experiment isotherms, which might be affected by multiple reasons. The result of GCMC simulation calculated the condition of N_2 saturated adsorption, whereas the experiment result was the condition of excessive adsorption of N_2. These differences were also consistent with the results of previous studies(Katz et al., 2013; Orellana-Tavra et al., 2015). In **Figures 2-1 c** and **d**, red points simulated the position of nitrogen adsorption in the system. The result showed there was a large space in the MOF architecture to provide space for the adsorption and fixation of guest molecules.

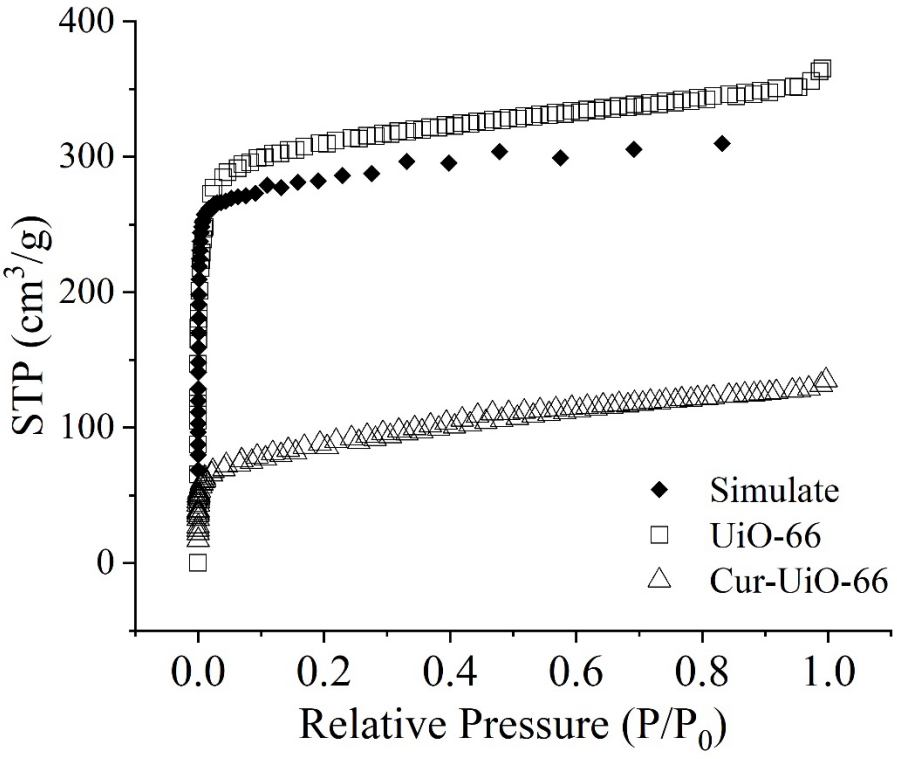


Figure 2-6 N_2 adsorption isotherms at 77 K on UiO-66, Cur-UiO-66 and simulate UiO-66.

2.4.3 Crystal structures

XRD pattern revealed the UiO-66 crystal structure at atomic and molecular levels. Compared with the original crystal structure, the XRD pattern of UiO-66 showed the same structure after being loaded with curcumin (**Figure 2-3**). Meanwhile, when comparing the simulated PXRD patterns of Cur-UiO-66 with UiO-66, they are highly similar with an insignificant difference. This small difference may be caused by two reasons. First, the background noise from the XRD machine, especially the peak of the initial stage. The background noise can be removed by XRD analysis software (the most obvious ones are the first two peaks). Second, there may be another minor crystal structure, for example, the multiple Zr compounds. It is still difficult to confirm the reason for this discrepancy because the peak signal value is too weak. However, compared with other previous research and published PXRD data, this result could prove that the material obtained here is UiO-66 and the material forms a single crystal structure and there is an insignificant difference between the original MOF structure and curcumin loaded MOF structure.

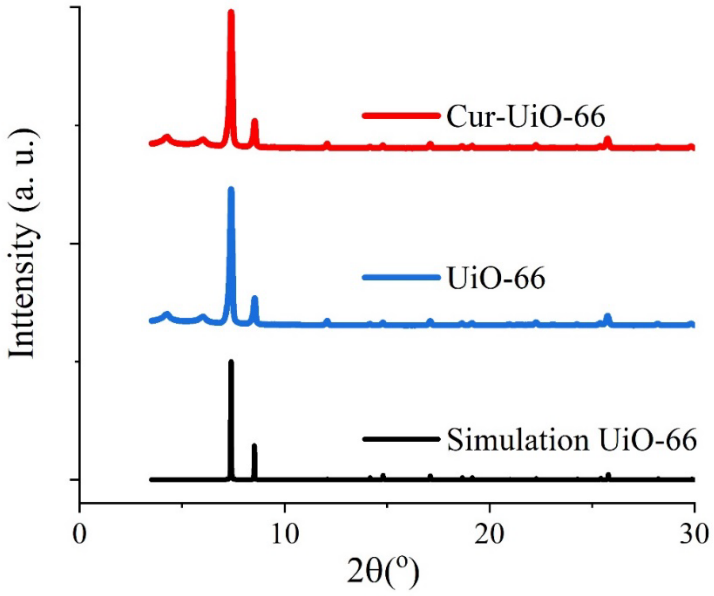


Figure 2-7 Powder X-ray diffraction (PXRD) patterns of synthesized UiO-66 and Cur-UiO-66 compared with the simulated one for UiO-66.

2.4.4 Microstructure

SEM and EDS have been used to characterize different MOF structures(Ploegmakers et al., 2013). The SEM representative images of UiO-66 and Cur-UiO-66 were shown in **Figure 2-4**. Both of them have a discoid morphology with the unit particle size in the range of 100 - 300 nm, which is consistent with previous reports(Orellana-Tavra et al., 2015; Y. Wu et al., 2019). By carefully comparing the EDS spectra of UiO-66 and Cur-UiO-66 (insert in Fig. 4a and b, respectively), we found that the different amounts of carbon and oxygen elements came from curcumin. Meanwhile, it was found that the Zr element was evenly distributed (green point in the EDS figures), indicating that the system formed an ordered structure, which is consistent with theoretical predictions(Chen et al., 2015).

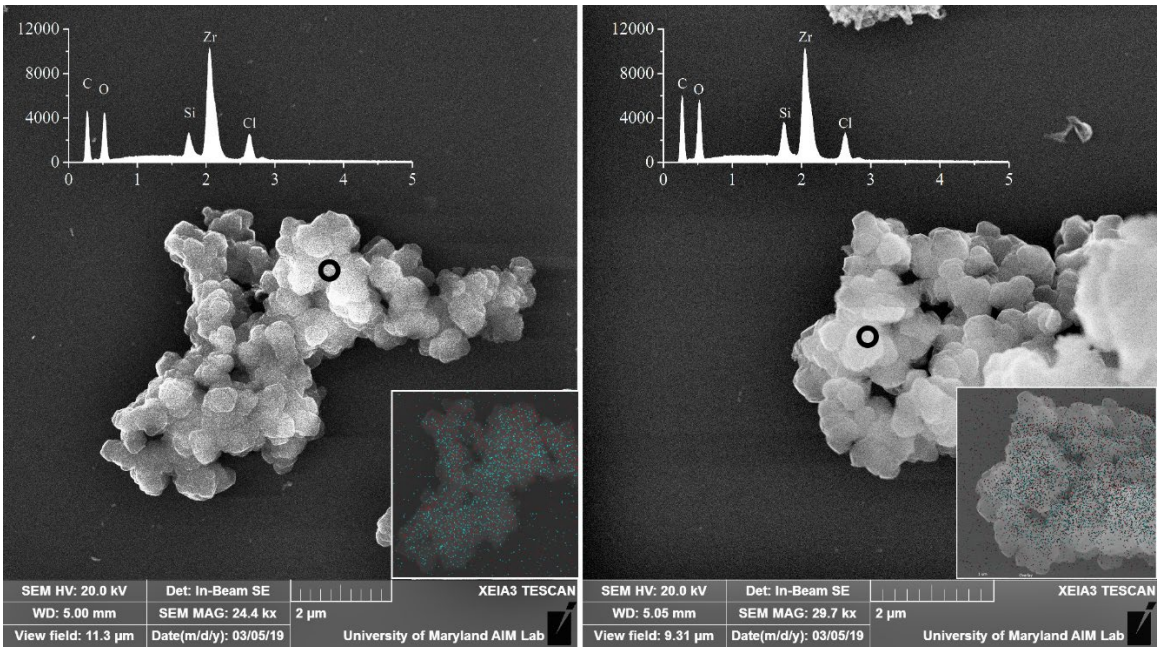


Figure 2-8 SEM images of (a) UiO-66; (b) Cur-UiO-66, (Bar scale = 1 µm).

2.4.5 Thermogravimetric analysis (TGA)

TGA was widely applied to quantify the amount of material incorporated inside MOF(Shearer et al., 2014). The weight loss of UiO-66 majorly happened in two stages. The first weight (22.6%) loss took place at a temperature ranging from 20–100ºC, which was caused by immobilized water evaporation from crystals. Another temperature of lattice breakdown was at 540ºC, where the weight loss of the system was 24.52%. This was caused by benzene and CO_2 fragments changing into the gas phase, indicating the breakdown of the connection between the organic ligand and the inorganic brick as well as the interaction between the carboxyl group and benzene rings. This result is consistent with a previous report, which concluded that UiO-66 was a system with high thermal stability(DeCoste et al., 2013; Katz et al., 2013). Curcumin-loaded UiO-66 showed protection ability for curcumin. Compared with curcumin powder, the decomposition rate of the curcumin-loaded UiO-66 delivery system was significantly slower.

The slope of the decomposition stage was smaller than that of curcumin powder as shown in **Figures 2-5**. This result proved that curcumin was loaded into the delivery system and the UiO-66 delivery system can provide protection to curcumin.

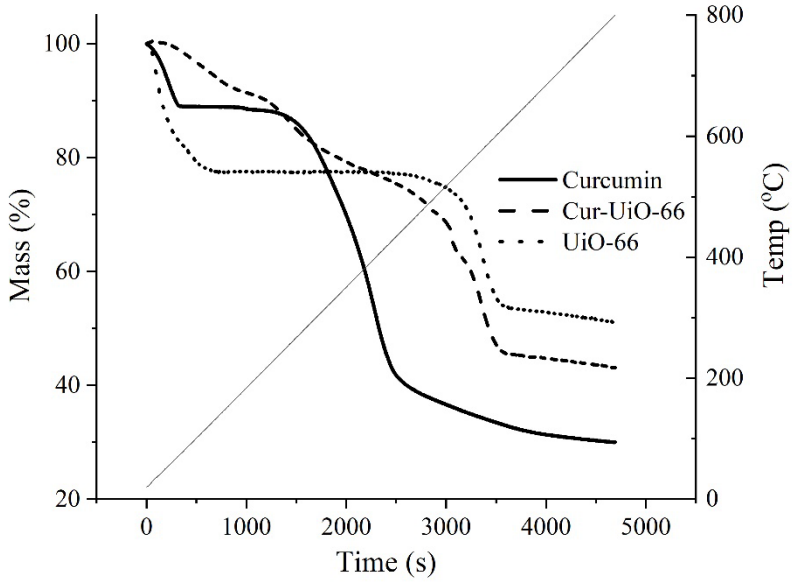


Figure 2-9 TGA curves of Curcumin, UiO-66, and Cur-UiO-66 under dry N_2 gas.

2.4.6 Loading capacity (LC)

Compared with other classical structures, UiO-66 displayed a higher loading capacity(Bai et al., 2016). Curcumin achieved 3.45% w/w loading without further optimization, which was calculated from 426 nm absorbance in **Figures 2-6** (Ma et al., 2017). Currently, liposomes, particles, emulsions are usually suffering from low loading capacities(Wu & Yang, 2017). Methods were developed to improve the loading capacity of these delivery systems, including but not limited to high-pressure, microwave, and ultrasonic methods, etc. But these methods either require a lot of energy input or at a high cost, which makes the practical application of these systems difficult(He et al., 2015). The low loading capacity of the delivery system is mainly determined by the intrinsic characteristics. Therefore, the loading capacity can be

improved not only by processing methods but also by improving the properties of the system itself(He et al., 2015). Since the MOF material is embedded by the voids of the material, there is a significant relationship between the molecular weight of the embedded material and loading capacity(Luo et al., 2016). In previous studies on MOFs, it has achieved the embedding amount of 4.9%, 13.2%, and 22.4% for calcein, caffeine, and 5-Fu, respectively(Cunha et al., 2013; Orellana-Tavra et al., 2015; Tai et al., 2016). The porous characteristics of MOF greatly improved the loading capacity of delivery systems. This characteristic could provide a new approach for improving loading capacity.

Table 2-2 Summary of representative works reported food nanocomplexes as nanocarriers for curcumin

Nanocomplexes	**Loading capacity (% w/w)**	**References**
Caseins	7.0	Pan et al. (2014)
SPI	10.4 (untreated), 14.4 (ultrasound)	Tapal and Tiku (2012)
Soy β-conglycinin	3.0	David et al. (2015)
Whey protein isolate	0.434-1.6 (pH 7-12)	Kevij et al. (2019)
Zein hydrolysate	1.8	Wang et al. (2015)

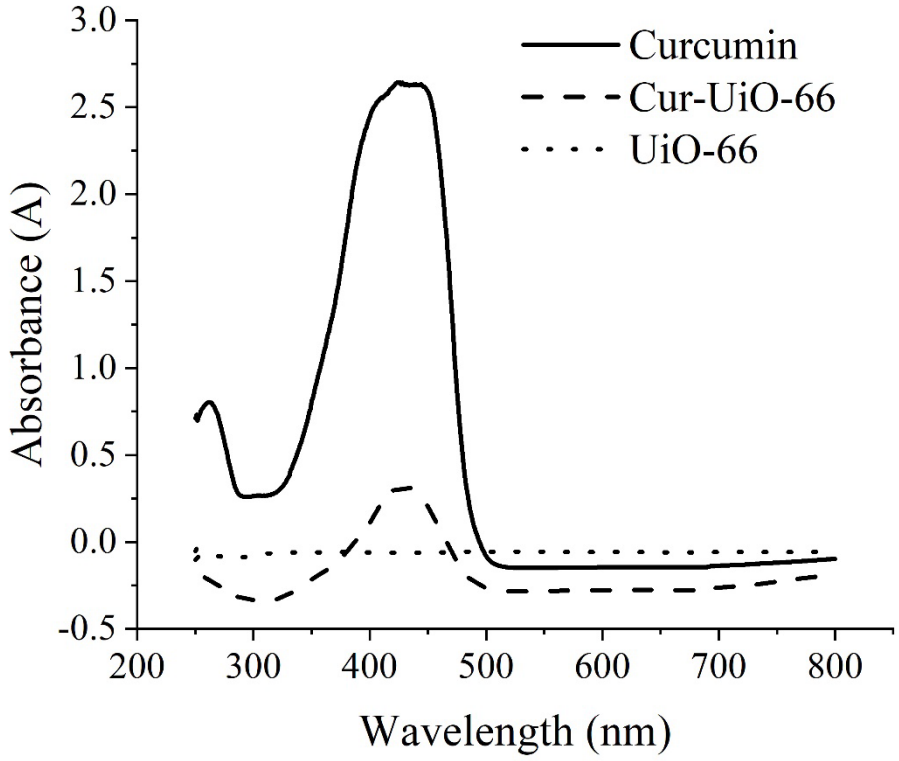


Figure 2-10 UV-visible absorption spectra of curcumin in the presence of UiO-66 suspended in ethanol.

2.4.7 In vitro digestion

Figure 2-7 showed the curcumin release profiles obtained for Cur-UiO-66 during simulated gastric (0 – 60 min) and intestinal (60 – 180 min) digestion. During the two digestion processes, the release speed of curcumin was quite fast in the initial phase of digestion, decreasing with the prolonged digestion time. Over 40% curcumin was still encapsulated after 180 min of digestion, similar trends have been found already for calcein and caffeine in UiO-66. The release time of calcein-loaded UiO-66 achieved sustained release up to 30 days(Orellana-Tavra et al., 2015). The kinetics release behavior of the curcumin delivery system was adjusted using non-linear regressions. According to the data fitting prediction, which was calculated from the first 100 minutes digestion result (r^2 = 0.9986), it was found that 24.76% and 12.07% amounts of curcumins are still not released after 5 hours and 24 hours in SGF and SIF

respectively. Based on this fitting result, the presence of curcumin can still exist in the delivery system after 1 day. In addition to the TGA result, the extended-release time suggested that the UiO-66 structure be stable and effective to protect curcumin within the system. Because UiO-66 is a highly stable MOF, curcumin could be released with the slow breakdown of the structure in an acidic or a high-temperature environment(Orellana-Tavra et al., 2015). Finally, it is possible to detect the curcumin from the curcumin-loaded UiO-66 material, which means that the loading method would not lead to the degradation of curcumin. Combined with previous reports, it is further proved that it is feasible to use UiO-66 to deliver curcumin and achieve controlled release.

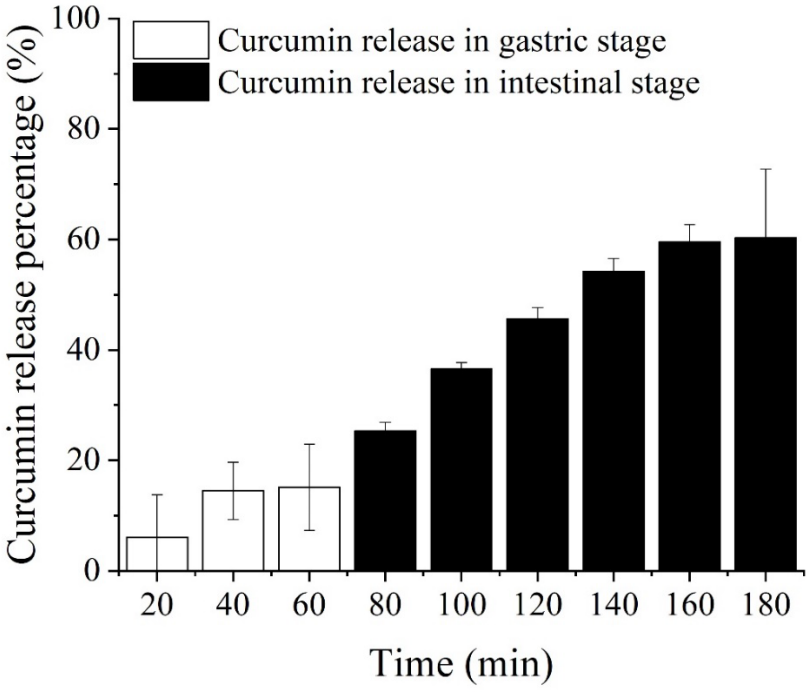


Figure 2-11 Curcumin release from Cur-UiO-66 during the first 3 hours of in vitro digestion.

2.5 Conclusion

In this study, we have successfully loaded and released the model fat-soluble food bioactive ingredient (i.e. curcumin) into the Zr-based MOF UiO-66. Computer simulation tools were involved to predict the material characteristic, including crystal structure, porosity, diffraction, which may help us to interpret the encapsulation mechanism. The crystallinity, morphology, and porosity were characterized by XRD, SEM, EDS, TGA, isotherm measurement. Furthermore, curcumin was loaded into the UiO-66. The loading capacity and release property of the UiO-66 delivery system were evaluated by UV-vis spectrophotometer and an in vitro study. The results showed the Cur-UiO-66 delivery system had a high loading capacity, 3.45% w/w, and the encapsulated curcumin was controlled release for more than 3 hours in a simulated gastrointestinal tract environment. These results proved that UiO-66 could be selected as a suitable carrier for curcumin. Further study may include modifying the UiO-66 MOF structure for improvement of its LC. In addition, Zr-based MOF materials are promising candidates for preparing efficient delivery systems for other bioactive compounds, such as β-carotenoid, quercetin, etc. Finally, other potential applications of MOF material in food systems need to be explored, such as in the area of packaging, catalysis, pathogen detection, etc.

There are several important limitation of curcumin@UiO-66 which hinder the application in food sector, specially the low loading capacity. On the base of curcumin@UiO-66 NPs delivery system, it is important to explore another delivery system based on MOF since the limited loading capacity and encapsulating efficiency. As a possible solusion, the emulsion system, especially the Pickering emulsion system attracted more attention recently which was proved as a high loading capacity and bioavailability for bioactive compound delivery. Besides, there is the lack of machnism of MOF-stablied Pickering emulsion system. Therefore, in next chapter, the curcumin@UiO-66 Pickering emulsion system was discussed.

Chapter 3 Development of UiO-66 nanoparticles as a stabilizer for curcumin loaded Pickering emulsion delivery system

3.1 Abstract

High internal-phase Pickering emulsions (HIPPEs) have taken a center stage in the arena of delivery systems in the food industry because of their high loading capacity and stability. Besides, metal-organic frameworks (MOFs), a type of cutting-edge designable porous scaffolding materials attracted attention in reticular chemistry, which satisfied fundamental demands for delivery research in the past years. Here, we demonstrate a novel metal-organic framework (MOFs) stabilized HIPPE delivery system for the hydrophobic phytochemicals. First, novel high biocompatibility and stable MOF particle, UiO-66-NH_2, was selected from atomic simulation screening, which showed proper electronegativity and amphiphilic properties to develop the HIPPEs system. Monodispersed UiO-66-NH_2 nanoparticles with a particle size of 161.36 nm then were prepared via solvothermal syncretization. Pickering emulsions with inner phase ratios from 50% to 80% with varied contents of polyethylene glycol (PEG) were prepared by *in situ* high-pressure homogenization and their physicochemical properties including crystallography, morphology, and rheology were systematically characterized. Subsequently, curcumin, a model antioxidant, was loaded in the HIPPE system, named cur@UiO-66-NH_2/HIPPE. It exhibited high loading capacity, up to 6.93 ± 0.41%, and encapsulation efficiency (19.76 ± 3.84%). This novel MOF nanoparticle stabilized HIPPE delivery system could be practically utilized for other bioactive components and antimicrobial agents, which would find applications in food safety and biomedical areas in the future.

3.2 Introduction

There has been a breakthrough recently in the development of highly porous materials including, but not limited to, metal-organic frameworks (MOFs), zeolite, and covalent organic frameworks (COFs) (Horcajada et al., 2010), with MOF attracting the most attention. As defined in the Cambridge Crystallographic Data Centre (CCDC) database, MOF is a material "*with a transition metal bonded to an oxygen or nitrogen atom via a polymeric bond*"(Moghadam et al., 2017). In principle, all MOF crystalline structures share similar characteristics, such as tailorable pore sizes, high void fractions, and large surface area. These unique properties have rendered MOF with many applications, including chemical separation, gas storage, catalysis, drug delivery, imaging, 3D printing, biomolecule encapsulation, and battery (Gangu et al., 2016). Until now, the research and applications of MOF in the food field are still limited, mainly due to their instability in water and toxicological and cost considerations. However, the UiO-66 family, named from the University of Oslo, attracted attention since it has high thermal, chemical, water, and mechanical stability due to the strong bonds between the inorganic block and high coordination number (fcc lattices) in the past decades. Besides, it is worth noting that a rich number of studies have been published on UiO-66 toxicity in different cell lines, e.g. human lung epithelial cell (A549), human breast cancer cell (MCF-7), mouse alveolar macrophage cell (MH-S), mouse fibroblast cell (L929), and mouse photoreceptor cell (661W)(Gandara-Loe et al., 2018; Jarai et al., 2020; Su et al., 2019). It was concluded that no acute toxicity was found when cellular uptake was less than 50 μg/mL for 24 h. In addition, the UiO-66 family was synthesized by terephthalic acid with zirconium salt and the benzene ring could be effortlessly modified by different functional groups, such as -OH, -NH_2, -COOH, -Br, which provide an opportunity to optimize the electronegativity and amphiphilic properties suitable for emulsion systems (Ma et

al., 2020; Qiu et al., 2020). It has been applied to the preparation of pharmaceutical delivery systems, e.g. pulmonary drug delivery, pH-responsive drug delivery, and targeted drug delivery.

Pickering emulsions were 3D self-assembly systems that may be formed and stabilized by small organic or inorganic colloidal particles absorbing onto the interface of oil and water (Kim et al., 2017). Many candidates particles could be applied to stabilize Pickering emulsions, including organic particles (e.g. protein) and inorganic particles (e.g. silica). The advantage of silica lies in its low cost and good stability. Previously, it was reported that lipid droplets coated with silica nanoparticles (NPs) decreased the rate of lipid digestion when compared with those coated with proteins (Tikekar et al., 2013). However, emulsions stabilized by protein particles, e.g. zein, β-lactoglobulin, kafirin (Xiao et al., 2017) have shown high biocompatibility and biodegradability, which appeal to consumers seeking clean-labels for food products, but those emulsion systems had inferior stability and bioaccessibility compared to silica-containing counterparts (McClements, 2018). In addition to protein and silica, a broad range of colloidal particles has been applied recently for preparing Pickering emulsions, including graphene oxide (GO), microgels, cellulose, and chitin nanocrystals (Cai et al., 2014; McClements, 2018). Due to the toxicity and water instability concern, few reports tried MOF as a Pickering emulsion stabilizer, and rather rare in the delivery system.

High internal phase Pickering emulsion (HIPPE), also called gel emulsions, is a special kind of Pickering emulsions. In 1966, Lissant first defined the HIPPE system as one with a minimal internal phase volume ratio (ϕ) of the emulsion system of 0.7 (Lissant, 1966). Now, HIPPEs are usually characterized by ϕ higher than 0.64 for the random close packing and 0.74 for the close hexagonal packing (Ikem et al., 2008). HIPPEs have shown many special features, such as high physicochemical stability and high loading capacity for encapsulated bioactive.

Taking those advantages, HIPPEs have been used in various applications, including organic semiconductors, filter membranes, and drug delivery systems (Xu et al., 2018). Several different theories explain the formation and stabilization of HIPPEs. In one theory, phase inversion was required for the formation of HIPPEs, possibly due to the involvement of the homogenization process that improved the uniformity of particles. In another theory, HIPPEs were stabilized by increasing the viscosity of the continuous phase or modifying the surface of colloids, which prevented the absorption of particles onto the interface and thus the formation of regular Pickering emulsions (Ikem et al., 2008). The third theory predicted that HIPPE systems were mechanically stabilized against phase inversion and sedimentation (Menner et al., 2007).

Here, we reported the methodology of computer simulation assistant to design a novel MOF HIPPE system and systematically evaluation of the HIPPE system simultaneously, including morphology, crystallography, morphology, and rheology. To explore the application of MOF-HIPPE system in the food field, curcumin was encapsulated by MOF-HIPPE system. Although this research was still in the early stage of introducing MOF in the food applications, the UiO-66 based HIPPE delivery system showed high stability and loading capability, which represents a potential breakthrough in the food research area.

3.3 Materials & Method

Zirconium tetrachloride (99.5 %), benzene-1,4-dicarboxylic acid (BDC, 98.0%), N,N-dimethylformamide (DMF, 99.0%), Nile red, Polyethylene glycol (PEG, 10,000 kDa), curcumin (95%) and acetic acid (99.9%) were purchased from Sigma-Aldrich (St. Louis, MO, USA). All of the chemicals are in analytical grade.

3.3.1 Computational calculation

Crystal structural units were downloaded from the Cambridge Crystallographic Data Center database (CCDC, https://www.ccdc.cam.ac.uk/). Because the unit-cell structures of Zr-based MOF were very large, the structural units were reduced to eight-unit cells (2*2*2) in Material Studio (version 7.6). The molecular electrostatic potential maps of UiO-66 and UiO-66-NH_2 were performed by density functional theory (DFT) method using $DMol^3$ code. The DFT method in this code uses fast convergent three-dimensional numerical integration to calculate the electrostatic potential. Perdew–Wang 1991 (PW91) is a generalized gradient approximation (GGA) level function and is considered as an adequate precision for this investigation (Liu et al., 2012).

The crystal structure of UiO-66-NH_2 was calculated using the RASPA2 to obtain its mass and density (Dubbeldam et al., 2016). The accessible pore volume, gravimetric surface area (nitrogen), geometric surface area, windows diameter were analyzed by a pyWINDOW (Miklitz & Jelfs, 2018).

The XRD pattern simulation was calculated by a simulation tool, VESTA, with wave angle from 1 to 30 degrees, and relative intensity was set to 1 (Ma et al., 2020).

Grand Canonical Monte Carlo (GCMC) simulations were used to calculate N_2 isotherms at 77 K for UiO-66 and UiO-66-NH_2. At each pressure, the parameter of the equilibration step at 10,000,000 was set as a computer ensemble average. The framework atom was taken from the Universal Force Field (UFF). A charge of -0.482 was placed on the N nuclei and +0.964 at the center of mass. Ewald & Group summation method was used for all interactions with atom-based van der Walls. All calculations mentioned above were based on a sorption isotherm module in Materials Studio. The parameters mentioned above were taken from a previous study with some modifications (Bernini et al., 2014).

3.3.2 Synthesis of UiO-66-NH_2

The UiO-66-NH_2 was synthesized by a solvothermal method according to a previous report with minor modification. First, $ZrCl_4$ (1.17 g, 5 mmol) and 2-aminobenzene-1,4-dicarboxylic acid (NH_2-BDC) (0.90 g, 5mmol), acetic acid 1.0 mL were dissolved in dimethylformamide (DMF) (30 mL) at room temperature. Then, the mixture was placed in a Teflon-lined stainless-steel autoclave after adding 2 ml of de-ionized water and mixing completely. The autoclave was placed in an oven at 120ºC for 24 hours. Afterward, the solution was cooled to room temperature for 30 min, and the resulting UiO-66-NH_2 particles were separated via centrifugation (12,096 × *g*, 10 min) at room temperature and washed three times with ethanol. The resulting white powder was dried in an oven for 4 hours (Chen et al., 2015).

3.3.3 Characterization of UiO-66-NH_2

Crystal structure

X-ray powder diffraction (XRD) patterns were obtained from an XRD diffractometer (C2 Discover Bruker Diffractometer, Madison, WI, USA) with CuKα radiation to evaluate the crystal structure of MOF. X-ray scan ranged from (2θ) 3.5° to 30°, step size at 0.02° (Ma et al., 2020; Su et al., 2015).

Porosity and surface area

The porosity and surface area of MOF was determined using an ASAP 2020 Physisorption Analyzer (Micromeritics Instrument Corporation, Norcross, GA, USA) following a previous study (Chen et al., 2015). Sample tubes were cleaned ultrasonically and dried at 110°C. The MOF samples were loaded into the sample tube for degassing for 24 hours. The sample tube with MOFs was then transferred to the analysis port with N_2 as the adsorptive gas

and liquid nitrogen as the cold medium (Chen et al., 2015). Nitrogen monolayer saturated adsorption capacity, and surface area was calculated following Equation 2-1 and Equation 2-2.

Thermal analysis

Thermal analysis of the UiO-66-NH_2 samples was performed using a thermogravimetric analysis (TGA) instrument (2950, TA Instruments Inc., New Castle, DE). The parameters were modified from a previous study, under a mixed air and N_2 flow of 100 mL min^{-1} (40% air, 60% N_2) with a heating rate of 10 K min^{-1} from 308 K to 1073 K (Oh et al., 2016).

Particle size

Hydrodynamic diameters of UiO-66-NH_2 were measured by a dynamic light scattering (DLS) instrument (BI-200SM, Brookhaven Instruments Corp., Holtsville, NY), which was equipped with a 35mW HeNe laser beam at a wavelength of 637 nm. All DLS measurements were performed three times at 25°C (Zhang et al., 2020). Particle size determination was conducted by diluting the particle with deionized water to 1 mL which was to avoid the multiple light scattering and the impact on the accuracy of measurement.

Surface charge

The electrophoretic mobility was determined at a pH range of 1.0 to 7.0 using a Zetasizer Nano ZS (Malvern Instruments, Worcestershire, UK). Each sample was measured three times in disposable folded capillary cells (DTS 1070, Malvern Instruments Ltd, Worcestershire, UK) at a particle concentration of 0.1 wt%, and at least 32 runs were performed per measurement (Zhang et al., 2020). The pH value was adjusted by adding HCl and NaOH dropwise and measured by a pH meter.

Morphology

A sample powder was dispersed onto an ultra-smooth, round (12 mm diameter), carbon adhesive tabs (Electron Microscopy Sciences, Inc., Hatfield, PA, USA) to 15 mm x 30 mm brass plates and placed into a Quorum PP2000 cryo-preparation chamber (Quorum Technologies, East Sussex, UK) attached to an S-4700 field emission scanning electron microscope (Hitachi High Technologies America, Inc., Dallas, TX, USA). The powder of samples was placed directly into the SEM at 5.0 kV, followed by sputter coating with platinum.

Contact angle

Contact angle measurement was performed by a sessile drop method using an Attention Theta optical tensiometer (Biolin Scientific, Linthicum Heights, MD, USA). The placement of droplets was controlled by a C201 automatic liquid dispenser (Biolin Scientific, Linthicum Heights, MD, USA). An aliquot of 20 μL pure DI water was dropped onto modified gold surfaces. Data collection (60 fps) was manually triggered by the initial contact of a liquid drop with a solid surface. Captured images were automatically analyzed by a One Attention software, Version 1.8 (Biolin Scientific), to identify the baseline and calculate the contact angles.

3.3.4 Emulsion preparation

An oil-in-water (O/W) emulsion was prepared as follows. The continuous phase was prepared by dissolving 0.2 g UiO-66-NH_2 and various polyethylene glycol (PEG, 10% w/w) in 30 mL DI water by vortexing at 3,000 rpm. Different amounts of the dispersed phase (i.e. medium-chain triglycerides, MCTs) were added into the continuous phase. After that, mixtures were sheared to form a coarse emulsion by using a high-speed homogenizer (Ultra-Turrax T25, IKA, Staufen, Germany) at 24,000 rpm for 5 min in an ice bath. The total mass of the system was 15 g (Wei et al., 2019a), with the composition is shown in **Table 3-1**.

Table 3- 2 The 3-factor Box-Behnken design for MOF-HIPPE system

PEG content (% w/w)	MOF content (% w/w)	O:W ratio (% w/w)
0	1	15
0	3	30
0	1	22.5
0	1	30
0	1	15
5	3	30
5	2	22.5
5	2	22.5
5	2	22.5
5	3	15
5	3	22.5
5	1	15
5	1	30
10	2	30
10	2	15
10	1	22.5
10	3	22.5

3.3.5 Characterization of UiO-66-NH_2 Pickering emulsion

Rheological property

The dynamic viscoelastic behavior of HIPPEs was characterized using a HAAKE RS600 Rheometer (HAAKE Co., Germany) with parallel plates (d = 27.83 mm) at 25°C. The gap between the two plates was set to 1.0 mm. For the strain sweep mode, elastic (G′) and loss moduli (G″) were recorded with the strain (γ) changing from 0.002 to 1.0 at a fixed frequency of 1.0 Hz. For the frequency sweep mode, the frequency oscillated from 0.1 to 10 Hz, and all measurements were performed at 0.5% strain, which was within the identified linear viscoelastic region (Wei et al., 2019b).

Low-temperature scanning electron microscopy (LT-SEM)

Samples were scooped into a 10 mm cup and placed into a shuttle, which was frozen conductively, in a Styrofoam box, by placing the brass plates on the surface of a pre-cooled (-196°C) brass bar whose lower half was submerged in the liquid nitrogen. After 20-30 s, the shuttle containing the frozen sample was transferred to a Quorum PP2000 cryo-preparation chamber. The top layer of the frozen sample was cryo-fractured, using a metal blade mounted inside the preparation chamber. All specimens were etched inside the cryo-preparation system to remove any surface contamination (condensed water vapor) by raising the temperature of the stage to -90°C for 10-15 min. Following the etching, the temperature inside the chamber was lowered below -130 °C, and the specimens were coated with a 10 nm layer of platinum using a magnetron sputter head equipped with a platinum target inside the cryo-preparation chamber. The specimens were transferred to a pre-cooled (-130°C) cryo-stage in the SEM for observation. An accelerating voltage of 5kV was used to view the specimens. Images were captured using a 4pi Analysis System (Durham, NC).

Confocal laser-scanning microscopy (CLSM)

A Zeiss LSM710 CLSM (Carl Zeiss Microscopy LLC., Thornwood, NY) system was utilized for observation of the emulsions system. The images were obtained using a Zeiss Axio Observer inverted microscope with 10x 0.45NA and 63x 1.4 NA Plan-Apochromat objectives. A 561 nm diode-pumped solid-state laser was used with a pin hole of 57 μm passing through an MBS 458/514 beam splitter filter with limits set between 540-750 nm. Zeiss Zen 2012 (Carl Zeiss Microscopy LLC., Thornwood, NY) software was used to obtain 7-21 z-stack images, and a maximum intensity projection was used to develop the final image.

Loading capacity (LC)

To achieve a high solubility, 1.5 g curcumin was first added to 100 mL MCT. Then, the mixture was treated with sonication (390 W, 15 min, interval 2 s, Model 505, Fisherbrand, PA, US). Afterward, the mixture was centrifuged for 2 min under 3,000 rpm, and the supernatant was collected (10.02 mg / mL). All the collected solutions were kept at room temperature in the dark for 24 hours before analysis. Aliquots of the curcumin oil solutions and the Pickering emulsions were extracted and diluted 1000 times with 95% alcohol for establishing a standard curve. The blank sample contained 95% alcohol without curcumin. The absorbance at a wavelength of 426 nm for the samples was determined using a UV spectrophotometer (Ma et al., 2018). All determinations were performed in triplicate, and the curcumin content of each sample was calculated according to the standard curve (curcumin in ethanol, standard curve equation: $Y=0.0146X+0.0222$, $R^2=0.9993$).

LC was calculated using **Equation 2-3** for curcumin(Wei et al., 2012).

EE was calculated using **Equation** 3-1 for curcumin

Equation 3-5

$$\text{EE\%} = \left(\frac{Weight\ of\ curcumin\ in\ emulsion\ system}{Weight\ of\ curcumin}\right) \times 100\%$$

3.3.6 Statistical analysis

Data on DLS, zeta-potential analysis, LC measurements were collected from three true triplicates and were reported as the mean ± standard error. Data were analyzed by a one-way analysis of variance using the SPSS 16.0 package (SPSS Inc., Chicago, USA). The significant level was set at p=0.05.

3.4 Results and Discussion

3.4.1 Characterization of UiO-66-NH_2 nanoparticles

The simulated structure of UiO-66 is shown in **Figure 3-1a**. The structure comprises $Zr_6O_4(OH)_4$ octahedrons (formed by in situ via hydrolysis of $ZrCl_4$) bridged by 1,4-benzene dicarboxylate (BDC) linkers. Each cationic $Zr_6O_4(OH)_4$ node is connected with 12 adjacent nodes by BDC linkers. The structure contains two sizes of cavities: 11 Å octahedral cage, and 8 Å tetrahedral cage. Each large cage is shared with eight small ones and edge-sharing with eight additional large ones. This unique structure leads to both high porosity and high stability. According to previous studies, the UiO-66 can be modified by different functional groups at the ortho position of the benzene ring of BDC to generate derivatives such as UiO-66-OH, UiO-66-NH_2, and UiO-66-COOH, which would share the same crystal structure as UiO-66 (Katz et al., 2013).

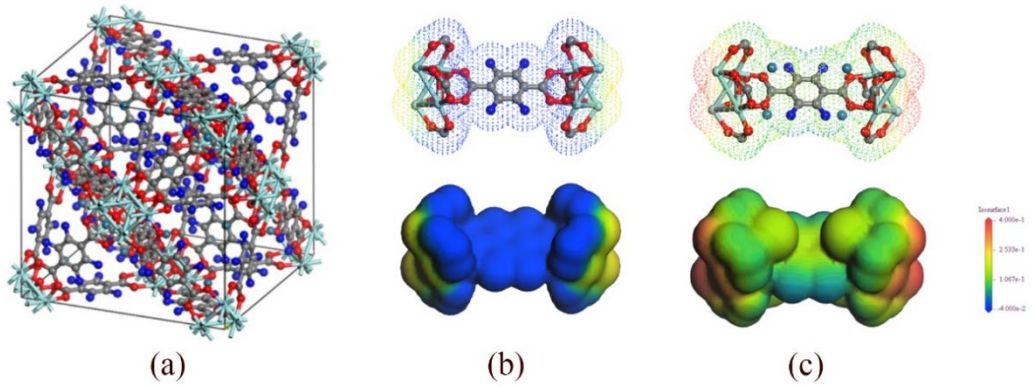


Figure 3-12 (a) A simulation view of the UiO-66 porous structure Carbon: Grey; Oxygen: Red; Zirconium: Bluegreen; (b) Molecular electrostatic potential maps of UiO-66; (c) Molecular electrostatic potential maps of UiO-66-NH_2

It is expected that modification on UiO-66 with amino groups (-NH_2) would increase the electrostatic potential of the molecule surface so that UiO-66-NH_2 particles may be used as a stabilizer for Pickering emulsion systems. To test that hypothesis, we performed a DFT simulation comparison between UiO-66 and UiO-66-NH_2. According to previous reports, it is adequate to describe the intermolecular interactions of MOF by two Zr-node and a single linked ligand, which provides a reasonable balance between accuracy and computational expense using the method in this work (PW91/DNP) (Liu et al., 2012). The molecular electrostatic potential of UiO-66 and UiO-66-NH_2 was shown in **Figures 1b** and **1c**, respectively. The red area represents the place with the most positive electrostatic potential, whereas the blue area denotes the most negative part. It was found that after modification, the positive surface electrostatic potential increased significantly, possibly due to the change of probability-density of electron clouds caused by π–π interactions (Li et al., 2017). Moreover, the increased absolute value of the molecular electrostatic potential enhanced electrostatic repulsion between UiO-66-NH_2 particles, which may indicate a better stabilizing property for Pickering emulsion systems.

Subsequently, UiO-66 and UiO-66-NH_2 were synthesized by the solvothermal method using different BDC ligands (i.e. terephthalic acid and 2-aminoterephthalic acid) under the same condition. The comparison between simulated and experimental XRD results of UiO-66-NH_2 showed that the characteristic peaks were nearly identical, which indicated that the crystal structure of the synthesized product was consistent with expectation (**Figure 3-2a**).

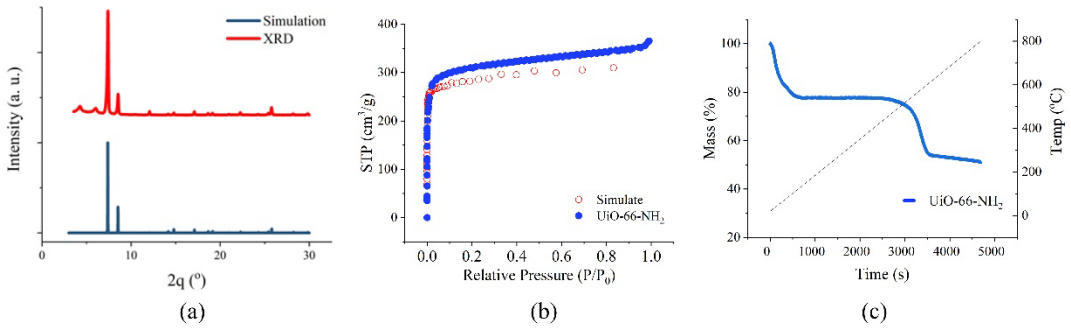


Figure 3-13 (a) PXRD patterns of UiO-66-NH2; (b) N2 adsorption isotherms at 77 K on UiO-66-NH2; (c) Thermogravimetric analysis of UiO-66-NH2;

Figure 3-2b illustrated comparisons between data from simulation and experiment for N_2 absorption of UiO-66-NH_2 nanoparticles. The result from the simulation (1112 m^2/g) was in good agreement with the experimental data (1230 m^2/g). Moreover, the BET surface area obtained in this study was higher than those of other types of water-stable MOF prepared by different metal ions and organic linkers, such as NU-1000 (617 m^2/g) and MIL-68 (584 m^2/g) but lower than HKUST-1 (1451 m^2/g) (Wu & Yang, 2017). Thereafter, through the computer simulation, we have obtained other physicochemical characteristics of UiO-66-NH_2, including molecular weight, density, accessible pore volume, etc. (**Table 3-2**).

Table 3- 3 Computer simulation output of UiO-66-NH2 characteristics

Property	Simulation output
Mass	8720.29 g / mol
Density	1664.06 kg / m^3
Accessible pore volume	0.41836 cm^3 / g
Gravimetric surface area (nitrogen)	1280.36 m^2 / g
Geometric surface area	1550.73 m^2 / g
Stimulate BET surface area	1367.74 m^2 / g
Cavities	11 Å (large)
	8 Å (small)

The thermal stability of UiO-66-NH_2 was tested by TGA. **Figure 3-2c** showed two major weight loss stages for UiO-66-NH_2 nanoparticles. The first weight loss happened at a temperature range below 150°C, which was contributed by the evaporation of immobilized free water from crystal. Another weight loss happened at ca. 550°C, which was ascribed to UiO-66-NH_2 lattice breakdown. These results were consistent with previous reports, which further validated the structures of the synthesized MOF material.

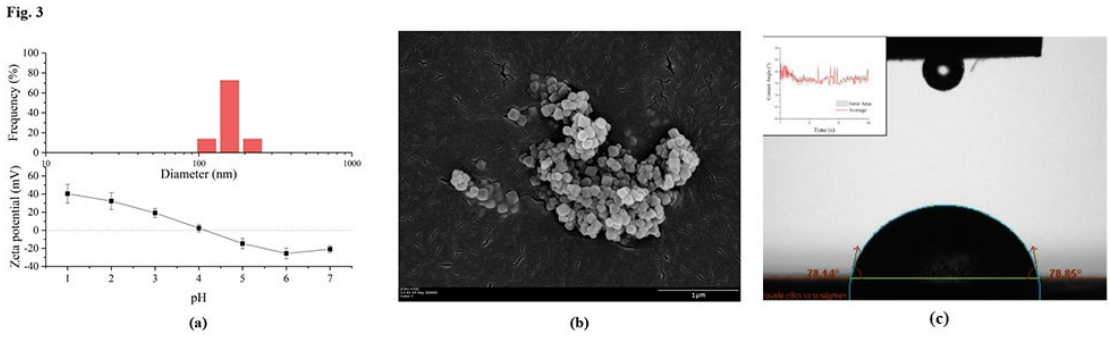


Figure 3-14 Particles size distribution of UiO-66-NH_2(Top); zeta-potential of UiO-66-NH_2 at different pH value (Bottom); (b) SEM images of UiO-66-NH_2; (c) WAC of UiO-66-NH_2

As evident, the particle size of the surfactant plays an essential role in the physicochemical properties of Pickering emulsions. As shown in **Figure 3-3a**, the average particle size of UiO-66-NH_2 was 161.4 nm with a polydispersity index (PDI) of 11.2, which indicated an excellent monodispersity and uniformity of the particles. Furthermore, SEM was applied to measure the particle size and morphology after the sample was freeze-dried (**Figure 3-3b**). A representative SEM image showed that all particles shared a discoid morphology with a particle size in the range of 100-200 nm, which was consistent with the results from the DLS measurement. Meanwhile, UiO-66-NH_2 particles showed clear boundaries in the image, which was in agreement with previous reports (Katz et al., 2013; Ma et al., 2020).

Particles adsorbed strongly to oil-water interfaces, and the energy of attachments depends on the water contact angle, θ_{wac}. As shown in **Figure 3-3c**, the water contact angle (WCA) of UiO-66-NH_2 has stabilized approximately at $78^o \pm 2^o$ for more than 10 s. WCA closer to 90^o, the absorption energy of the particles to the interface of the droplet was closer to its maximum, and the required energy to stabilize the Pickering emulsion system was at its minimum. In practice, particles with WCA lower or higher than 90^o were considered ideal for O/W or W/O Pickering emulsions, respectively (McClements, 2018). Therefore, after modification with amino groups, UiO-66-NH_2 particles with WCA 78^o were deemed suitable for stabilizing O/W Pickering emulsion as compared to some Pickering stabilizers that had WAC as low as 73^o in a previous report (Ojala, Visanko, Laitinen, Österberg, Sirviö, & Liimatainen, 2018), which was expected to reduce the surface tension and stabilize the emulsion.

In addition to particle size and WCA, the electrostatic force was critical in determining the dispersibility of the particles in water and its ability to stabilize the Pickering emulsion (Boire et al., 2019). The results on electrostatic potential calculated from the computer simulation have

been discussed in section 3.4.1. To further confirm this result, we measured the zeta-potential of all treatments in different pH values (**Figure 3-3a**). The pH_{pzc} (point of zero charges) value for UiO-66-NH_2 was ca. 4.0. Compared with other particles around 7.0 or above (e.g. protein, silica, zeolite), UiO-66-NH_2 particles have a stronger positive surface charge at low pH, up to 42 mV.

In summary, UiO-66-NH_2 particles have an acceptable amphiphilic, proper electrostatic attraction, and particle size which contributed to reducing phase separation. Therefore, it is expected that UiO-66-NH_2 nanoparticles were feasible to stabilize the Pickering emulsion.

3.4.2 Pickering emulsion stabilized by UiO-66-NH_2

UiO-66-NH_2 stabilized Pickering emulsion was developed by *in situ* high-pressure homogenization with PEG as depleter. Control experiments showed that without PEG, only Pickering emulsions with a low O:W ratio (less than 50%) was successfully obtained by homogenization. In contrast, with the absence of UiO-66-NH_2, PEG cannot be used alone as an emulsifier to stabilize the emulsion systems (see the control sample in **Figure 3-4a**). Here, the results showed when MOF particles and PEG coexisted and exceeded 0.5% w/w and 5% w/w, respectively, a Pickering emulsion was formed with one-step homogenization. The definition of a HIPPE was when the minimum volume ratio of an internal phase was higher than 0.74 (Ikem et al., 2008). In this study, as shown in **Figure 3-4b**, HIPPE (green dots) was obtained under the following two conditions: 1) PEG was at 0.5 to 5% w/w and UiO-66-NH_2 was higher than 1% w/w; 2) UiO-66-NH_2 was at 0.5 to 5% w/w and PEG was higher than 10% w/w. When either of these two conditions was achieved, HIPPE, with a volume ratio of internal phase at up to 90%, was successfully prepared.

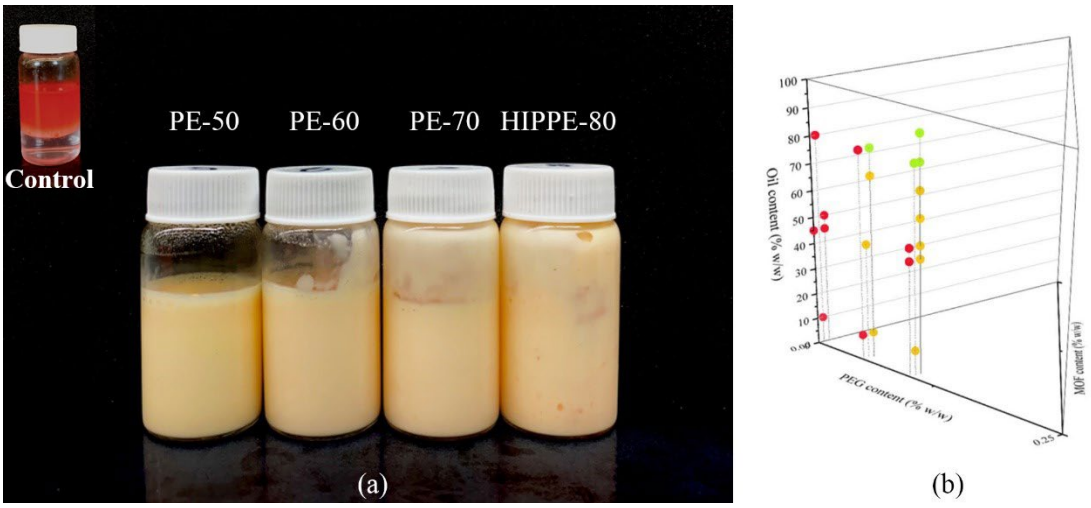


Figure 3-15 (a) Visual appearance of MOF stabilized emulsions at different O:W ratios. (b) The stabilization of HIPPEs that contain various concentrations of PEG and UiO-66-NH_2 particles. Red dot: unstable emulsion; Brown dots: emulsion only; Green dots: HIPPE.

For visual comparison, the emulsion was dyed by dissolving a fluorescent dye (Nile red) in the oil phase. **Figure 3-4a** showed the appearance of Pickering emulsions with the volume ratio of the internal phase at 50%, 60%, 70%, and 80% (hereafter referred to PE-50, PE-60, PE-70, and HIPPE-80, respectively), after 24 hours of storage under ambient conditions. In the control sample (i.e. left upper image), the upper layer was MCT, in which the Nile red dye was dissolved, and the lower layer was a transparent aqueous phase, in which PEG was dissolved and obvious sedimentation and a clear water-oil separation was observed. However, different from the control sample, all other Pickering emulsions maintain homogenized. The disappearance of the apparent red color proved that the oil phase was successfully encapsulated in the emulsion systems. The different amount of wall-mounted emulsion after storage indicated that the mobility of the emulsion was different.

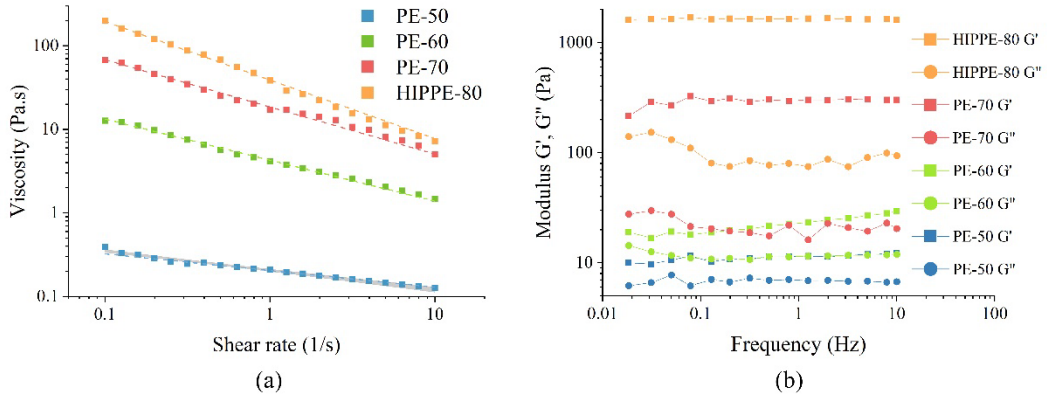


Figure 3-16 (a) Apparent viscosity of Pickering emulsions at different O:W ratios. (b) Storage modulus (G') and loss modulus (G") as a function of angular frequency for the stabilized Pickering emulsions

To better understand the stabilization mechanism, the rheological properties of Pickering emulsions were investigated. For all Pickering emulsions, the apparent viscosity (η) gradually decreased with an increase in the shear rate from 0.1 to 10 s^{-1}, indicating the shear-thinning behavior of all emulsions. As pointed out by Wei et al, the Pickering emulsion system is a type of power-law fluid that follows Ostwald-de Waeel's relationship. The apparent viscosity, η, is given by **Equation 3-2** (Wei et al., 2019b):

Equation 3-6

$$\eta_{app} = K(\frac{\partial u}{\partial y})^{n-1}$$

Where K is the flow consistency index in Pa s^n, $\frac{\partial u}{\partial y}$ is the shear rate or the velocity gradient perpendicular to the plane of shear in s^{-1}, n is the flow behavior index (dimensionless). The experimental data was successfully fitted to the model (**Figure 3-5**), and the K value and the flow behavior index of the four Pickering emulsions were calculated and presented in **Table 3-2**. It can be found that for the MOF-Pickering emulsions, the flow behavior index was always less than 1, which indicated that these emulsion systems were pseudoplastic fluids. At the same time, the value of n decreased with the increased O:W ratio. One plausible explanation was that for both normal Pickering emulsion and HIPPE, UiO-66-NH_2 particles generated a concentrated

form, which means that even under low inner phase conditions, particle-filled weak gels were formed within the system. With the increase of dispersion phase concentration, the network of aggregated droplets, which contain a long-chain polymer (PEG) at a high O:W ratio, endowed the system with high viscosity (Kim et al., 2017). This hypothesis is also supported by the flow consistency index (K). The K value increased significantly as oil content increased (e.g. K = 4.3, 18.5, and 38.8 for PE-60, PE-70, and HIPPE-80, respectively) (**Table 3-2**), suggesting a dramatic increase in viscosity.

Table 3- 4 Fitting results of emulsion rheology analysis based on Ostwald–de Waele model

	PE-50	**PE-60**	**PE-70**	**HIPPE-80**
K	0.204	4.276	18.509	38.833
n	0.800	0.508	0.436	0.300

K is the flow consistency index

n is the flow behavior index (dimensionless)

Dynamic oscillatory data with different O:W ratios were shown in **Figure 3-5b**. With increased angular frequency, neither shear storage nor shear loss modulus changed significantly. The damping ability of a system (i.e. the ratio of storage modulus to loss modulus, tanδ) decreases significantly with increasing O:W ratio. Besides, the sample with a higher O:W ratio showed a smaller tanδ value, which could be attributed to the loss modulus being lower than its storage modulus in the HIPPE system. As shown in Figure 5b, the damping ability decreased rapidly as the O:W ratio increased from 60% w/w to 70% w/w. Moreover, after the formation of the HIPPE system, the value of tanδ decreased far from 1, which suggested increased pseudoelasticity. It is worth noting that previous reports suggest the viscosity does not play a

predominant role in stabilizing the HIPPE system (Xu, Liu, & Tang, 2019; Xu et al., 2018). Combining the previous discussion of emulsion viscosity, at the relatively low ratio of O:W (<60% w/w), viscosity was essential for emulsion stability. However, with the increase of emulsion O:W ratio, especially from 60% to 70% w/w, the interaction between droplets in the system rapidly increased, and the effect of viscosity on emulsion stability was significantly reduced.

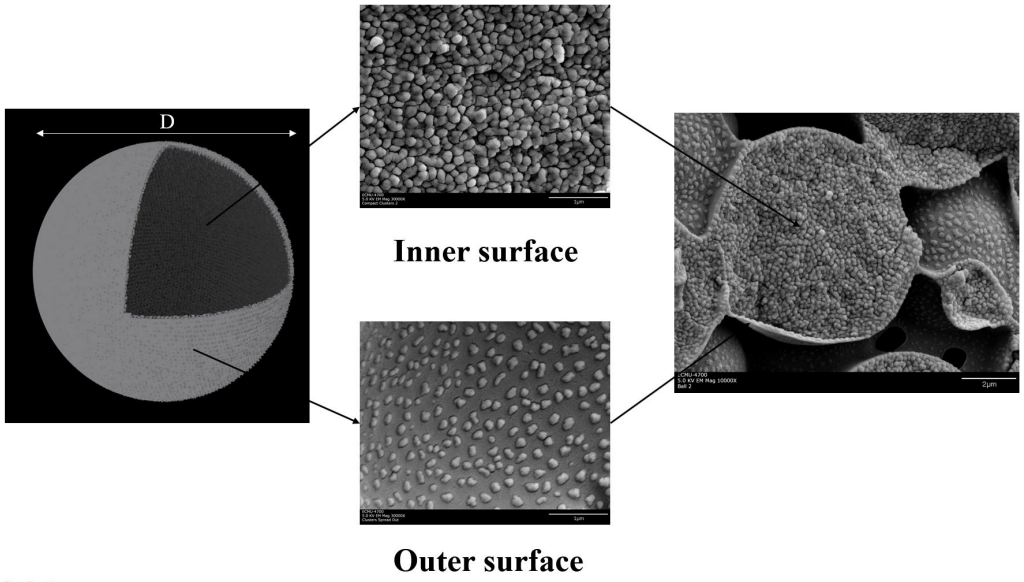


Figure 3-17 SEM images of MOF-HIPPE droplets with the theoretical model. The left figure showed the theoretical Pickering droplet model and the right was image from SEM. Middel upper image showed the droplet interface from internal view and middle bottom image showed the droplet interface from outer view.

Studies have demonstrated that the HIPPE system was a bridging hydrogel network, in which the droplet interface was a monolayer between droplets to droplets. The result was confirmed by the LT-SEM result, in which the diameter of droplets was around 10 μm (**Figure 3-6**). In general, the jamming packing effect was proportional to effective volume fraction and the ratio of interface thickness to droplets size. Since the ratio of interface thickness to droplet size was less than 5%, the enhanced jamming packing due to the increase of the effective volume fraction would be negligible under this condition. Therefore, one possible explanation was that in

the process of the system changing from a Pickering emulsion system to a HIPPE, the depletion interaction brought by PEG plays a vital role in the process of stabilizing the system to overcome the phase inversion of emulsion (Kim et al., 2017).

Depletion interaction was a type of physical interaction that facilitates hydrophilic particles absorption to the droplet interface, which was induced by the presence of co-solvents (Hinrichs, Himstedt, & Dorfs, 2018; Kim et al., 2017). When both large UiO-66-NH_2 particles and small PEG depletants were in a suspension, the region that surrounds every large MOF particle was unavailable for the centers of the PEG to occupy. During the homogenization process, although depletion attraction tends to flocculate the particles, when the two particles were close enough, the strong repulsive interaction between the particles helps particles stay individually (calculated from DLVO Model). At the same time, due to the strong external force in the system during the homogenization, the UiO-66-NH_2 particles tend to stabilize on the surface of the oil droplet led to reducing the surface tension.

In order to investigate the changes of the interface during the formation of HIPPE, we took confocal microscopy images of representative regimes from PE-60, PE-70, and HIPPE-80 and named them regime-1, regime-2, and regime-3, respectively (**Figure 3-7**). In the case of regime-1, which denotes a low internal phase, the distance between the adjacent droplets in the system was large, and the exclusion volume was formed by the electrostatic force and Van der Waals force outside the droplets. The droplet motion under this condition was mainly affected by the viscosity of the continuous phase. With the increased O:W ratio, the volume of non-exclusion volume areas in some parts of the system decreased, and the overlap of exclusion volume began to occur near the interface of the adjacent droplets, which became regime-2. In this region, due to the effect of depletion attraction brought by PEG, MOF particles were stabilized at the interface.

Therefore phase inversion would not happen. With the amount of oil phase increasing continuously, the contact area between the two interfaces merges to form a mono-isolation layer. Eventually, any two adjacent droplets in the system were forced to form a tightly packed emulsion structure, leading to the formation regime-3. In this regime, droplets were surrounded by the MOF particles layer, which stabilizes the emulsion mechanically and prevents sedimentation.

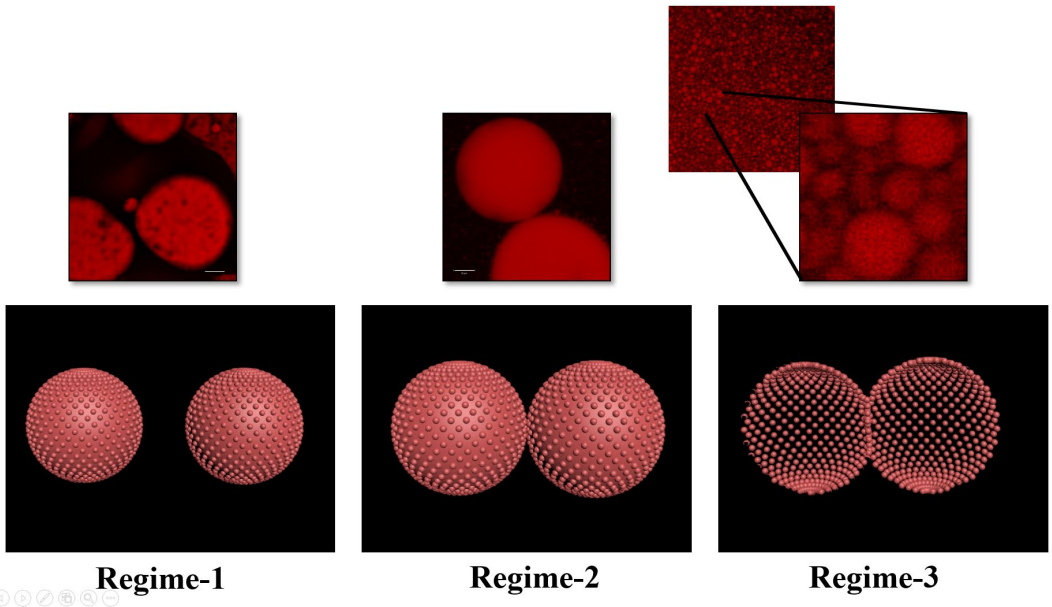


Figure 3-18 Representative confocal laser scanning microscopy (CLSM) images of the HIPPE in different regimes. Upper three images was imaged by CLSM from representative regime and the bottom three images was mapping to their theoretical model.

3.4.3 Loading capacity of MOF-HIPPE system

HIPPE emulsion system was prepared under the O:W ratio higher than 80% w/w, which suggests the possibility of a high payload of oil-soluble compounds such as curcumin. In principle, the loading capacity (LC) and encapsulation efficiency (EE) of curcumin were positively related to O:W ratio of the Pickering emulsion system. The LC of curcumin in the UiO-66-NH_2 stabilized HIPPE was measured at 6.93 ± 0.41 %, and EE of the system was 19.76 ± 3.84%, significantly higher than the conventional Pickering emulsion systems (i.e. PE-70 and

PE-80). When compared to other emulsion systems, the loading capacity was relatively low, this may be due to the amphiphile of the UiO-66-NH_2 NPs. As mentioned before, the WCA of UiO-66-NH_2 NPs was 78º, which indicated that they were more hydrophobic than other stabilizers, e.g. protein and silica dioxide. The EE showed a significant correlation to the WCA. When WCA was closer to 90º, the system would show a higher EE (see section 3.3.1).

At present, one of the main disadvantages of the Pickering emulsion system for food application was suffered from low LC and EE. As expected, compared with protein stabilized traditional Pickering emulsion, MOF-HIPPE system showed higher loading capacity. For example, the LC for octenyl succinic anhydride (OSA) quinoa starch Pickering emulsion was 0.0016 wt% (Marefati et al., 2017), and 0.0005 wt% for kafirin Pickering emulsion (Xiao et al., 2015) with *in situ* homogenization. The high LC and EE value of the MOF-HIPPE system can be attributed to two reasons below: a. the high internal phase system could load more dispersed phases with dissolved saturated curcumin due to the high water-oil ratio; b. the MOF particle itself was highly porous materials, so the particles themselves provide loading capacity and therefore the loading was further increased. In summary, as we selected a water-stable and high bio-affinity MOF material, this shed light for further expansion of novel reticular materials for food applications in the future.

Table 3- 5 Composition of emulsion for delivery of curcumin

Emulsifier	Oil (% w/w)	Loading capacity (% w/w)	References
Tween-80	Corn oil (10)	0.00278	Zheng el al., 2017

Bovine serum albumin - dextran conjugate (BSA-dextran)	MCT (20-40)	0.22-0.56	Wang et al., 2016
Casein - soybean soluble polysaccharide complex (CN/SSPS)	MCT (16.7)	0.15	Xu et al., 2017
Kafirin	Vegetable Oil (0.2–0.8)	0.0005-0.002	Xiao et al., 2015
OSA quinoa starch granules	MCT (7)	0.0016	Marefati et al., 2017
Chitosan-tripolyphosphate nanoparticles	MCT and LCT (5–50)	0.1	Shah et al., 2016
Colloidal silica	Canola Oil (5)	0.0046	Tikekar et al., 2013

3.5 Conclusion

In this study, for the first time, with the help of computational simulation, we have established a hydrophobic bioactive compounds-loaded MOF-HIPPE system. With the assistance of simulated computation, UiO-66-NH_2 was optimized for stabilizing O/W Pickering emulsions due to its evenly distributed positive surface potential and amphiphilic properties. The solvothermal method was applied for the facile synthesis of monodisperse UiO-66-NH_2 particles with a particle size of 161.36 nm. Experimental results on crystal structure by XRD, porosity by

BET, particle size and zeta-potential by DLS, and morphology by SEM showed high consistency with simulation expectations. Pickering emulsion systems with different contents of MOF particles and PEG, and O:W ratios were prepared by an *in situ* homogenization. Afterward, rheological and morphological studies demonstrated that increasing the viscosity of the continuous phase and enhancing depletion attraction helped to stabilize the Pickering emulsions and prevent phase inversion during internal phase ratio increased. Finally, curcumin was encapsulated into the newly prepared MOF-HIPPE system and achieved a higher LC and EE compared with other food Pickering emulsion delivery systems, up to 6.93 ± 0.41 % for LC, and 19.76 ± 3.84 % for EE. This UiO-66-NH_2 stabilized HIPPE system was a successful example to develop other MOF-HIPPE systems and a similar strategy may be useful to create more hierarchical structures based on novel highly porous materials for food applications. The next step, the effect of a single factor, the stability and toxicology of the system, and application in the food industry need to be explored.

Chapter 4 Optimization curcumin loaded UiO-66 Pickering emulsion delivery system

To reach the maximum loading capacity and encapsulation efficiency,in this chapter, response surface methodology was applied to optimize the UiO-66 Pickering emulsion system.

4.1 Abstract

Ultrasound-assisted preparation of a curcumin-loaded metal-organic framework (MOF) UiO-66-NH_2 stabilized Pickering emulsion systems was carried out in this study. A 4-factor-3-level Box-Behnken design (BBD) and response surface methodology (RSM) analysis were employed to systematically evaluate the effect of different experimental parameters (i.e., ultrasonic power, ultrasonic time, oil content, and MOF content) on curcumin loading capacity (LC) and encapsulation efficiency (EE). The results indicated that ultrasonic power and MOF content significantly affected LC and EE, whereas ultrasonic time and oil content had little effect. A mathematical model for optimizing the preparation of emulsion systems was established. Based on the ridge max analysis, an optimal condition for the newly developed curcumin-loaded MOF-Pickering emulsion was identified, i.e., ultrasonic power 150W, ultrasonic time 11.17 min, oil content 20.0%, and MOF content 1.10%. At this condition, the LC and EE of curcumin obtained from the experiment reached 7.33±0.54% and 56.18±3.03%, respectively, which were within the prediction range of LC (7.35±0.29%) and EE (54.34±2.45%). The emulsion systems created in this study may find new applications for the delivery of bioactive compounds in food and pharmaceutical areas.

4.2 Introduction

Ultrasound is widely applied in cell disruption, chemical syntheses, extraction, and emulsification in the food industry because it can homogenize and form a high viscosity system

with a uniform droplet size distribution(Sui et al., 2017). The versatility of ultrasound refers to its wide effective frequency region that allows controlling the cavitation intensity and the number of cavitation events of the system (Leong et al., 2017). The mechanism of ultrasound homogenization has been illustrated as follows: high-energy ultrasonic waves generate cavitation in a liquid solution, and subsequent collapses of the cavitation bubbles are facilitated by stirring and thorough mixing of the solution(Leong et al., 2017). The ultrasonic method has been proven effective at preparing highly stable emulsions, polymeric particles with environmental sensitivity (i.e. sensitivity to light, heat, and pressure), and microspheres for encapsulating bioactive compounds(Johansson et al., 2016).

Ultrasonic-assisted preparation of Pickering emulsion systems has attracted attention recently. Pickering emulsion is a special category of emulsions stabilized by solid particles of emulsifiers located at the oil-water interface, and it has been discovered a century ago but only studied extensively recently(McClements, 2018). When compared to the traditional emulsion system, Pickering emulsions usually have better stability since solid particles at the interface prevent the emulsion from coalescence. Previous studies have used ultrasonic-assisted homogenization to prepare Pickering emulsions from solid particles with various origins, for example, polyaniline/nano-ZnO composites, Fe_3O_4 nanoparticles, cellulose nanocrystals(Leong et al., 2017; Meroni et al., 2020; Sui et al., 2017).

On the other hand, metal-organic frameworks (MOFs), a class of hybrid porous materials with uniform structures, have been studied due to their high porosity and tunable physical and chemical properties(Wang et al., 2019) and have the potential to be used as stabilizers for Pickering emulsions. In an early stage, MOFs' application has been limited to catalysis, separation, and storage of gas mixture, whereas it has been expanded to include hazardous

material adsorption, new catalysis, and biomedical applications(Shen et al.). To date, MOFs have demonstrated their versatility by being specifically tailored and have been reported for applications in different food sectors, including food packaging, contaminants' detection, and antibacterial delivery(Y. Wu et al., 2019). Meanwhile, with an in-depth understanding of MOFs as a porous material, low toxicity MOFs have been designed as drug delivery vehicles and tissue imaging agents(Kagan, 2016). Some MOFs have been found to show little adverse effects in the host during the test and display good biocompatibility(Dong et al., 2017). Since the first structure was reported in 1976, more than 80,000 MOFs' structures were added in the Cambridge Crystallographic Data Centre (CCDC), known as the world's repository of small molecule crystal structures, and the number of collates increased dramatically in the past decade (Bobbitt et al., 2017; Moghadam et al., 2017). The simplest form of MOFs' structure is 1,4 benzene dicarboxylic (BDC) linkers connected to zinc, copper, or zirconium salts/oxides by a carboxyl group. The well-known examples are IRMOF-1, HKUST-1, and UiO-66 and their derivatives(Furukawa et al., 2010; Gomez-Gualdron et al., 2016). Among them, UiO-66 and its derivatives are usually used as a model material for studying MOFs' structures because of their facile synthesis, simple structures, and typical physicochemical properties. The UiO-66 family as model MOFs has been applied to many aspects of research, include but are not limited to the use of synthesis control, group modification, toxicology evaluation, and delivery systems(Li et al., 2017). In recent years, many reports utilized the MOFs as a delivery system due to their high porosity. Meanwhile, due to the strong surface charge of MOF particles, they may be utilized to prepare stable emulsions preventing droplet coalescence and aggregation, but the research on applying MOFs as a stabilizer for Pickering emulsions is still in an early stage(Orellana-Tavra et al., 2015).

In general, emulsion delivery systems stabilized by solid particles (i.e. SiO_2 and protein) instead of surfactants are recognized as “Pickering emulsions”. Compared to conventional emulsion delivery systems, Pickering emulsion showed desirable characteristics such as the fewer amount of emulsifiers and better stability due to their coalescence, which facilitated their applications in the cosmetics, pharmaceutical, and food industries. Among these Pickering emulsion systems, curcumin loaded Pickering emulsion delivery system attracted attention in food scope recently. Curcumin, a representative phytochemical compound, has been reported for various benefits, including cancer prevention and neuroprotection. However, the low water solubility, photosensitive, and poor oral bioaccessibility of curcumin seriously limited its application as an attractive food colorant or a dietary supplement. To address this challenge, various delivery systems have been demonstrated to expand the applicability of curcumin, and encapsulating lipophilic curcumin with Pickering emulsion-based delivery systems proves to be a useful means to surmount the disadvantages of curcumin.

The exploration of novel, stable, and functional Pickering emulsion systems using different stabilizing materials has been a hot topic of research in past decades. In this study, for the first time, we reported an ultrasound-assisted MOF-Pickering emulsion system for encapsulating curcumin (a representative bioactive compound for testing Pickering emulsion characteristics). Medium-chain triglycerides (MCTs) were selected as a dispersed phase, UiO-66-NH_2 was used as the stabilizer, and curcumin was loaded in MCTs with ultrasonic solubilization. The effect of experimental conditions (i.e. ultrasonic power, ultrasonic time, oil content, and MOF content) on the responsive results (i.e. loading capacity and encapsulation efficiency) was analyzed using a Box-Behnken design (BBD) and response surface methodology

(RSM). Attempts were made to obtain optimal conditions for the curcumin-loaded UiO-66-NH_2 stabilized Pickering emulsion.

4.3 Materials and methods

4.3.1 Materials

Zirconium tetrachloride ($ZrCl_4$, 99.5 %), benzene-1,4-dicarboxylic acid (BDC, 98.0%), N,N-dimethylformamide (DMF, 99.0%), ethyl alcohol (99.5%) polyethylene glycol (PEG, m.w. 10,000 Da), curcumin (99.5 %), medium-chain triglyceride (MCT), and acetic acid (99.9%) were purchased from Sigma-Aldrich (St. Louis, MO, USA). All of the chemicals are in an analytical grade.

4.3.2 Experimental design

A 3-level-4-factor BBD, including 29 experiments, was employed in this study. To avoid bias, 29 runs were performed in random order. The variables and their levels selected for preparation of MOF-stabilized emulsion were ultrasonic power 50 – 150 W, ultrasonic time 5 – 15 min, MCTs content 15 – 30% w/w, and UiO-66-NH_2 content 1 – 3% w/w. All experiments were performed in a 30 g system. **Table 4-1** shows the independent factors (x_i), and their levels.

Table 4- 6 Box-Behnken design (3-level-4-factor) for curcumin-loaded Pickering emulsion delivery system and response surface analysis of experimental data.

No.	Factors				Responses			
	Ultrasonic Power (W)	Ultrasonic Power (min)	Oil content (% w/w)	MOF content (% w/w)	Loading capacity (%)	S.D.	Encapsulation efficiency (%)	S.D.
1	100	10	30	3	4.86	0.38	17.93	0.10
2	100	5	22.5	3	6.79	0.23	19.36	4.78
3	150	5	22.5	2	5.33	0.30	32.89	1.48
4	100	15	15	2	7.01	0.41	30.01	0.30
5	100	15	22.5	1	2.31	0.17	54.73	1.45
6	100	10	30	1	1.61	0.11	50.27	4.28
7	100	5	30	2	3.56	0.23	28.71	3.19
8	50	5	22.5	2	4.30	0.18	26.53	3.79
9	150	10	22.5	3	6.93	0.41	19.76	3.84
10	100	10	22.5	2	5.05	0.34	31.17	3.21
11	100	10	15	3	8.87	0.57	17.86	4.39
12	150	10	30	2	3.85	0.05	31.02	4.86
13	100	10	22.5	2	4.96	0.03	30.62	4.11
14	100	10	22.5	2	5.10	0.16	31.46	0.73
15	150	10	15	2	7.15	0.57	30.59	0.67
16	100	15	22.5	3	6.89	0.02	19.67	3.06
17	50	10	22.5	1	2.26	0.14	53.41	3.17

18	100	10	22.5	2	5.14	0.16	31.68	4.91
19	100	5	15	2	6.30	0.41	26.96	2.80
20	100	15	30	2	3.38	0.17	27.19	3.50
21	150	10	22.5	1	2.47	0.04	58.41	0.59
22	50	10	30	2	3.35	0.25	26.95	3.56
23	50	15	22.5	2	4.25	0.35	26.22	3.82
24	50	10	15	2	6.17	0.13	26.39	0.25
25	150	15	22.5	2	5.26	0.40	32.43	4.40
26	50	10	22.5	3	6.35	0.40	18.11	2.46
27	100	5	22.5	1	2.29	0.17	54.24	0.92
28	100	10	15	1	3.49	0.26	56.28	3.08
29	100	10	22.5	2	5.08	0.13	31.33	3.65

4.3.3 Synthesis of UiO-66-NH_2

The UiO-66-NH_2 was synthesized according to a previous report with a minor modification(Ma et al., 2020). First, $ZrCl_4$ (1.17 g, 5 mmol), BDC (0.90 g, 5mmol), and acetic acid (1.0 mL) were dissolved in DMF (30 mL) at room temperature. Then, the mixture was placed in a Teflon-lined stainless-steel autoclave after adding 2 ml of de-ionized (DI) water and mixed completely. The autoclave was heated in an oil bath at 120°C for 24 h. Afterward, the solution was cooled down at room temperature for 30 min, and the resulting UiO-66-NH_2 particles were separated via centrifugation (12,096 × g, 10 min) at room temperature and washed three times with ethanol. The resulting white powder was obtained by drying the particles in an oven for 24 h(Ma et al., 2020). The particle size of synthesized UiO-66-NH_2 was 161.36 nm, measured by a dynamic light scattering (BI-200SM, Brookhaven Instruments Corp., Holtsville, NY) with crystal structure verified by an X-ray diffraction (XRD) diffractometer (C2 Discover Bruker Diffractometer, Madison, WI, USA).

4.3.4 Emulsion Preparation

The ultrasound can be categorized into three different regions along the frequency spectrum: power ultrasound region (16-100 kHz), intermediate ultrasound region (100-1000 kHz), and ultra-high frequency ultrasound region (above 1000 kHz)(Johansson et al., 2016). In the power ultrasound region that was used in this study, the radius of cavitation bubbles during homogenization can be calculated using the Equation 4-1:

Equation 4-7

$$R_r = \sqrt{\frac{3\Upsilon p_\infty}{\rho_L \omega^2}}.$$

Where Υ is the specific heat ratio of the gas(Li et al., 2017) inside the bubble, p_∞ is the ambient liquid pressure, ρ_L is the liquid density, and ω is the angular frequency of ultrasound. In practice, the size of an active bubble is expressed as $R_r \approx 3/F$, where F is the frequency of the ultrasound. In the power ultrasound region, ultrasound delivers high energy into the solution, converting it to localized shear force and increased temperature. The energy density of the solution could be as high as 1000 w/cm^2 and is directly influenced by the input power(Leong et al., 2009).

Briefly, 1.5 g of curcumin was dissolved in 200 mL MCTs as a stock solution, and it was treated with ultrasound (Model 505, Fisherbrand, PA, US) in the conditions of a one-second interval and under 20 kHz, 390 W for 30 min. After centrifugation, the supernatant was collected as the oil phase (dispersed phase). The parameters of preparing curcumin-loaded emulsion have been optimized in our previous report(Ma et al., 2018). The mixture of different concentrations of UiO-66-NH_2 with 10% w/w PEG (as depleter) in water was vortexed and then treated with an ultrasound in the conditions of one-second interval and 390 W for 15 min. The solution was kept at room temperature for 24 h as the continuous phase. An oil-in-water (O/W) Pickering emulsion was prepared as follows. Different amounts of dispersed phase were added into the continuous phase. After that, mixtures were sheared to form a coarse emulsion by using a high-speed homogenizer (Ultra-Turrax T25, IKA, Staufen, Germany) at 24,000 rpm for 5 min. The obtained coarse emulsions were treated with the high-energy ultrasonic wave at different powers (50 – 150 W) for a different period of time (5 – 15 min) using a sonic dismembrator (Model 505, Fisherbrand, PA, US) in an ice bath. The total mass of the system was 30 g(Ma et al., 2017).

4.3.5 Encapsulation properties

The content of curcumin within the Pickering emulsion was analyzed using a reported method(Chen et al., 2020). Briefly, curcumin was extracted by MCT with the ultrasonic-assisted method, then its concentration was obtained from a standard curve using a UV−visible spectrophotometer (Beckman Coulter, Brea, CA, USA) at 426 nm (curcumin content in MCT stock was 10.07 mg/L). The loading capacity (LC) and encapsulation efficiency (EE) of curcumin were calculated by **Equation 2-3** and **Equation 3-1**, respectively:

4.3.6 Statistical analysis

All data were performed in triplicate and values were expressed as the mean ± standard deviation. The experimental data (Table 1) were analyzed by the response surface regression (RSREG) using the SAS software to fit the following second-order polynomial **Equation 4-2**:

Equation 4-8

$$Y = b_0 + \sum_{i=1}^{4} b_i x_i + \sum_{i=1}^{4} b_{ii} x_i^2 + \sum_{i=1}^{3} \sum_{j=i+1}^{4} b_{ij} x_i x_j,$$

where Y is the response (percent of molar conversion);

b_0 is a constant,

b_i, b_{ii} and b_{ij} are coefficients;

x_i and x_j are the uncoded independent variables.

The options of RSREG SAS and RIDGE MAX were employed to compute the estimated ridge of maximum response for increasing radii from the center of the original design(Chen et al., 2011).

4.4 Results and discussion

In order to systemically investigate and optimize the influence of ultrasonic power, ultrasonic time, oil content, and UiO-66-NH_2 content on LC and EE of the Pickering emulsions, a 3-level-4-factor BBD was applied, and a total of 29 treatments were carried out. RSM was then

applied to analyze the experimental data. The results of the curcumin LC and EE are shown in Table 1. Of the total 29 treatments, treatment #4 (ultrasonic power 100W, ultrasonic time 15 min, oil content 15.0 %, MOF content 2%) resulted in the highest LC (7.01±0.41%) and treatment #21 (150W ultrasonic power, 10 min ultrasonic time, 22.5% oil content and 1% MOF content) resulted in the highest EE (58.41± 0.95%), whereas treatment #6 (ultrasonic power 100W, ultrasonic time 10 min, oil content 30.0% and MOF content 1%) resulted in the lowest LC (1.61±0.11%) and treatment #11 (ultrasonic power 100W, ultrasonic time 10 min, oil content 15.0% and MOF content 3%) resulted in the lowest EE (17.86±3.17%).

In addition, the RSREG procedure, which calculated least squares to fit quadratic response surface regression models from SAS, was employed to fit the second-order polynomial. **Equation 4-3** and **Equation 4-4** were thus generated and given as below:

Equation 4-9

$$Y_{LC}(\%) = (0.0440 + 0.0172X_1 + 0.2419X_2 + 0.2901X_3 + 1.2325X_4 - 0.0051X_2X_3 + 0.0174X_2X_4 - 0.0062X_2^2 - 0.0062X_3^2 - 0.3910X_4^2) \times 100\%$$

Equation 4-10

$$Y_{EE}(\%) = (0.6352 + 0.1263X_1 + 1.5573X_2 + 1.5314X_3 - 47.1652X_4 - 0.0168X_1X_4 - 0.0305X_2X_3 + 0.2027X_3X_4 - 0.0406X_2^2 + 6.6207X_4^2) \times 100\%$$

Analysis of variance (**Table 4-2**) indicated that this quadratic polynomial model was highly significant and adequate to represent the actual relationship between variables and response factors. For LC, the p-value was <0.0001, and R^2 was 0.9017. For EE, the p-value was <0.0001, and R^2 was 0.9965.

Table 4- 7Analysis of variances for the variables in the preparation of the Pickering emulsion pertaining to response LC and EE.

Response factor	Model	Degree of freedom	p-value	Std. deviation	R^2
LC	Linear	20	0.0056	3.4853	0.4432
	2FI	14	0.9022	3.8099	0.5009

	Quadratic	10	< 0.0001	1.9172	0.9017
	Cubic	2	0.0138	0.9031	0.9906
EE	Linear	20	< 0.0001	4.1877	0.9027
	2FI	14	0.9911	4.7351	0.9067
	Quadratic	10	< 0.0001	1.0366	0.9965
	Cubic	2	0.0066	0.4280	0.9997

A joint test was further used to analyze the overall effect of four synthesis variables on LC and EE. As shown in **Table 4-3**, ultrasonic power (X_1) affected LC significantly. Meanwhile, ultrasonic power (X_1) and MOF content (X_4) in the range of 50-150 W and 1-3 % w/w, respectively, affected the EE significantly ($p<0.1$). Moreover, the p-value of MOF content (X_4) for LC and oil content (X_3) for EE was only slightly higher than 0.1, with a non-negligible improvement of the estimated results. Ultrasonic time (X_2) did not show a significant effect on the LC and EE.

Table 4- 8 Analysis of variances for preparation of the delivery system by a joint test.

Response factor	Factor	Sum of Squares	Prob. >F-value
LC	Ultrasonic Power (x_1)	18.5340	5.0422
	Ultrasonic Time (x_2)	0.6960	0.19
	Oil phase concentration (x_3)	2.9304	0.8
	MOF concentration (x_4)	9.4696	2.58
EE	Ultrasonic Power (x_1)	62.98	< 0.0001
	Ultrasonic Time (x_2)	0.2	0.6726
	Oil phase concentration (x_3)	3.01	0.1164
	MOF concentration (x_4)	3839.55	< 0.0001

4.4.1 Mutual effect of parameters

The response surface plots were used to investigate the mutual effects of ultrasonic power and MOF content on the LC and EE. The results from the BBD experiment were plotted with the ultrasonic time and oil content set at 10 min and 22.5% w/w, respectively. **Figures 4-1a and b** show the effect of the ultrasonic power ranging from 50 to 150 W, and MOF content from 1.0% to 3.0% w/w on LC and EE, respectively. LC increased continuously with the increase of ultrasonic power. However, with the MOF content increasing from 1.0% to 3.0% w/w, LC reached a maximum value of 2.0% w/w. On the other hand, the trend of MOF content and ultrasonic power to EE were both monotonicities. To sum up, it appears that increasing

ultrasonic power led to higher LC and EE, but increasing MOF content caused LC to have a peak value, and EE decreased continuously as MOF content increased.

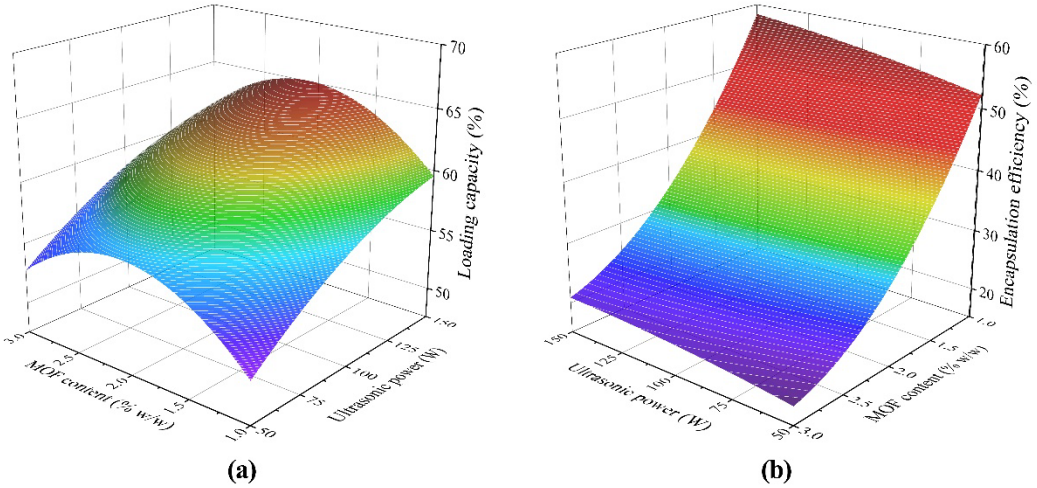


Figure 4-19Response surface plot showing the effect of ultrasonic power and MOF content on (a) LC; (b) EE.

In addition to the qualitative prediction for the four factors, the statistical analysis result can be seen in **Table 4-4**. For both LC and EE, the p values for ultrasonic power are less than 0.0001. MOF content comes in the second position, while ultrasonic time and oil content do not appear as significant. The estimated independent weight of both LC and EE models share a similar trend, except for a few minor interaction differences.

Table 4- 9Model parameters coefficients (and their associated p-value between brackets) for the prediction of the LC and EE of curcumin. Coefficients have to be used with coded levels for each factor.

Model parameters	LC		EE	
	Coefficient Estimate	p-value	Coefficient Estimate	p-value
X_1	0.0172	< 0.0001	0.1263	< 0.0001
X_2	0.2419	NS	1.5573	NS
X_3	0.2901	NS	1.5314	0.1164
X4	1.2325	0.1308*	-47.1652	< 0.0001
X_1*X_2	-0.0003	NS	-0.0002	NS
X_1*X_3	-0.0002	NS	-0.0001	NS
X_1*X_4	-0.0003	NS	-0.0168	0.1285*
X_2*X_3	-0.0051	0.0327	-0.0305	0.0443
X_2*X_4	0.0174	NS	-0.0090	NS

X_3*X_4	0.2057	0.1299*	0.2027	0.0109
X_1*X_1	-0.0006	0.0879	-0.0002	NS
X_2*X_2	-0.0062	0.0298	-0.0406	NS
X_3*X_3	-0.0062	< 0.0001	-0.0375	0.0001
X_4*X_4	-0.3910	< 0.0001	6.6207	< 0.0001

* These parameters were kept because their coefficient p-value was only slightly higher than 0.1, with non-negligible improvement of the estimated result. NS: Non-significant parameters ($p < 0.1$).

4.4.2 Optimization of synthesis conditions

For ultrasonic power factors, upsurging ultrasonic power led to a monotonous increase for both LC and EE. This result indicated that for the preparation of a Pickering emulsion by ultrasound waves, within a relatively wide range, increasing the ultrasonic power can significantly improve LC and EE of the delivery system. This phenomenon can be explained by the formation of cavitation bubbles during ultrasonic homogenization. This phenomenon led to the strong correlation between droplets particle size and ultrasonic power, and this result is consistent with previous reports(Li et al., 2017; Tikekar et al., 2013).

However, it should be noted that increasing the ultrasound power to a threshold value will cause the local temperature of the emulsion system to increase quickly during the ultrasound process, which may lead to the oxidation of natural products. We observed in a preliminary test that, at an ultrasonic power level >150 W, the system temperature will not be able to maintain during the emulsion preparation even with the ice-water bath. Therefore, we have selected 150W of power level as the upper limit for BBD modeling.

Compared to the ultrasonic power, extended ultrasonic time did not have a significant impact on LC and EE. This indicates that the Pickering emulsion has already been formed or entered a homogeneous steady state after 10 min of ultrasonic treatment. According to our previous study, the droplet size of the MOF-stabilized Pickering system was attributed to competition for MOF particles between continuous phase and droplet interface. This competition resulted in an equilibrium of MOFs' concentration in the continuous phase and at the interface of droplets. The LC and EE are related to the droplet size. After the homogenization exceeding 10

minutes, the LC and EE of the emulsion are no longer related to the ultrasonic-treat time because both the amount of MOF at interface and droplet size reaches a dynamic equilibrium.

Similar to the ultrasonic time, LC and EE appear at a peak value when the oil content reaches around 22.50% w/w (**Figure 4-2**). Unlike the previous three independent variables, the investigation of optimal conditions on MOF content is the most complicated. For LC, the optimal value of MOF content appears around 2.0% w/w. Nevertheless, for EE, as the MOF content increases within the tested range, EE decreases monotonically. It is easy to understand, by definition, LC has no direct relationship with MOF content as shown in **Equation 2-3**, but for the EE, MOF content itself is the denominator in **Equation 3-1**. Therefore, in order to eliminate interference, we used LC as the response for MOF content optimization.

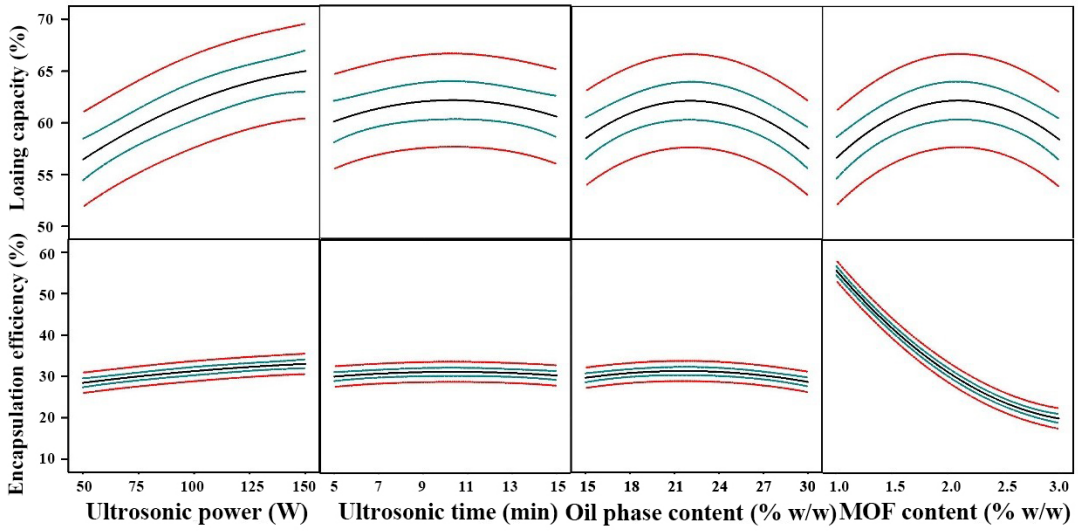


Figure 4-20Prevision profiler's outputs after maximization of the desirability function for LC and EE: Optimum emulsion preparation conditions are given while curves show how changes of factors' level affect the response. Greenline for 95% confidence interval and re

The optimum condition for preparing the MOF-Pickering emulsion system was determined by the ridge max analysis, which computed the estimated ridge of maximum response for increasing radii from the center of the original design. **Figure 4-2** showed determination. The highest values of LC (7.35±0.29%) and EE (54.34±2.45%) were predicted at

the following conditions: 150 W ultrasonic power, 11.17 min ultrasonic time, 20.0% w/w oil content, and 1.10% w/w MOF content.

4.3.3 Model validation

We used the slope of a regression line to evaluate the similarity between experimental observation and model prediction. The scatter plot of validation data is shown in Figure 3, where the x-axis indicated the values from experiments while the y-axis indicated the values from model simulation, and a slope value closer to 1 indicates a better regression. In addition, the narrower distribution of data points also means that the model is more effective. As shown in **Figure 4-3**, the data points between the actual value and estimated value of LC and EE showed a significant linear relationship without obvious outliers. Meanwhile, compared with LC, the data point distribution for EE is narrower, which means the model is more effective. This result was further confirmed with the R^2 value in **Table 4-2**.

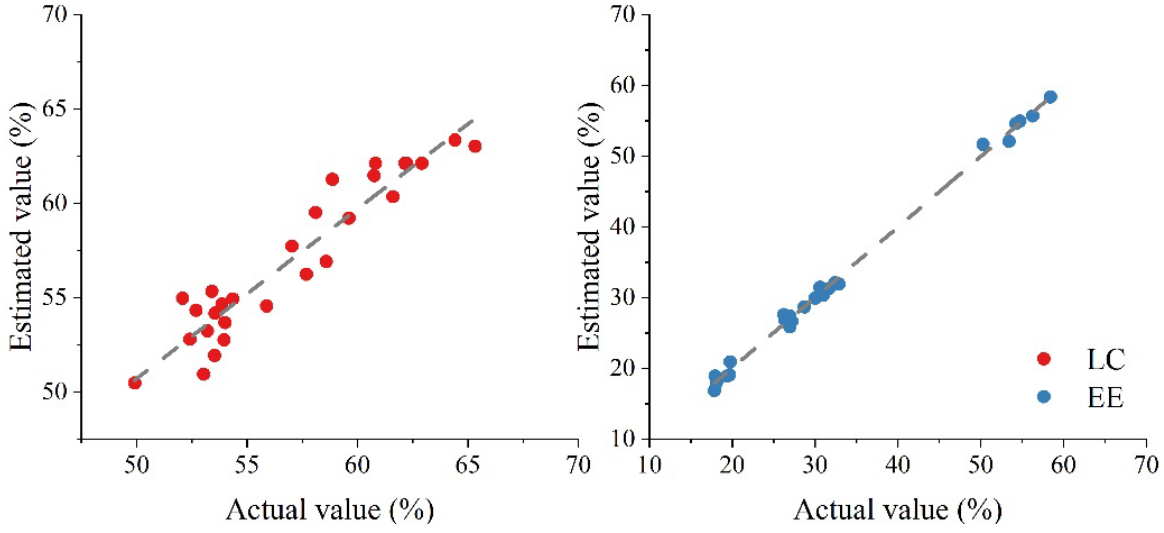


Figure 4-21Validation of the model with experimental data.

Optimum conditions are usually used to validate the model equation for the prediction of optimal responses. The validation adequacy of the predicted model (**Equation 4-3** and **Equation 4-4**) was examined by a delivery system that was prepared under the optimal condition

aforementioned. The results showed LC and EE were 7.33±0.54% and 56.18±3.03%, respectively, under the optimal conditions. This observed LC and EE did not significantly differ from the predicted LC (7.35±0.29%) and EE (54.34±2.45%). Thus, the model developed, as shown in Eq. (5) and Eq. (6) adequately predicts the LC and EE for preparing the curcumin-loaded MOF-Pickering emulsion delivery system.

4.5 Conclusion

The optimization of ultrasound in the curcumin-loaded Pickering emulsion with UiO-66-NH_2 as a stabilizer was investigated. A 3-level-4-factor BBD experiment and the RSREG procedure from SAS were employed for the experimental design and data analysis, respectively. Four parameters, i.e., ultrasonic power, ultrasonic time, oil content, and MOF content, were evaluated. According to the response surface analysis, ultrasonic power and MOF content significantly affected the LC and EE ($p<0.0001$), whereas ultrasonic time and oil content did not. The experimental data were used to establish a model for the preparation of the MOF-Pickering emulsion systems and optimal preparation parameters have been deduced from the model. The optimized conditions were found at ultrasonic power of 150 W, ultrasonic time of 11.17 min, oil content of 20.0% w/w, and MOF content of 1.10% w/w. Furthermore, a Pickering emulsion delivery system was prepared under this optimal condition, and LC and EE of 7.33±0.54% and 56.18±3.03%, respectively for curcumin were obtained, respectively. Validation test proofed the optimization parameters of this ultrasound-assisted preparation of the curcumin-loaded Pickering emulsion delivery system LC and EE matched well with the RSM prediction. Therefore, the optimization procure was considered successful. More research needs to be carried out for evaluating the toxicity of MOFs to better use in food systems. Our future study would focus on the storage stability of MOF delivery systems as well as investigation the interfacial stabilization

mechanism using porous materials as stabilizers. The newly developed delivery system in this study may find applications for the delivery of bioactive agents in functional foods and food safety areas.

Besides the Pickering emulsion system, UiO-66 NPs could also be applied in many other systems, which also need high surface area and porosity. In food scope, sensor array was a desirable platform to illustrate the potential superiorty of MOF.

Chapter 5 Development integrated portable shrimp-freshness prediction platform based on UiO-66-loaded ice-template colorimetric combinatorics

5.1 Abstract

Real-time monitoring of food freshness is critical to reducing food waste and pursuing sustainable development. Cross-reactive artificial scent screening systems provide a promising solution for freshness monitoring, but their commercialization is hindered by their low sensitivity or pattern-recognition inaccuracy. Leveraging the cutting-edge artificial intelligence and high-porosity nanomaterial, we developed a cost-effective and versatile method by incorporating metal-organic frameworks (MOFs) into smart food packaging via a colorimetric combinatorics sensor array. We screened the whole UiO-66 family by density functional theory (DFT) calculations and chose UiO-66-Br (due to the highest binding energy) to construct sensor arrays on an ice-templated chitosan substrate (i.e. ice-templated dye@UiO-66-Br/Chitosan). The physicochemical properties and morphologies of the fabricated sensor arrays were systematically characterized. The limit of detection (LOD) of 37.17, 25.90, and 40.65 ppm for ammonia (i.e. ammonia (NH_3), methylamine (MA), and trimethylamine (TMA), respectively) was achieved by the prepared composite film. Deep convolutional neural networks (DCNN), a deep learning algorithm family, were further applied to monitor shrimp freshness by recognizing the scent fingerprint. Four state-of-art DCNN models were trained using 31584 labeled images and 13537 images for testing. The highest accuracy achieved was up to 99.94% by the Wide-Slice Residual Network 50 (WISeR50). Our newly developed platform is integrated, sensitive, and non-destructive, enabling consumers to monitor shrimp freshness in real-time conveniently.

5.2 Introduction

According to a recent report from the United States Department of Agriculture (USDA) in 2018, approximately 15% of perishable food is wasted at retail stores due to damage and spoilage, equaling $162 billion annually in the U.S[1]. Particularly, seafood has the highest percentage of waste compared to other food categories, with about 30% of the seafood products being wasted. Typically, more than half of the seafood waste or over 94 million pounds per year occurs at the end of the value chain, largely due to the conservative allocation of expiration dates on "sell by" tags(Van der Werf & Gilliland, 2017; White, Froehlich, Gephart, Cottrell, Branch, & Baum, 2020). In stark contrast to the arbitrary allocation of expiration dates, real-time measurements on individual products are predicted to effectively reduce the waste by 60%, which is worth 135 million dollars per year in the U.S(Corradini, 2018).

As evident, there is tremendous market value for developing real-time food freshness monitoring devices(Xiao-wei et al., 2018). Recently, different approaches mimicking the mammalian olfactory system have been developed for the detection of explosives, drugs, and deleterious chemicals in foods(Guo et al., 2020; Schroeder et al., 2019; Yang et al., 2021). One mainstream approach is artificial scent screening which requires two critical components: cross-reactive sensing and fingerprint pattern recognition(T. Wang, Wang, Yang, Li, Loh, & Chen, 2020). Conventionally, cross-reactive sensing is achieved by integrating metal oxides(J. Chen et al., 2018) or colorimetric dyes onto sensor arrays(Dai et al., 2020). While those sensors could target different molecules to generate a fingerprint pattern, they suffer from low adsorption rates and poor selectivity for volatile aroma compounds (VAC), resulting in poor accuracy and sensitivity(Xiao-wei et al., 2018). In addition, the high complexity of the image-based pattern recognition cannot be efficiently analyzed by traditional statistical methods, e.g. discriminant

analysis (LDA), principal component analysis (PCA), and hierarchical cluster analysis (HCA)(W. Hu et al., 2019).

To address these challenges, we synergized artificial intelligence (AI), i.e. deep learning and porous framework nanomaterials in colorimetric sensor array systems. We adopted the metal-organic frameworks (MOFs) to enhance sensitivity - due to the high-porosity structure with extremely high surface to bulk ratio, they have been widely applied in gas separation and storage, catalysis, biomolecule encapsulation, and battery(Anik, Timur, & Dursun, 2019)-(Ajdari et al., 2020). Besides, the addition of non-coordinated heteroatoms to the framework ligand can improve the interior surface contact of host frameworks with certain guest analytes, resulting in changes in photo-, electrochemical, and other characteristics. In addition, MOF nanoparticle would increase the dispersibility of small molecules due to their high surface area decreasing the binding energy of the system. And lowering energy would favor the adsorption of ammonia gas thermodynamically. Among different MOFs, we chose UiO-66 (named from the University of Oslo) for its high thermal, water, chemical, and mechanical stability, all of which arise from the high coordination number, strong bonds between inorganic blocks, and the linker, and strong Zr-O bonds(Giannakoudakis et al., 2019). Furthermore, functional groups (such as $-NO_2$, $-NH_2$, -OH, $(COOH)_2$, $-(CH_3)_2$, and –Br) can be introduced into UiO-66 to increase the gas detection sensitivity and selectivity(Demir, Walton, & Sholl, 2017). To address the long-standing challenge in accurate image recognition, we exploited the latest advances in AI and deep learning(Ordovas, Ferguson, Tai, & Mathers, 2018). In particular, we employed a deep convolutional neural network (DCNN) and its derivative algorithms, which have found widespread success in the food field for dietary monitoring(Ege et al., 2018), food quality detection(X. Yu et al., 2019), food supply chain credit evaluation(Mao, Wang, Hao, & Li, 2018),

and predicting morbidity of gastrointestinal infections by food contamination(Bisgin et al., 2018).

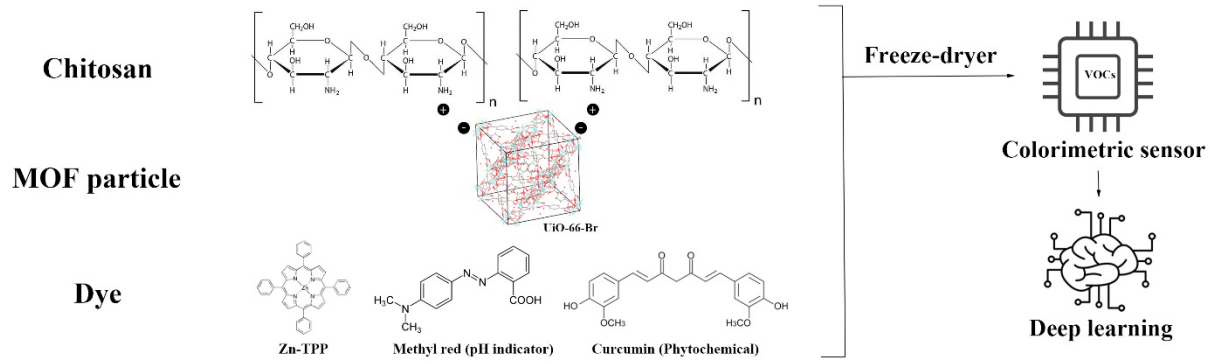


Figure 5-22Fabrication of ice-template colorimetric sensor array with DCNN.

In this study, as shown in **Figure 5-1,** an ecofriendly sensor system was developed on ice-templated dye-loaded monoliths formed with chitosan, a low-cost biodegradable material, and UiO-66 (Dye@chitosan/UiO-66 hereafter). The system was designed and optimized with the help of the high-performance computer (HPC) by DFT and Grand Canonical Monte Carlo (GCMC) simulation. The adsorption ability of the sensor system was then evaluated for selective VACs. Finally, a fully supervised DCNN was trained using 31,584 labeled shrimp images with the sensor array. The overall objective of this study is to establish a MOF-based practical platform for real-time monitoring of seafood freshness based on advanced computer technology to effectively reduce food waste.

5.3 Materials & Methods

5.3.1 Materials

Zirconium tetrachloride (99.5 %), benzene-1,4-dicarboxylic acid (BDC, 98.0%), 2- 2-bromoterephthalic acid (Br-BDC, 98.0%), N,N-dimethylformamide (DMF, 99.0%), nile red, chitosan (medium molecular weight), ammonia hydrogen solution (25% in water), methylamine

solution (33% in absolute ethanol), trimethylamine solution (45% in water), acetic acid (HAc, 99.9%), boric acid, (99.8%), 2-methoxyethanol (99%) and 7 dyes were purchased from Sigma-Aldrich (St. Louis, MO, USA, detail of dyes were presented in **Table 5-1**). All chemicals are in analytical grade. Jumbo tiger prawns (*Penaeus monodon*) at a mass of 14 to 16 g per shrimp were bought from Maine Ave Fish Market (Washington DC, USA). The microwave container (38 oz) was bought from a local market (SafePro, MD, USA).

Table 5-1 0 The list of biocompatible chromophore dyes on the colorimetric sensor array.

No	Name	Abbreviation	Color range
1	Methyl Red	MR	4.4 (Red)- 6.2 (Yellow)
2	Zinc Tetraphenylporphyrin	TPP	Amino gas
3	Curcumin	CUR	7.8 (Yellow)- 9.2 (Reddish Brown)
4	Chlorophenol Red	CPR	4.8 (Yellow) - 6.8 (Red)
5	Bromocresol Purple	BCP	5.2 (yellow) - 6.8 (Purple)
6	Bromocresol Green	BCG	3.8 (Yellow) - 5.4 (Blue)
7	Bromophenol Blue	BPB	3.0 (Yellow) – 4.6 (Blue)

5.3.2 Computational methods

Electronic structure calculations were performed using supercells to study the effect of confinement on molecular adsorption. The parent UiO-66 structure was taken from Jasuja et al[21]. and hydrogen(s) were replaced in the benzene ring with the functional groups of interest(Jasuja & Walton, 2013). These calculations used 1x1x1 supercell with lattice parameters of ~14-15 Å in each direction. The Vienna Ab-initio Simulation Package (VASP) was used at the PBE-D293 level with a 400 eV kinetic energy cutoff and one Γ-centered k-point. For structural optimization, the total energy and ionic force convergence criteria were $1x10^{-4}$ eV and $3x10^{-2}$ eV/Å, respectively. UiO-66 has a 3D cubic framework composed of $Zr_6O_4(OH)_4$ nodes linked with 1,4-benzenedicarboxylate linkers (BDC). It has centric octahedral cages (11 Å) connected to eight tetrahedral cages (8 Å) with triangular windows (6 Å).

Binding energies were defined in **Equation 5 1**:

Equation 5-11

$$E_{binding} = E_{adsorption\ complex} - E_{adsorbate} - E_{adsorbent}$$

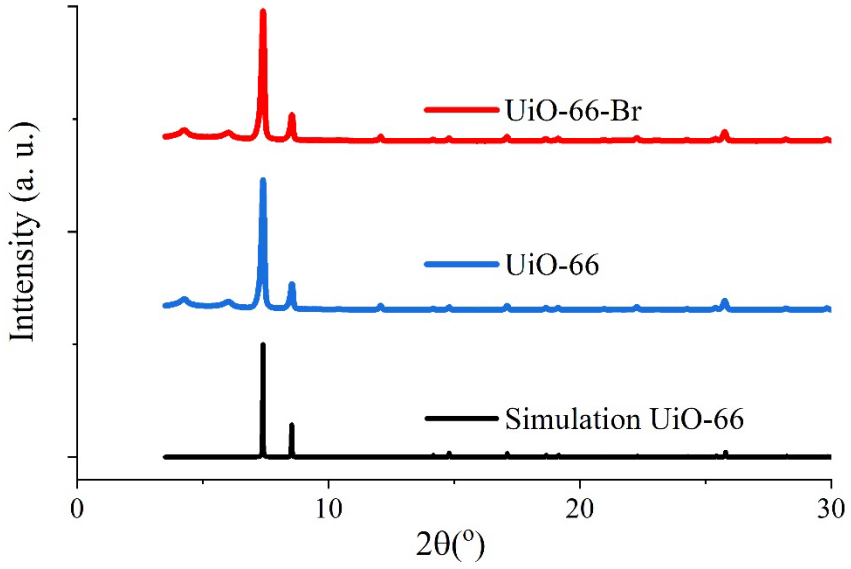
where $E_{binding}$, $E_{adsorption\ complex}$, $E_{adsorbate}$ and $E_{adsorbent}$ were binding energy, total energy of adsorption complex, the total energy of isolated adsorbate, and total energy of isolated adsorbent, respectively. The most stable state between molecules is often the state with the lowest binding energy, so we used binding energy to predict molecular adsorption.

GCMC simulations were used to calculate different isotherms at 200 K for UiO-66 and UiO-66-Br. At each pressure, the parameter of the equilibration step at 10,000,000 was set as a computer ensemble average. The framework atom was taken from the Universal Force Field (UFF). A charge of -0.482 was placed on the N nuclei and +0.964 at the center of mass. Ewald & Group summation method was used for all interactions with atom-based van der Walls. All calculations mentioned above were based on a sorption isotherm module in Materials Studio (BIOVIA, v 5.51). The parameters mentioned above were taken from a previous study with some modifications(Bernini et al., 2014).

5.3.3 Preparation of UiO-66 and UiO-66-Br

The UiO-66-Br was synthesized by a solvothermal method according to a previous report with minor modification(D. Ma, Han, Gao, & Chen, 2019). First, $ZrCl_4$ (1.17 g, 5 mmol) and Br-BDC (1.23 g, 5 mmol) or benzene-1,4-dicarboxylic acid (0.83 g, 5 mmol), and acetic acid 1.0 mL were dissolved in DMF (30 mL) at room temperature. Then, the mixture was placed in a Teflon-lined stainless-steel autoclave after adding 2 ml of de-ionized water and mixing completely. The autoclave was placed in an oil bath at 121 ºC for 24 hours. Afterward, the solution was cooled to room temperature for 30 mins, and the resulting UiO-66 and UiO-66-Br particles were separated

via centrifugation (12,096 × g, 10 min) at room temperature and washed three times with ethanol. The resulting white powder was dried in an oven at 40°C for 4 hours and tested by XRD and SEM for verification (**Figure 5-1**).



(a)

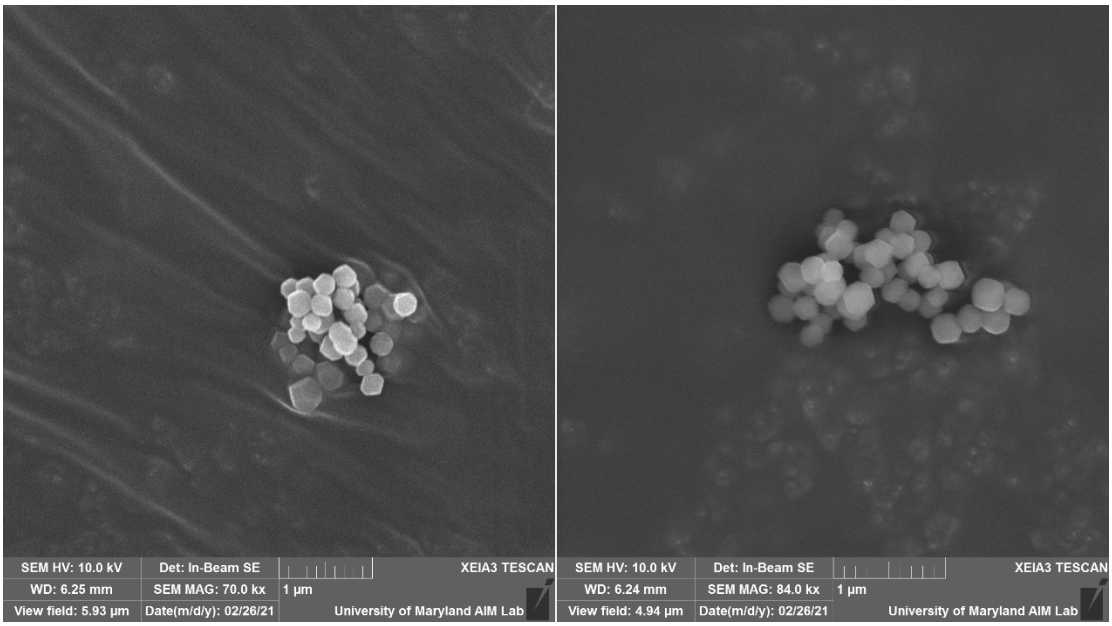


Figure 5-23(a) Powder X-ray diffraction (PXRD) patterns of synthesized UiO-66 and UiO-66-Br compared with the simulated one for UiO-66; (b) SEM images of UiO-66 nanoparticles; (c) SEM images of UiO-66-Br nanoparticles

5.3.4 Ice-templated Dye@chitosan/UiO-66 monoliths

In detail, 2.5 mL chitosan solution (5 mg/mL, 2% HAc), 2.5mL UiO-66 / UiO-66-Br solution (5 mg/mL, 2% HAc), and 0.4 mL dye solution (5 mg/mL in 2-methoxyethanol) were added in a bottle. The formulas for all dyes were enclosed in **Table 5-1**. After vigorous stirring, 0.2 mL of each solution was transferred to its assigned well on a 96-well plate, diameter 6 mm for each pore. After carefully sealing the plate with a cap, the plate containing the solution was slowly immersed into a bath of liquid nitrogen for 5 min. The frozen sample was freeze-dried for approximately 48 hours to form dry chitosan/UiO-66 monoliths. The monoliths of two types of UiO-66 particles were denoted as Chitosan/UiO-66 and Chitosan/UiO-66-Br. For control, 2.5 wt% chitosan solution without UiO-66 or Uio-66-Br was freeze-dried following the same procedure, and the acquired monolith was denoted as Chitosan. All monoliths with different dyes adhered on a paper tape in the order of color in **Table 5-1** to form the sensor array.

5.3.5 Calculation of amine gas concentration.

Detection experiments on amine gases were performed in standard Petri dishes (100 * 15 mm) with temperature-controlled at 20°C. The colorimetric sensor array was passed on the cap of the Petri dishes. The required gas concentration was reached by injecting a certain volume of liquid analyte into the dish and sealing with parafilm (i.e. ammonia (NH_3), methylamine (MA), and trimethylamine (TMA)). The resulting gas concentration (C_{ppm}) was calculated using the following equation **Equation 5 2**:

Equation 5-12

$$C_{ppm} = \frac{V_{\mu L} \times D_{mg/L} \times W}{M_{g/mol} \times V_L} \times 22.4 \times 10^7$$

Where $V_{\mu L}$ is liquid analyte volume, $D_{mg/L}$ is the liquid density, W is the mass fraction of the liquid, $M_{g/mol}$ is the molecular weight of the liquid analyte, V_L is the volume of Petri dishes.

5.3.6 Material characterization

Fourier transform infrared (FT-IR) spectrometry

The samples (ice-template UiO-66/chitosan and UiO-66-Br/Chitosan, 3-5 mg) were mounted onto a Jasco FT-IR 4100 spectrometer (Jasco Inc., Easton, MD, USA) coupled with an attenuated total reflectance accessory (ATR). The infrared transmittance was acquired at the wavenumbers from 600 to 4000 cm^{-1} with a resolution of 2 cm^{-1}. Sixty-four repeated scans were undertaken for each sample. The spectra were averaged, smoothed, corrected for their baselines, and converted to absorbance with Spectra Manager software (Jasco Inc., Easton, MD, USA)(Mei et al., 2017).

Morphology analysis

Samples were scooped into a 10 mm cup and placed into a shuttle, which was frozen conductively, in a Styrofoam box, by placing the brass plates on the surface of a pre-cooled (-196°C) brass bar whose lower half was submerged in the liquid nitrogen. After 20-30 s, the shuttle containing the frozen sample was transferred to a Quorum PP2000 cryo-preparation chamber (Quorum Technologies, East Sussex, UK). The top layer of the frozen sample was cryo-fractured using a metal blade mounted inside the preparation chamber. All specimens were etched inside the cryo-preparation system to remove any surface contamination (condensed water vapor) by raising the temperature of the stage to -90°C for 10-15 mins. Following the etching, the temperature inside the chamber was lowered below -130 °C, and the specimens were coated with a 10 nm layer of platinum using a magnetron sputter head equipped with a platinum target inside the cryo-preparation chamber. The specimens were transferred to a pre-cooled (-130°C) cryo-stage in the scanning electron microscope (SEM) **(**Tescan XEIA FEG SEM, Brno, Czechia) for observation. An accelerating voltage of 5 kV was used to view the specimens. Images were captured using a 4pi Analysis System (Durham, NC).

Total volatile basic nitrogen (TVB-N) measurement

To mimic the storage conditions at supermarkets, 150 ± 10 g of fresh shrimps, without any pretreatment was placed in a plastic box. One sensor array per package was attached to the inner side of the bag. Shrimps were stored at 4 ^{o}C before analysis.

To test the freshness of shrimps without the interference of image collection, a separate group of 24 (8 storage intervals x 3 parallel experiments) packages of shrimps was prepared for TVB-N testing. Ten grams of minced shrimp sample with shell were homogenized with 100 mL of distilled water (Ultra-Turrax T25, IKA, Staufen, Germany). The mixture was filtered for 30 mins later to obtain a liquid sample. Then, 3 mL boric acid absorbing solution (20 g/L) and 50 μL pH

indicator (methyl red: bromocresol green = 1:5, v/v) were added to the inner chamber of Conway dish (diameter 90 mm). In the outer chamber, 3 mL potassium carbonate saturated solution and 1 mL sample liquid were added in sequence. The Conway dish was kept sealed and incubated at 37℃ for 2 hours. The volatile amine gases were absorbed by boric acid as an absorbing solution. The abovementioned mixture was then titrated using 0.1 mol/L hydrochloric acid (HCl), and the amount of volatile amines was calculated with the following **Equation 5-3**.

Equation 5-13

$$\boldsymbol{X = \frac{(v1-v2)\times C\times 14}{m\times 0.05}\times 100} \qquad (3)$$

Where, X is TVB-N content in the sample (mg/100g);

*v*1 is the volume of 0.1 mol/L HCl used for the actual test (mL);

*v*2 is the volume of 0.1 mol/L HCl used for the control test (mL);

C is the HCl concentration (mol/L);

14 is the weight of nitrogen;

m is the weight of the sample (g).

5.3.7 Machine learning

Circular region of interest (ROI) identification

Hough circle transform was applied to recognize the color area of the sensor array. The circled candidates were produced by "voting" in the Hough parameter space and then selecting glocal maxima in an accumulator matrix. To obtain the best result, the inverse ratio of the resolution was set to 1, the upper threshold for the internal Canny edge detector was set to 10, the threshold for center detection was set to 9, and the range of radius to be detected was [20,60) pixel. The ROI was extracted from the seven dye region labeled by the Hough circle transform(Kuo et al., 2019).

Database preparation and images collecting for DCNN training

To collect data from the sensor, 10 s of a short video for each box was taken with shrimps at a certain storage interval. During the 10 s, the color and intensity of the background light in the photo box changed according to the program settings. Eight intervals that covered the spoilage process were selected. During the data collecting period, a portion of shrimp was examined for TVB-N, and others were used for image acquisition. Noted that, we changed the light that was included in the input images and photoed them by iPhone 11 Max Pro for training to fully mimic real testing scenarios. The 60 fps video was then randomly sampled at 30 fps and exported as an image set. Based on the actual measured TVB-N results and shrimp freshness criteria, we labeled samples with <30 mg N/100 g as fresh and >30 mg N/100 g as spoiled. And the final database was split into a training set and a testing set at ratio 7:3. The final training set contained 31,584 labeled images and the test set contained 13,537 images. The fresh to spoiled ratio was 1:1 in both the training set and test set.

Network architecture

With the acquired database, DCNN was employed to train a food classification system. This system took images as input and classified them into two categories, i.e., Fresh and Spoiled. Four different DCNN architectures were compared for their effectiveness in classifying our novel food dataset: VGG(Simonyan & Zisserman, 2014), ResNet-50(K. He, Zhang, Ren, & Sun, 2016b), Wide ResNet-50(Zagoruyko & Komodakis, 2016), and Inception V3(Szegedy et al., 2015). These four CNN architectures were pre-trained by the most commonly-used and challenging image classification dataset. All experiments in this study were conducted on Windows Servers with Nvidia Quadro RTX 3000 GPUs. During the training and testing, the images were resized to 224 * 224 as inputs. The learning rate was set to 0.1 at the beginning of training and reduced

to 0.05 and 0.01 when the test accuracy exceeded 70% and 80%, respectively. The momentum and weight decay were set to 0.9 and 0.0001, respectively.

5.4 Results and discussion

5.4.1 Identification of materials for selective adsorption

During the storage, proteins in rotting shrimps are microbially decomposed into peptides and amino acids(X. Yu et al., 2019). Over time, these components are further degraded into amines and ammonia, which will cause the color change of the sensor array(Xiao-wei et al., 2018; Yang et al., 2021). Four amine gases (i.e. NH_3, MA, TMA and PUT) typically generated during shrimp storage were simulated.

Previous research found that UiO-66-$(COOH)_2$ had a high CO_2 working capacity(Z. Hu, Peng, Kang, Qian, & Zhao, 2015), UiO-66-NH_2 was identified as the most promising material for vacuum swing adsorption(Cmarik, Kim, Cohen, & Walton, 2012), and UiO-66-$(CH_3)_2$ diminished water adsorption by ~50% comparing with bare UiO-66(Jasuja et al., 2013). However, due to the abundance of benzene ring modifications, the selection of the appropriate functionalized materials for particular applications from overwhelming functional groups motivated the utilization of the computer method. Indeed, quantum chemistry calculations, especially density functional theory (DFT), were performed using clusters chosen to examine a wide range of functional groups for selective adsorption of ammonia(D. Yu, Ghosh, & Snurr, 2012). Although methods to develop accurate force fields for molecular adsorption in MOFs from electronic structure calculations have developed rapidly in recent years, they still require extensive calculations for each specific adsorbent of interest. Here, we focus on using results from electronic structure calculations and identify the best choice of functional UiO-66 for selective VACs adsorption.

The binding energies for the aforementioned four amine gases were calculated for the [-NH_3^+, -OH, -Cl, -NO_2, -NH_2 -Br] functionalized and unfunctionalized UiO-66 MOFs using DFT with PBE-D2 functions. **Figure 5-3a** compared the binding energy for four amine gases in functionalized UiO-66 materials. The PBE-D2 calculation is a useful quantification to consider situations with a low bulk phase concentration of adsorbing species(Demir et al., 2017). Since our calculations have focused on individual binding sites for adsorbed molecules and the concentration of absorbed molecules was low in the food package, PBE-D2 was selected. It should be noted that this heuristic approach neglects possible synergistic effects between co-adsorbed species. The combination color close to red in the figure represents the strongest preferential binding energy. Among selected groups, -Br functionalized UiO-66 MOFs showed the strongest preferential affinity for Four types of amine gases (i.e. NH_3, MA, and TMA), whereas unfunctionalized UiO-66 showed the least. For example, UiO-66-Br binds MA (84.14 kJ/mol) more strongly than UiO-66-OH (77.42 kJ/mol) and the lowest bare UiO-66 (38.4 kJ/mol). Although calculated binding energies and experimental heat of adsorption are not precisely the same, they can be used to qualitatively screen and rank the binding affinity for the UiO-66 family.

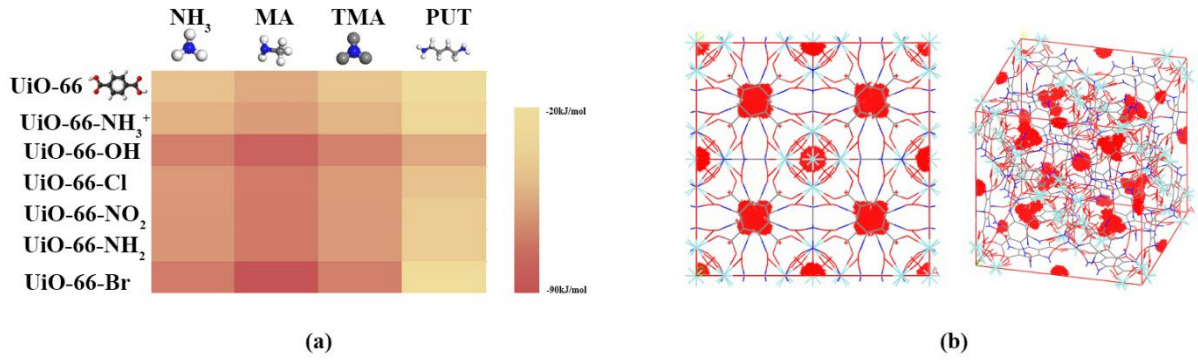


Figure 5-24(a) the heat map of relative binding energy for four selected amine gases in functionalized UiO-66 materials determined from periodic PBE-D2 calculations; (b) Material Studio simulation indicates the center of mass (COM) probability distribution of the a

Figure 5-3b illustrates the structure of UiO-66-Br with absorbed NH_3 molecules. The distribution of red dots represents the center of mass (COM), which indicates that amino gas molecules are more preferentially being adsorbed onto the BDC ligand sites than Lewis acid sites of Zr_6 nodes. According to the GCMC simulation result, the BDC ligand with the functionalized group was identified as the preferential adsorption site for amino gas. Besides, the adsorption enthalpy $-\Delta H^o$ (i.e. isosteric heat) of water molecules on UiO-66-Br is calculated as 11.7 kJ/mol, which is much smaller than 84.14 kJ/mol for MA molecules and 67.4 kJ/mol for NH_3. From the thermodynamic aspect, amino gas molecules can replace the pre-adsorbed water molecules on UiO-66-Br material(K. C. Kim, Yu, & Snurr, 2013). Hence, the moisture in the real atmosphere has a negligible impact on VAC sensing. Based on the results of the above simulations, UiO-66-Br was selected as the candidate material for colorimetric sensor array preparation. Besides, to verify the simulation results, unfunctionalized UiO-66 was included as a control for the following experiments.

5.4.2 Sensor array validation on response to VAC standards

Because the sensor array was prepared on a paper base, it is cheap and can be integrated easily with existing package materials. To assess the ability of the colorimetric sensor array to be used

as an indicator for VAC, the response of the Dye@UiO-66-Br/Chitosan sensor array to multiple gases, i.e. NH_3, MA, and TMA, was tested. The color changes of the array are dependent upon the concentration of selected gases, which provides a direct method for quantitative analysis(Guo et al., 2020). **Figure 5-4a** shows the color changes of Dye@UiO-66-Br/Chitosan sensor arrays, which were treated with different concentrations of NH_3, MA, and TMA (photo by iPhone 11 Pro Max). All sensor arrays showed different color changes with these gases at concentrations ranging from 0-320 ppm. Similar to mammalian olfactory receptors, where one scent molecule can bind to different receptors and one type of gas can trigger several sensors' color changes within the array. Meanwhile, the sensor array that responded to each gas formed a colorful fingerprint.

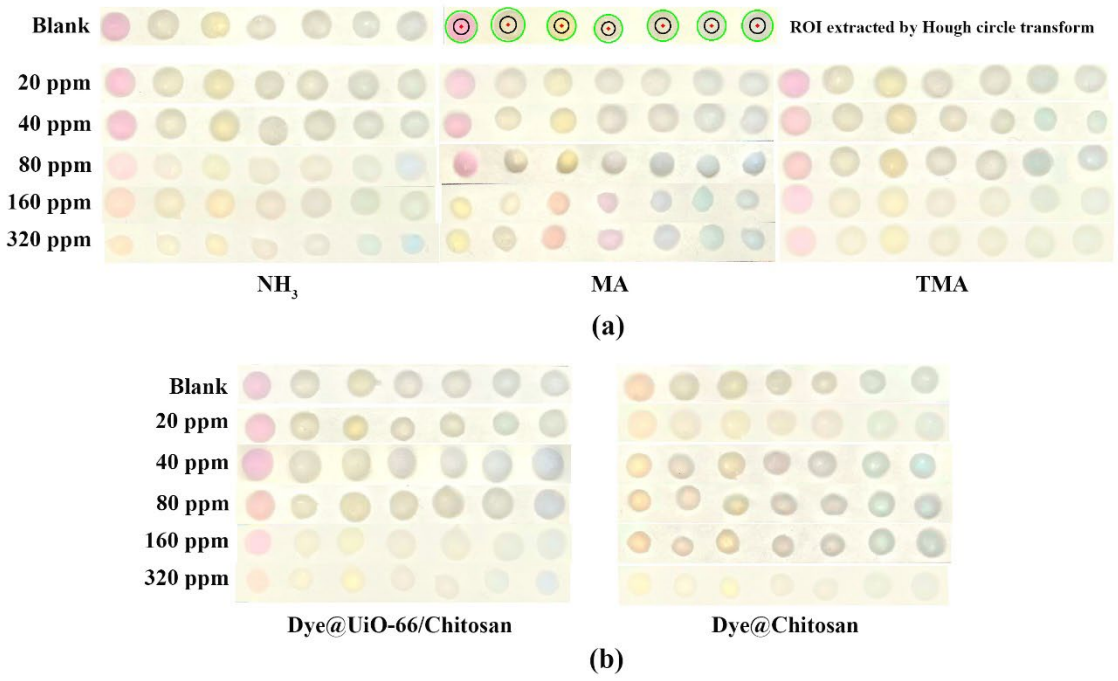


Figure 5-25(a) Photoed images of color changes of Dye@UiO-66-Br/Chitosan sensor arrays exposed to NH3, MA, and TMA as gas concentration increased from 20 to 320 ppm; (b) Photoed images of color changes of Dye@UiO-66/Chitosan and Dye@Chitosan sensor arrays exposed t

To describe the color distribution of the sensor, a color extraction and area recognition system based on the Hough circle transform was applied. The circled candidates are produced by "voting" in the Hough parameter space and then selecting glocal maxima in an accumulator matrix. The ROI was extracted from the seven dye region labeled by the Hough circle transform (see in **Figure 5-4a**). Then 100 pixels were randomly generated from ROI, and each variance of color components (red, green, and blue, RGB) of pixel was computed. According to previous reports, the variance is an important descriptor of the distribution of values, lower values refer to a more even dye distribution and vice versa(Xiao-wei et al., 2016). To achieve the quantitative analysis of color changes, the Euclidean distance (ED), an important value for the evaluation of color, was calculated by the RGB distance between selected concentrations with blank(Schroeder et al., 2019). As shown in **Figure 5-5**, ED values were overlapped under 40 ppm for seven dyes. As gas concentration increased, some dyes such as MR showed increased ED, whereas others still showed insignificant changes (e.g. CPR, $n = 10$, $p < 0.05$). Meanwhile, ED values of the sensor array quantitatively followed the trends of the gas concentration. Corresponding to the previous report, higher concentrations of three types of amine gases (i.e. NH_3, MA, and TMA) displayed higher ED values but still some combinations did not show significant change (e.g. MA/BPB and NH_2/CPR)(Guo et al., 2020; Schroeder et al., 2019; Yang et al., 2021).

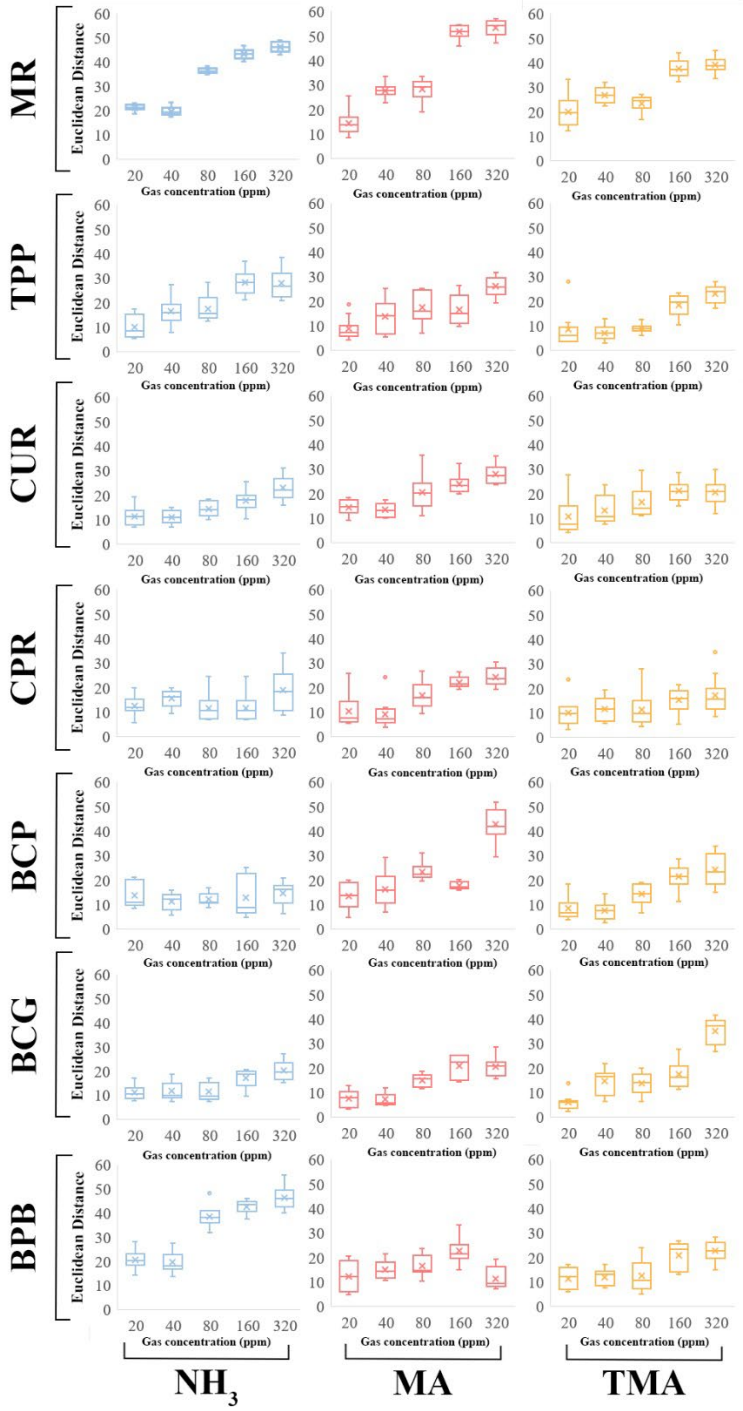


Figure 5-26Boxplot of the ED distribution of different dyes based on UiO-66-Br/Chitosan for NH3, MA, TMA at different gas concentrations (from 20 to 320 ppm, n = 10).

The limits of detection (LODs) of three amine gases is obtained at the signal to noise ratio of 3 following equation **Equation 5-4** and **Equation 5-5**:

Equation 5-14

$$S = \sum_{i=0}^{20}(|R_{Analyte} - R_{Control}| + |R_{Analyte} - R_{Control}| + |R_{Analyte} - R_{Control}|)$$

Equation 5-15

$$N = \sqrt{\frac{\sum_{i=0}^{20}((R_{Control}-\bar{R})^2+(G_{Control}-\bar{G})^2+(B_{Control}-\bar{B})^2)}{n-1}}$$

where S is defined as the difference between blank control (Control) and exposed groups (Analyte) and n represents ten independent experiments. The estimated LOD for NH_3, MA, and TMA was 37.17, 25.90, and 40.65 ppm, respectively. This result demonstrated our sensor array had an adequate LOD (less than 35 ppm) for shrimp freshness detection in the food package. In addition, the ED values for each sensor before and after exposure to the same amount of gas were different. For example, after exposure to 320 ppm NH_3, MA, and TMA, the ED values for the MR sensor were 46.26, 53.13, and 39.13, respectively. This can be explained by the VASP simulation that the number of methyl groups in these three amine gases would impact the binding energy of the adsorption complex. Different chemical environments and the number of amino (-NH_2) groups in these selected amine gases would induce different color combinations in the sensor array. Meanwhile, this result was consistent with the observation from naked eyes. Different chemical environments and the number of -NH_2 groups in these selected amine gases would induce different color combinations in the sensor array. Meanwhile, this result was consistent with the observation by naked eyes. To further verify the computer simulation results, UiO-66/Chitosan and chitosan monolithic colorimetric sensor arrays (i.e. Dye@UiO-66/Chitosan and Dye@Chitosan) were prepared for comparison. As shown in **Figure 5-4b**, two clear trends in color differences can be observed. First, all sensor arrays were affected by individual ammonia gas concentrations. Second, when observed by the naked eye, the colors of UiO-66-Br/Chitosan (see in **Figure 5-4a,** NH_3) and UiO-66/Chitosan were different from the Chitosan array.

Meanwhile, adding UiO-66 or UiO-66-Br MOF particles led to the increasing turbidity of the system before freeze-drying in preliminary research and also showed the overall color change of the sensor array. Moreover, to all sensor arrays, the dyes spread uniformly and distributed evenly. To quantitatively analyze the results, two traditional machine learning models (i.e. PCA and HCA) were used.

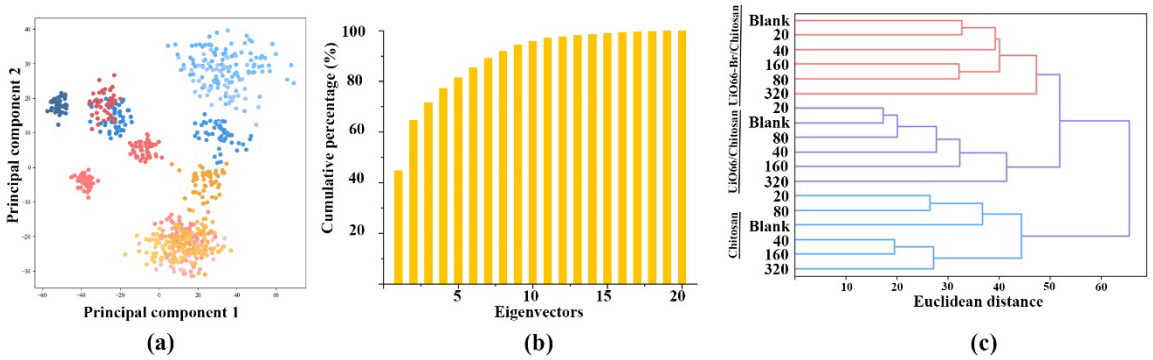


Figure 5-27(a) Clusters of three sensor array systems: Dye@UiO-66-Br/Chitosan (red), Dye@UiO-66/Chitosan (blue), Dye@chitosan (yellow) via 2D PCA score plot. The color shade of the dot represents the concentration of ammonia gas concentration. The two dimensions plotted only encompass 44.73% of the total variance; (b) PCA score plot, the number of eigenvectors (i.e. principal components) need to reach cumulative percentage (i.e. total variance); (c) Cluster tree produced by hierarchical cluster analysis showed three colorimetric sensor array systems can be distinguished treated by different ammonia gas concentration.

PCA is a widely used classification method(Granato, Santos, Escher, Ferreira, & Maggio, 2018). Being evaluated by PCA, a 360×21 (20 duplicates × 6 gas concentration × 3 sensors arrays ×21 RGB values) dimensional matrix was acquired from the colorimetric sensor array. The PCA clustering result was shown in **Figure 5-6a**. PCA created several independent principal components (PCs) that maximally represent the whole matrix. According to the PCA score plot (**Figure 5-6b**), 5 PCs were needed to reach 80% of the total variance, and 8 PCs were needed to reach 90% of the total variance. Here, due to the difficulties of drawing a high dimensional plot, PCA clustering with two PCs (2D PCA score) was plotted, which represented 44.73% of the total variance. Two clear points can be concluded. First, UiO-66-Br/Chitosan sensor array (red dots in **Figure 5-6a**) showed four cluster groups in the plot, three high gas concentration groups

were clearly distinguished between each other. For UiO-66/Chitosan sensor array (blue dots), only two high gases concentration groups could be successfully separated, and only one group could be roughly classified for the chitosan sensor array (without UiO-66 particle, yellow dots). This could be explained by the VASP simulation results that different binding energy would induce different color combinations in the sensor array, which verified the hypothesis that UiO-66-Br/Chitosan sensor array showed the best sensitivity. Besides, as the gas concentration increased, sensor arrays with different initial colors moved toward the same endpoint region **(**upper left area in **Figure 5-6a**). The possible reason was that the direction of dye color change was the same in different sensors, so the color change endpoints were similar. Also, the PCA score showed that below 10 PCs, the variance increased with PCs and reached a platform after 15 PCs. This result could be explained by the over-adequate number of dyes. For the ammonia gas response, the combination of multiple sensors improves the accuracy of the analysis, but there are some sensors in the array not involved. With HCA, Ward's minimum variance method was applied to determine gas-induced variations of the 21-dimensional RGB colorimetric sensor array (**Figure 5-5c**). The cluster tree showed the three sensor arrays were clearly separated from each other. In addition, UiO-66-Br/Chitosan showed the highest ED value among different gas concentration groups. The results from PCA and HCA clustering intuitively revealed that UiO-66-Br/Chitosan sensor array effectively discriminated NH_3 based on a cross-reactive colorimetric mechanism. Meanwhile, HCA results further confirmed that UiO-66-Br/Chitosan showed a better sensitivity when compared to the other two sensor arrays. Together, these results demonstrate that it is highly possible to use our colorimetric barcode to monitor shrimp freshness and other microbial metabolic processes in food storage.

Another comparison of the results between three types of colorimetric sensor arrays was shown in **Table 5-2**. To study the stability of sensor arrays, the variation in the color shade was evaluated. At each concentration of NH_3, colorimetric sensor arrays were repeated ten times and the color standard deviation after exposure to 40 ppm NH_3 was compared. A lower standard deviation indicates a more precise measurement and better stability. The result was consistent with the computer simulation analysis that UiO-66-Br/Chitosan system showed the best accuracy when compared to bared UiO-66 and chitosan monoliths. Besides, the UiO-66-Br/Chitosan system showed the shortest equilibrium time, which could also be explained by the lower bonding energy simulated by VASP.

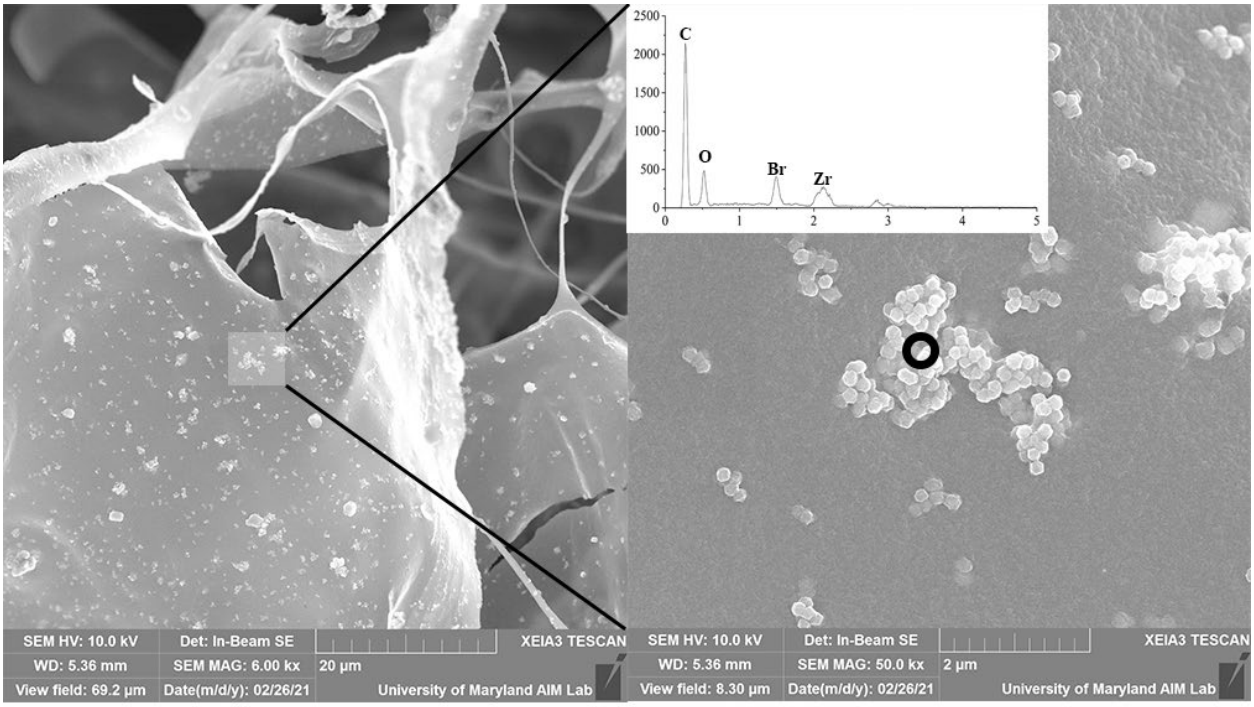
Table 5-1 The comparison of the range of concentration and equilibrium time between the three kinds of colorimetric sensor arrays.

Sensor array	Range of concentration (ppm)	Equilibrium time (s)	Standard deviation		
			Red	Green	Blue
UiO-66-Br/Chitosan	80~	420	0.09	0.04	0.10
UiO-66/Chitosan	160~	550	0.16	0.10	0.18
Chitosan	320~	720	0.18	0.13	0.22

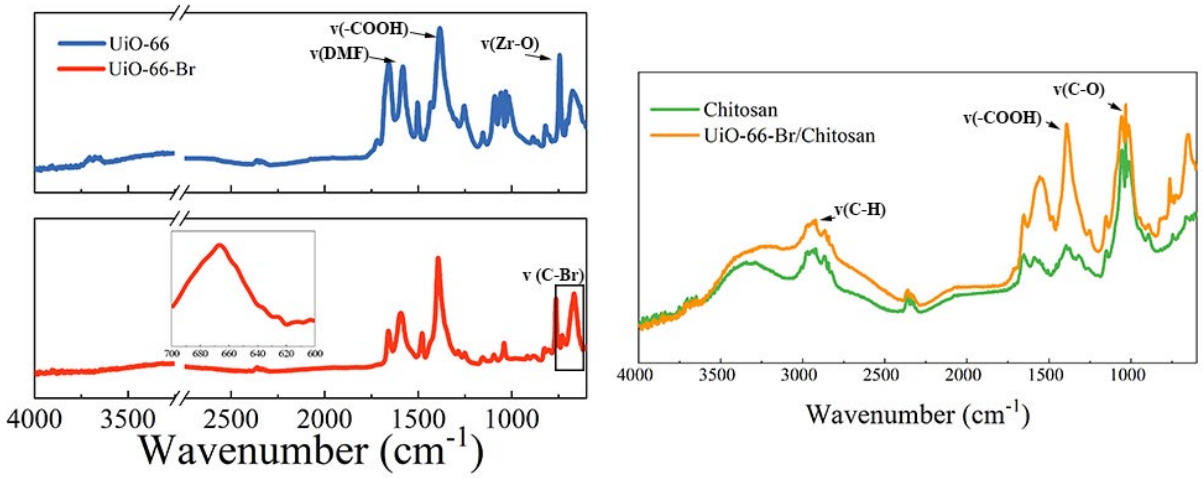
5.4.3 Characterization of sensor arrays

The UiO-66-Br/Chitosan system has fine fibers and sheets' structure with voids (**Figure 5-7a**). SEM images revealed that MOF particles were trapped in the chitosan network after freeze-drying. The interspersed voids in the interwoven chitosan ribbons allow the impregnation of dye molecules. SEM of MR-loaded sensor system revealed that UiO-66-Br penetrated through the voids during rehydration of padded dry sensor monoliths and got physically trapped in the fiber network. The morphology and size of UiO-66-Br particles were also determined using the SEM.

The average diameter was in the range of 132-163 nm and most of the particles had clearly geometric boundaries. Besides, the EDS elemental analysis was carried out. The result confirmed that the particles trapped in the network were UiO-66-Br particles, which were composed mainly of carbon, oxygen, bromine, and zirconium, which was in accordance with the previously reported data(Q. Fu et al., 2017; D. Ma et al., 2019). The physicochemical characteristic of UiO-66-Br particles was shown in **Table 5-3**.



(a)



(b)

Figure 5-28(a) SEM image of ice-templated methyl red@UiO-66-Br/Chitosan monolith with EDS result (left); and UiO-66-Br nanoparticles (right) (b) Infrared spectra of UiO-66 and UiO-66-Br nanoparticles (left). Infrared spectra of chitosan monoliths and UiO-66-Br/ Chitosan monoliths (right).

Table 5- 1 2 Comparison between UiO-66 and UiO-66-Br nanoparticles

	Particle size (nm)	PDI	Mass (g/mol)	Geometric surface area (m^2/g)	BET surface area (m^2/g)
UiO-66	143.12	1.64	8720.29	1550.73	1110
UiO-66-Br	156.31	0.87	10857.11	1164.60	851

Figure 5-7b shows the infrared spectrum in the region of the skeletal mode of the samples. At lower frequencies, peaks due to O-H and C-H bending were mixed with Zr-O peak (main bands at 746 cm^{-1}). In Zr-O_2 (**Figure 5-7b**, left), a twin-peak at 725 and 620 cm^{-1} has been assigned to longitudinal and transverse peaks, respectively. Strong changes occurred between UiO-66 and UiO-66-Br due to the band associated with DMF (1667 cm^{-1}) and C-Br (668 cm^{-1}). The unique peaks of chitosan were observed at 3410 (ν_{O-H}), 1413 (δ_{N-H}), 1623 ($\nu_{C=O}$), and 1088 cm^{-1} (ν_{C-N}). After mixing UiO-66-Br with chitosan, the typical peaks of chitosan and MOF particles were all observed in the UiO-66-Br/Chitosan spectra, indicating UiO-66-Br particles were successfully incorporated onto the chitosan via the adsorption process. In this study, UiO-66-Br was placed in chitosan dispersion until equilibrium was reached. According to a previous report, this mechanistic process often followed three consecutive steps: diffusion, attachment, and rearrangement/relaxation. Finally, UiO-66-Br nanoparticle and chitosan chain formed a stable ice-templated macropores monoliths system(Q. Fu et al., 2017; D. Ma et al., 2019).

5.4.4 Deep learning-enabled freshness recognition

For the concept-proof purpose, we applied the newly developed sensor array to monitor the freshness of shrimp. To demonstrate the superiority of accuracy, the ED value method was applied and compared with deep learning models. Meanwhile, to obtain the best results, four state-of-the-art DCNN models were involved simultaneously, VGG, Inception V3, WISsR, and

Resnet-50, respectively. The sensor arrays were glued on the bottom of lunch boxes without touching shrimp samples (**Figure 5-8a**).

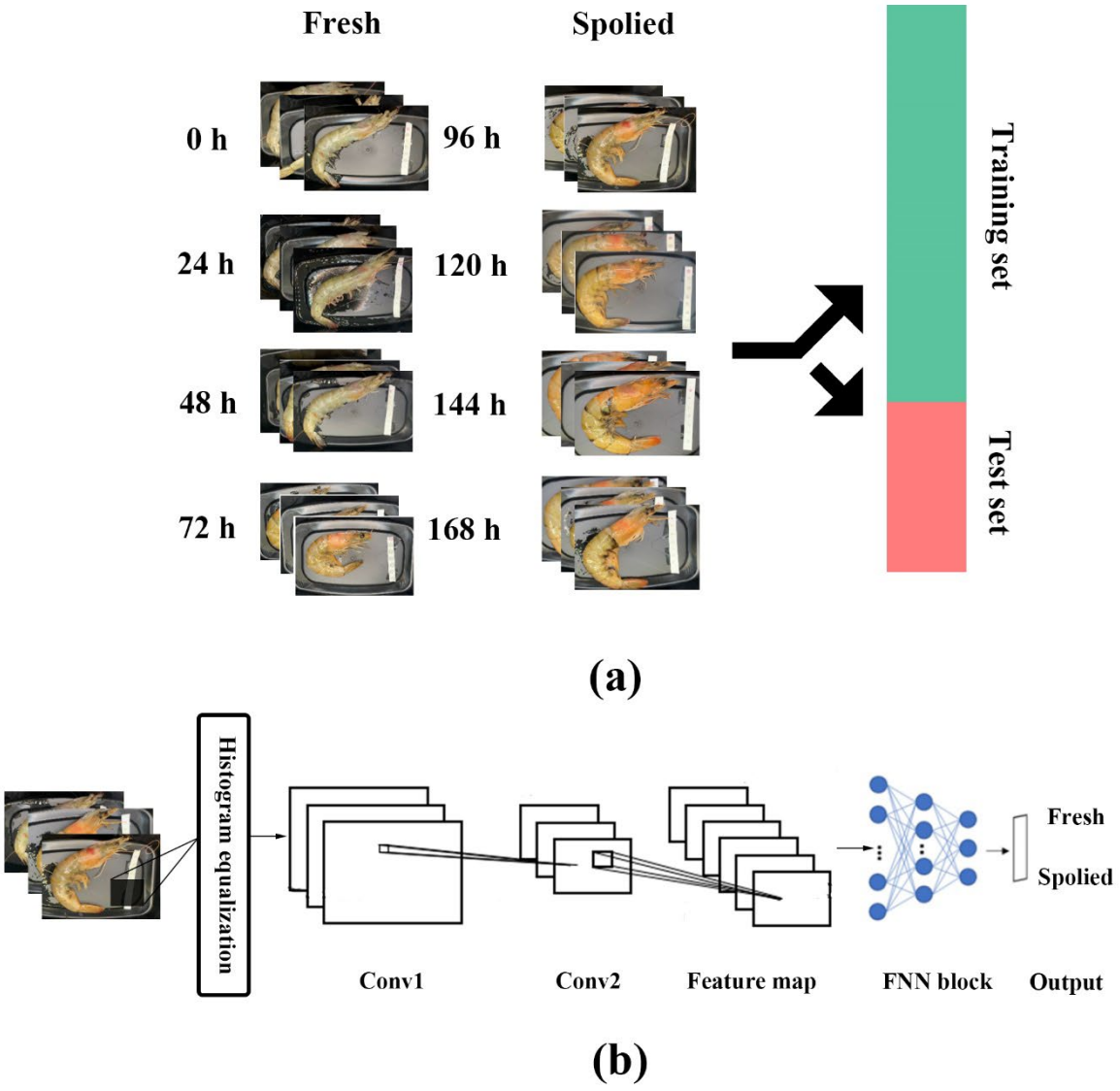


Figure 5-29(a) The shrimp with sensor array images database structure. The database contained 31584 images for model training and 13537 images for testing labeled with reference TVB-N result; (b) The DCNN models were used for shrimp freshness classification.

The shrimps were sealed in lunch boxes and stored at 4°C. Images of the sensor arrays were taken at different time intervals by an iPhone 11 max. According to a previous report, shrimps with TVB-N values less than 30 mg/100g were considered fresh, whereas higher than

30mg/100g indicated inedible and spoiled. To classify the sensor array into these two categories of freshness, the TVB-N value of the shrimp was tested by the Conway method. Then images were labeled as fresh and spoiled according to this standard. The overall pattern changes in reference measurements of TVB-N contents during a period of 168 hours cold storage period was illustrated in **Figure 5-9**.

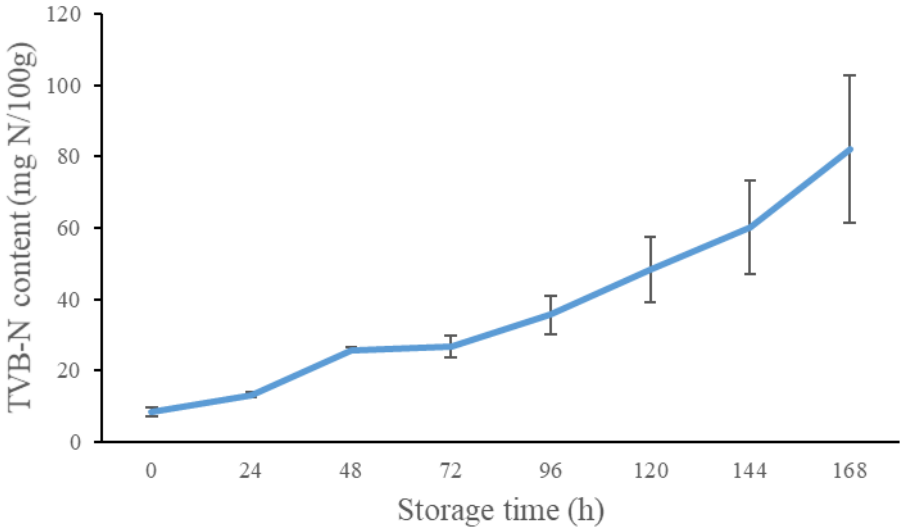


Figure 5-30 The pattern change of TVB-N content in Penaeus monodon during cold storage.

A total of 45,121 images of shrimp and sensor array were obtained and formed a dataset for machine learning evaluation of shrimp freshness. As mentioned in the method section, the dataset was first randomly split into a training subset and a testing subset with a ratio of 7:3, which means 31,584 images for model training and 13,537 images for testing. A True/False image classification network with different DCNN backbones, which comprised of input, multiple convolutions, full connection, and output layers was designed. The trained DCNN extracted features from images that contained sensor arrays and shrimp, afterwards, images were classified into one of the two categories, annotated fresh (true) and spoiled (false). Among four

state-of-art DCNN models, the WISeR50 model showed the highest accuracy for freshness prediction, up to 99.94%, whereas VGG16 showed 98.51%. Besides, to illustrate the superiority of deep learning, ED values were applied for compassion with the DCNN model. Following previous research, we randomly selected 50 sensor array images from fresh and spoiled categories to assess the prediction accuracy of ED values(Guo et al., 2020). In the end, the ED values achieved an overall prediction accuracy of 56.05%, which is significantly lower than those from DCNN models indicating it is difficult to distinguish fresh from spoil using ED value in practice (**Figure 5-10a**).

Table 5- 1 3 The accuracy comparison results between the ED value method and four state-of-art DCNN models

Models	Accuracy
Euclidean distance	56.05%
VGG16	98.51%
ResNet50	99.75%
WISeR50	**99.94%**
Inception-V3	98.90%

Due to the superior accuracy of the DCNN algorithm, the model can reduce the interfering effect caused by photo-taking environments, including angle, lighting, and white balance when compared to values from the ED method. This superiority of DCNN could be explained by the algorithm of the fitness model and data structure. RGB values of the sensor array do not linearly change with the concentration of gases, thus the non-linear DCNN algorithm was consistent with mathematical similarity(Ciocca et al., 2018). Besides, as epochs (i.e. the number of passes the algorithm completes through the entire database) increase, the loss (i.e. the difference between predicted and actual result) approaches 0 and keeps in a plateau after 400 epochs (**Figure 5-10b**). This result proved that the training model was effective and after 400 epochs, all models achieved their highest accuracy for image-based freshness prediction. The comparison of four DCNN models confusion matrix was shown in **Figure 5-10b** whose diagonal showed the number of correctly classified samples further illustrating the classification accuracy. In the statistical analysis of binary classification, the F_1 score is an indicator of test accuracy following **Equation 5-6**:

Equation 5-16

$$\boldsymbol{F_1 = \frac{tp}{tp + 0.5(fp + fn)}} \quad \textbf{(6)}$$

where tp is the number of true positives;

fp is the number of false positives;

fn is the number of false negatives.

It is the harmonic mean calculated from the precision and recall of the test, which might be a better measure to use when needed to seek a balance between precision and recall. F_1 score is often used in the field of information retrieval for measuring search, query classification, document classification, and machine learning. For this research, the WISeR50 DCNN model still showed the highest F_1 score, up to 0.9994 whereas the lowest by VGG16, around 0.9853. This result confirmed that the WISeR50 DCNN model was preferable for identifying the freshness of shrimp with sensor arrays pictures.

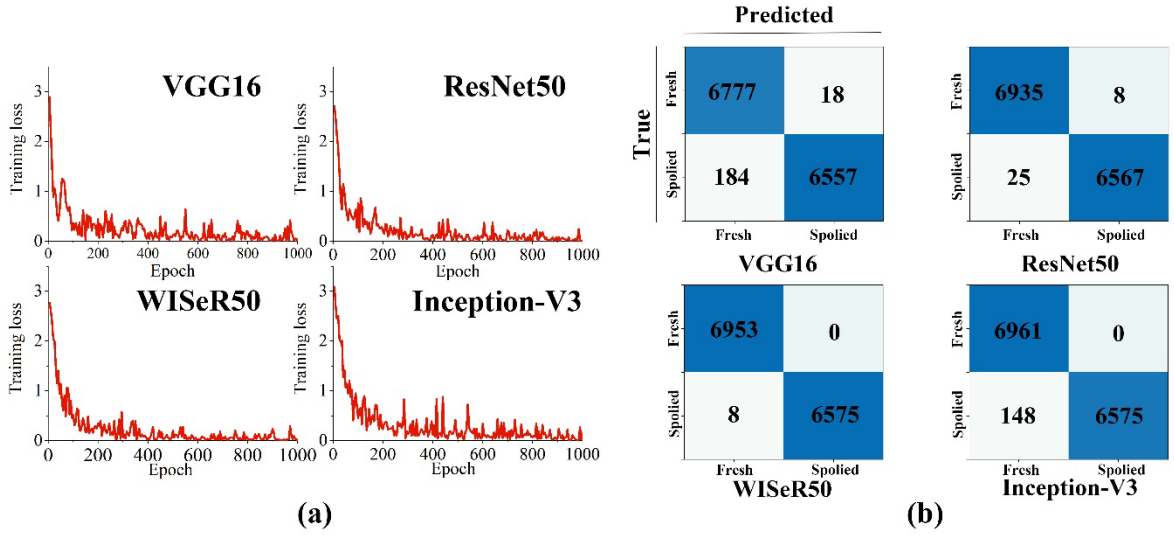


Figure 5-31(a) The relation between DCNN models training loss with the increase of training epoch; (b) The confusion matrix of four DCNN models.

Due to the higher accuracy of DCNN models than conventional machine learning models, it would be advantageous to apply them in colorimetric sensor array recognition and classification task. Furthermore, there are many other sensor arrays available for a good candidate which could

take advantage of the DCNN model and promise to achieve higher accuracy. This platform may be applied to other colorimetric sensor array systems or for a different task. The key advantage of this method is to maintain a high accuracy of image classification whilst the image database can be established easily.

Conclusion

By leveraging an integrated cross-reactive colorimetric sensor array with a DCNN platform, we developed a novel colorimetric sensor array was developed to rapidly and accurately monitor shrimp freshness in real-time. The ice-templated Dye@chitosan/UiO-66-Br sensor system, which was optimized by DFT and GCMC simulation showed significantly better sensitivity than unmodified UiO-66. The sensor array platform successfully detected gases released by spoiled shrimps (i.e. NH_3, MA, and TMA) and formed a scented fingerprint. All DCNN exhibited remarkably better accuracy than commonly used ED analysis, with the highest accuracy of 99.94% obtained by the WISeR50 model. Our developed sensor array platform has great potential to be applied in smart food packages and this work shed light on both reticular chemistry and artificial intelligence technology utilization in food research and industry.

Chapter 6 Development integrated portable chicken-freshness prediction platform based on UiO-66-loaded MOF-MMM colorimetric combinatorics

6.1 Abstract

The static labels presently prevalent on the food market are confronted with challenges due to its assumption that a food product only experiences a limited range of predefined handling and storage conditions, which cause the rise of uncertain safety risks or waste of perishable food products. Hence, integrated systems for measuring real-time food freshness have been developed for improving the reliability, safety, and sustainability of the food supply. However, these systems are limited by poor sensitivity and accuracy. Here, metal-organic framework mixed-matrix membrane (MOF-MMM) and deep learning technology were combined to tackle these challenges. UiO-66-OH and polyvinyl alcohol (PVA) were fabricated as colorimetric sensor array composites, which were impregnated with five chromogenic indicators. The sensor array system underwent color changes after being exposed to volatile organic compounds (VOCs) at different pH conditions. Four state-of-art deep convolutional neural networks (DCNNs) were applied to recognize the color change, endowing it with high-accuracy freshness estimation. The limitation of detection (LOD) of 80 ppm for trimethylamine was obtained, which was practically acceptable for the food industry. Moreover, 3D printing was applied to create a mold for possible scale-up production. The simulation test for chicken freshness estimation achieved accuracy up to 98.95% by the WISeR-50 algorithm. A portable food freshness detector platform was conceptually built. This approach has the potential to advance integrated and real-time food freshness estimation.

6.2 Introduction

Based on the previous chapter, which applied the ice-template monolith method to develop a MOF sensor array due to its more sustainable, high sensitive, and selective, mixed-matrix membrane would also be considered since they are easy to cast off, which means cheaper and stable in practice.

Food labels currently used only provide consumers with rough guidance to their expected shelf-life since manufactories assume that a product only experiences a limited range of predefined handling and storage conditions(Xiao-wei et al., 2018). These static labels were confronted with two major challenges: (a) they do not take into consideration of conditions that shorten shelf-life, such as temperature abuse and the difference between batches(Corradini, 2018), and (b) perishable food waste caused by the over-cautious allocation of the expiration date was account for approximately 35% production annually, according to a report from the united states department of agriculture (USDA)(Van der Werf et al., 2017; White et al., 2020). Therefore, novel analytical tools that are able to determine the safety and quality attributes in real-time and accurately estimate of shelf-life of food products have the potential to contribute to market value as well as sustainable development.

Ideally, real-time shelf-life estimation for foods would satisfy the following requirements(Corradini, 2018; Guo et al., 2020; Xiao-wei et al., 2018): a) the complexity of natural foods requires the detection system to input multiple attributes' indicators for shelf-life estimation; b) select reliable indicators and sensors that monitor an actual deterioration of the product and process relevant outputs; c) integrate real-time computing to determine the current freshness and estimate shelf-life of the product based on in situ observations. At present, the mainstream approach is to mimic the mammalian olfactory system to develop an artificial scent screening system, which has been applied in the detection of drugs, explosives, and rapid food

analysis. However, considering that the kinetic of the food deterioration process was influenced by multiple factors, such as nutritional loss, microbial growth, environmental factors, etc, conventional methods that integrate metal oxides or colorimetric dyes to cross-reactive sensor array suffered from poor sensitivity and low accuracy(J. Chen et al., 2018; Yang et al., 2021). To address these challenges, we took the advance of reticular chemistry, metal-organic framework mixed-matrix membrane (MOF-MMM) in specific, helped with deep learning technology to achieve the practical and acceptable accuracy for food freshness estimation system.

Metal-organic frameworks (MOFs), which comprise a family of highly porous and chemically mutable materials, offer various advantages and thus are considered as promising additives for mixed matrix membranes (MMMs)(Dechnik et al., 2017). The chemically diverse and controllable MOF structures (by judicious selection of ligands with appropriate chemical functionalities) can be prepared to facilitate strong interactions with polymer bulk materials, which improve the selectivity of MMMs by reducing the micro gaps between inorganic and organic phases(Cheng et al., 2021; Y. Zhang et al., 2016). Furthermore, the chemical mutagenicity of MOF can be embraced to provide enhanced adsorption to particular chemical species(K. C. Kim et al., 2013). Besides, due to the high complexity of image-based pattern recognition, traditional statistical methods, including principal component analysis (PCA), hierarchical cluster analysis (HCA), etc, cannot be used to accurately analyze the images(S. Cai et al., 2019). Therefore, the latest breakthroughs in computer vision research proved deep convolutional neural network (DCNN) and its derivative algorithms as the key for image recognition and have exhibited superiority in dietary monitoring, food supply chain evaluation, and food quality detection(Guo et al., 2020; Yang et al., 2021).

Here, the MOF-MMM system was for the first time introduced to prepare a food freshness sensor array. When compared to other materials, e.g. organic polymer membranes sensor array or inorganic membranes, a balance between production cost, gas selectivity, and stability is obtained by the MOF-MMM system. MOF-MMM was synergized to overcome the low sensitivity and DCNN technology was applied to improve the accuracy of the cross-reactive colorimetric sensor array system. The UiO-66-OH/PVA MOF-MMM system was developed and systematically characterized. Moreover, a real-time sensor array fingerprint pattern recognition by DCNN was optimized after the comparison of four state-of-arts DCNN models. Finally, we integrated the MOF-MMM sensor and DCNN image recognition system together to achieve the prediction of chicken freshness with an accuracy of up to 98.95%.

6.3 Materials & methods

6.3.1Materials

Zirconium tetrachloride (99.5%), benzene-1,4-dicarboxylic acid (BDC, 98.0%), 2-hydroxyterephthalic acid (BDC-OH, 98.0%), N,N-dimethylformamide (DMF, 99.0%), Nile red, Poly(vinyl alcohol) (PVA, Mw 85,000-124,000), ammonia hydrogen solution (25% in water), methylamine solution (33% in absolute ethanol), trimethylamine solution (45% in water), acetic acid (HAc, 99.9%), boric acid, (99.8%), 2-methoxyethanol (99%) and 6 dyes, i.e. methyl red (MR), 5,10,15,20-tetraphenyl-21H,23H-porphine zinc (Zn-TPP), curcumin (CUR), chlorophenol red (CPR), bromocresol purple (BCP), and bromophenol blue (BPB) were purchased from Sigma-Aldrich (St. Louis, MO, USA, detail of dyes were presented in Table S1). All chemicals are in analytical grade. The chicken breast was bought from Costco Wholesale Corporation (Seattle, WA, USA). The microwave container (38 oz) was bought from a local market (SafePro, MD, USA).

6.3.2 Synthesis of UiO-66 and UiO-66-OH

The UiO-66-OH was synthesized by a solvothermal method according to a previous report with minor modification(P. Ma et al., 2020). First, ZrCl4 (1.17 g, 5 mmol) and BDC-OH (0.92 g, 5 mmol) or benzene-1,4-dicarboxylic acid (0.83 g, 5 mmol), and acetic acid 1.0 mL were dissolved in DMF (30 mL) at room temperature. The UiO-66 particle was synthesized by replacing BDC-OH with BDC (0.89 g, 5 mmol). Then, the mixture was placed in a Teflon-lined stainless-steel autoclave after adding 2 ml of de-ionized water and mixing completely. The autoclave was placed in an oil bath at 121°C for 24 h. Afterward, the solution was cooled to room temperature for 30 min, and the resulting UiO-66 and UiO-66-OH particles were separated via centrifugation (12,096 × g, 10 min) at room temperature and washed three times with ethanol. The resulting white powder was dried in an oven at 40°C for 4 h and tested by XRD and SEM for verification.

6.3.3 Synthesis of dye@UiO-66/PVA and dye@UiO-66-OH/PVA MMM

PVA resin (1 g) was first dissolved in double-distilled water at 90°C for 1 h with stirring to obtain 10 wt% PVA aqueous solution. To avoid aggregation during the drying process, UiO-66 or UiO-66-OH nanoparticles, 200 mg, were first dispersed in 50 mL water with an assistant by ultrasound. A certain volume of the prepared MOFs dispersion was diluted with deionized water to a final volume of 27 mL. Subsequently, 2.5 mL PVA aqueous solution and 0.5 mL dye solution (e.g. 5 mg/mL in 2-methoxyethanol) were added in it. After vigorous stirring, 0.2 mL of each solution was transferred to its assigned well on a 96-well plate, with a diameter of 6 mm for each pore. After that, a 96-well plate with the solution was degassed and dried in a vacuum at 43ºC for 24 h. All films with different dyes were adhered to on paper tape to form the sensor array.

6.3.3 Calculation of amine gas concentration.

Detection experiments on amine gases were performed in standard Petri dishes (100 * 15 mm) with temperature-controlled at 20°C. The colorimetric sensor array was placed on the cover of the Petri dishes. The required gas concentration was reached by injecting a certain volume of liquid analyte (i.e. ammonia (NH_3), methylamine (MA), and trimethylamine (TMA)) into the dish and sealed with parafilm. The resulting gas concentration (C_{ppm}) was calculated using the following equation **Equation 6-1**:

Equation 6-17

$$C_{ppm} = \frac{V_{\mu L} \times D_{mg/L} \times W}{M_{g/mol} \times V_L} \times 22.4 \times 10^7$$

Where $V_{\mu L}$ is liquid analyte volume;

$D_{mg/L}$ is the liquid density;

W is the mass fraction of the liquid;

$M_{g/mol}$ is the molecular weight of the liquid analyte;

V_L is the volume of Petri dishes.

6.3.4 Scanning electron microscope (SEM)

Samples were scooped into a 10 mm cup and placed into a shuttle, which was frozen conductively, in a Styrofoam box, by placing the brass plates on the surface of a pre-cooled (-196°C) brass bar whose lower half was submerged in the liquid nitrogen. After 20-30 s, the shuttle containing the frozen sample was transferred to a Quorum PP2000 cryo-preparation chamber (Quorum Technologies, East Sussex, UK). The top layer of the frozen sample was cryo-fractured using a metal blade mounted inside the preparation chamber. All specimens were etched inside the cryo-preparation system to remove any surface contamination (condensed water vapor) by raising the temperature of the stage to -90°C for 10-15 min. Following the etching, the temperature inside the chamber was lowered below -130 °C, and the specimens were

coated with a 10 nm layer of platinum using a magnetron sputter head equipped with a platinum target inside the cryo-preparation chamber. The specimens were transferred to a pre-cooled (-130°C) cryo-stage in the SEM (Tescan XEIA FEG SEM, Brno, Czechia) for observation. An accelerating voltage of 5 kV was used to view the specimens. Images were captured using a 4pi Analysis System (Durham, NC)(P. Ma, Zhang, Teng, et al., 2021).

6.3.5 Fourier transform infrared (FT-IR) spectrometry

The samples (UiO-66/PVA MMM and UiO-66-OH/PVA MMM, 3-5 mg) were mounted onto a Jasco FT-IR 4100 spectrometer (Jasco Inc., Easton, MD, USA) coupled with an attenuated total reflectance accessory (ATR). The infrared transmittance was acquired at the wavenumbers from 600 to 4000 cm^{-1} with a resolution of 2 cm^{-1}. Sixty-four repeated scans were undertaken for each sample. The spectra were averaged, smoothed, corrected for their baselines, and converted to absorbance with Spectra Manager software (Jasco Inc., Easton, MD, USA)(Mei et al., 2017).

6.3.6 UV−Vis Spectrophotometry

The sample after being loaded with different dyes was quantified using ultraviolet−visible spectrophotometry. Six different diluted dye@UiO-66-OH/PVA solutions were prepared from the bulk solution in a volumetric flask (30 mL). Each sample was controlled to a pH 6 environment using a 1 mL buffer solution. Thus prepared samples were analyzed by scanning the quartz cuvettes. The scanning wavelength was in the range of 300 – 650 nm.

6.3.7 Thermogravimetric analysis (TGA)

Thermal analysis of the UiO-66, UiO-66-OH, UiO-66/PVA, and UiO-66-OH/PVA samples was performed using a thermogravimetric analysis (TGA) instrument (2950, TA Instruments Inc., New Castle, DE). The parameters were modified from a previous study, under

a mixed air and N_2 flow of 100 mL min^{-1} (40% air, 60% N_2) with a heating rate of 10 K min^{-1} from 308 K to 1073 K(P. Ma, Zhang, Tsai, et al., 2021).

6.3.8 Crystal structure of MOFs

X-ray powder diffraction (XRD) patterns were obtained from an XRD diffractometer (C2 Discover Bruker Diffractometer, Madison, WI, USA) with CuKα radiation to evaluate the crystal structure of UiO-66 and UiO-66-OH. X-ray scan ranged from (2θ) 3.5°–30°, step size at 0.02°. The XRD pattern simulation was calculated by a simulation tool, VESTA, with wave angle from 1 to 30 degrees, and relative intensity was set to 1(P. Ma, Zhang, Tsai, et al., 2021).

6.3.9 Particle size and polydispersity index (PDI)

Hydrodynamic diameters of UiO-66 and UiO-66-OH were measured by a dynamic light scattering (DLS instrument (BI-200SM, Brookhaven Instruments Corp., Holtsville, NY), which was equipped with a 35mW HeNe laser beam at a wavelength of 637 nm. All DLS measurements were performed three times at 25°C(P. Ma, Zhang, Teng, et al., 2021).

6.3.10 Surface charge

The electrophoretic mobility was determined at a pH range of 2.0 to 7.0 using a Zetasizer Nano ZS (Malvern Instruments, Worcestershire, UK). Each sample was measured three times in disposable folded capillary cells (DTS 1070, Malvern Instruments Ltd, Worcestershire, UK) at a particle concentration of 0.1 wt%, and at least 32 runs were performed per measurement. The pH value was adjusted by adding HCl and NaOH dropwise and measured by a pH meter(P. Ma, Zhang, Teng, et al., 2021).

6.3.11 Determination of swelling index

The swelling index was used to evaluate the swelling ability of each membrane when the polymer matrix was immersed in water. Each film was weighed (M_{dry}) at first. Then, these films

were immersed in water at room temperature. Each membrane was taken out from the water and reweighed periodically until a constant membrane weight was maintained ($M_{swollen}$), indicating that equilibrium was reached. The swelling index of films or water uptake was determined by the following equation **Equation 6-2**(Pounds et al., 2021):

Equation 6-18

$$\boldsymbol{Swelling\ index}\ (\%) = \left(\frac{\boldsymbol{M_{swollen} - M_{dry}}}{\boldsymbol{M_{dry}}}\right) \times \mathbf{100}\%$$

6.3.12 Solubility Determination for MOF/PVA-MMM

The membrane sample of each film was dried in an oven at 100°C for 24 h. Then, it was weighed to obtain the initial dry content of each membrane (W_i). After this, all membrane samples were placed in water and maintained at 30°C for 24 h in a sealed beaker under stirring. Then, the membrane samples were taken out, rinsed, and dried in an oven at 100°C until constant weight (W_0). Membrane solubility was determined by the following **Equation 6-3**(Pounds et al., 2021):

Equation 6-19

$$\boldsymbol{Solubility}(\%) = \left(\frac{\boldsymbol{W_i - W_0}}{\boldsymbol{W_i}}\right) \times \mathbf{100}\%$$

6.3.13 Total volatile basic nitrogen (TVB-N) measurement

To mimic the storage conditions at supermarkets, 200 ± 30 g of fresh chicken breast, without any pretreatment was placed in a plastic box. One sensor array per package was attached to the inner side of the box. The chicken was stored at 4°C before analysis.

To test the freshness of chicken without the interference of image collection, a separate group of 24 (8 storage intervals x 3 parallel experiments) packages of chicken was prepared for TVB-N testing. Ten grams of minced chicken sample were homogenized with 100 mL of distilled water (Ultra-Turrax T25, IKA, Staufen, Germany). The mixture was filtered 30 min

later to obtain a liquid sample. Then, 3 mL boric acid absorbing solution (20 g/L) and 50 μL pH indicator (methyl red: bromocresol green = 1:5, v/v) were added to the inner chamber of Conway dish (diameter 90 mm). In the outer chamber, 3 mL potassium carbonate saturated solution and 1 mL sample liquid were added in sequence. The Conway dish was kept sealed and incubated at 37℃ for 2 h. The volatile amine gases were absorbed by boric acid as an absorbing solution. The abovementioned mixture was then titrated using 0.1 mol/L hydrochloric acids (HCl), and the number of volatile amines was calculated with the following **Equation 6-4**.

Equation 6-20

$$\boldsymbol{X = \frac{(v1 - v2) \times C \times 14}{m \times 0.05} \times 100}$$

Where, X is TVB-N content in the sample (mg/100g), *v*1 is the volume of 0.1 mol/L HCl used for the actual test (mL), *v*2 is the volume of 0.1 mol/L HCl used for the control test (mL), C is the HCl concentration (mol/L), 14 is the weight of nitrogen, and m is the weight of the sample (g).

6.3.14 Circular region of interest (CROI) identification

Hough circle transform was applied to recognize the color area of the sensor array. The circled candidates were produced by "voting" in the Hough parameter space and then selecting glocal maxima in an accumulator matrix. To obtain the best result, the inverse ratio of the resolution was set to 1, the upper threshold for the internal Canny edge detector was set to 15, the threshold for center detection was set to 13, and the range of radius to be detected was [20,40) pixel. The CROI was extracted from the seven dye region labeled by the Hough circle transform.

6.3.15 Database preparation and images collecting for DCNN training

To collect data from the sensor, 5 s of a short video for each box was taken with chicken at a certain storage interval. During the 5 s, the color and intensity of the background light in the

photo box changed according to the program settings. Eight intervals that covered the spoilage process were selected. During the data collecting period, a portion of chicken was examined for TVB-N, and others were used for image acquisition. Noted that, we changed the light that was included in the input images and photoed them by iPhone 11 Max Pro for training to fully mimic real application scenarios. The 60 fps video was then randomly sampled at 10 fps and exported as an image set. Based on the actual measured TVB-N results and chicken freshness criteria, we labeled samples with <28 mg N/100 g as fresh and >28 mg N/100 g as spoiled based on the previous sensory (odor) and microbial analysis according to a published paper (Balamatsia et al., 2006). It's worth note that there are other freshness standards for chicken, from 15 mg N/100 g to 34 mg N/100 g(Alaa et al., 2021). And the final database was split into a training set and a testing set at ratio 7:3. The final training set contained 4492 labeled images and the test set contained 1927 images. The fresh to spoiled ratio was 1:1 in both the training set and the test set.

6.3.16 Network architecture

The final step was to train CNN models on the training set for image classification and evaluate the model inferences on the validation set. Four different deep convolutional neural network architectures were used: VGG(Simonyan et al., 2014), ResNet(K. He, Zhang, Ren, & Sun, 2016a), Wide ResNet(Zagoruyko et al., 2016), and Inception V3(Szegedy et al., 2015). These four CNN architectures achieved good results on the most state-of-arts and challenging image classification dataset, ImageNet-1000, which consisted of roughly 1.2 million training images in total, including 50,000 validation images and 150,000 testing images in 1000 diverse classes(J. Deng, Dong, Socher, Li, Li, & Fei-Fei, 2009). Therefore, these four network architectures would be a defensible optimal to test on our dataset.

VGG was a convolutional neural network model improved from AlexNet, which was the winner in the ImageNet Large Scale Visual Recognition Challenge (ILSVRC) 2012(Krizhevsky, Sutskever, & Hinton, 2012). VGG used larger kernel-sized filters (11 and 5 in the first and second convolutional layer, respectively) with multiple 3×3 kernel-sized filters one after another. This modification made it achieve a 92.7% top-5 accuracy in ImageNet and is regarded as one of the most successful models submitted to ILSVRC-2014. ResNet was a deeper network, and we used the ResNet-152 variant of the ResNet architecture, which had 152 layers. ResNet consisted of shortcut architecture and solved the problem of high training error when more layers were added. Similar to ResNet, Wide ResNet applied the shortcut structure in ResNet but with a larger feature channel in each convolutional layer. They showed that a shallow model with 16 layers could significantly outperform 1000-layer deep networks. Inception V3 increased the network space from which the best network to be chosen via training with different inception modules. Global features, distributed features, and low-level features were all extracted by different inception modules, including 1x1 Conv layer, 3x3 Conv layer, 5x5 Conv layer, and max-pooling layer.

6.3.17 Statistical analysis

Data on particle size, surface charge, swelling index, and solubility were collected from three true triplicates and were reported as the mean ± standard error. Data were analyzed by a one-way analysis of variance using the SPSS 16.0 package (SPSS Inc., Chicago, USA). The significant level was set at p=0.05.

6.4 Result and discussion

6.4.1 MOF-MMM materials identification

Usually, meat products need to travel from their wild or farm origin, through processing, packaging, and distribution chains, to end-value consumers. During this process, proteins in rotting meat or seafood are microbially decomposed into peptides and amino acids and further degraded into amines and ammonia. Hence, the design of the sensor array for food freshness detection would be practical as indicators for four categories: ammonia gas response (e.g. metal-oxide tetraphenylporphyrin family), pH value response (e.g. litmus test), time response (e.g. phytochemicals oxidation over time), and microbial response (e.g. microbial metabolite indicators). For practical reasons, sensory deterioration and safety concerns are often applied to mark the end of shelf-life, so a single limiting attribute might not provide an accurate representation of the loss of acceptability. Here, five indicators were selected from other previous reports chromogenic responding to three attributes: (a) ammonia gas response: zinc tetraphenylporphyrin (TPP); (b) pH value response: methyl red (MR), chlorophenol red (CPR), bromocresol purple (BCP) and bromophenol blue (BPB); (c) time response: curcumin (CUR). The details of indicators were presented in **Table 6-1**.

Table 6-1 4 *The list of biocompatible chromophore dyes on the colorimetric sensor array*

	Name	Abbreviation	Color range
1	Methyl Red	MR	4.4 (Red)- 6.2 (Yellow)
2	Zinc Tetraphenylporphyrin	TPP	Amino gas
3	Curcumin	CUR	7.8 (Yellow)- 9.2 (Reddish Brown)
4	Chlorophenol Red	CPR	4.8 (Yellow) - 6.8 (Red)
5	Bromocresol Purple	BCP	5.2 (yellow) - 6.8 (Purple)
6	Bromophenol Blue	BPB	3.0 (Yellow) – 4.6 (Blue)

Compared to indicator selection, MOF and polymer selection for the preparation of the MOF-MMM system needs to be considered and are restricted by many factors, including gas adsorption performance, gas selectivity, structure stability, and safety. In the selection of MOFs,

UiO-66 and its derivatives have been widely studied in recent years due to their excellent stability, which could withstand up to 400^{o}C and keep its crystal structure stable in a wide range of pH values. Moreover, when selecting material applied in the food sector, toxicity should always be taken into consideration. Recent researches have found that UiO-66 was biocompatible and had low cytotoxicity in different cell lines, including human lung epithelial cell (AS49)(Rakhshani, Nemati, Saadatabadi, & Sadrnezhaad, 2021), breast cancer cell (MCF7)(Abánades Lázaro, Wells, & Forgan, 2020), mouse fibroblast cell (L929)(Y. Li et al., 2020), and alveolar macrophage cell (661W)(Gandara-Loe et al., 2018). Moreover, it was reported to be used in various bioapplications, such as drug delivery systems, antibacterial, and biocatalysis. Therefore, UiO-66 was selected as MOF material. Furthermore, functional groups, such as -NH_2, -OH, -CH_3, -COOH, -Cl, -Br can be introduced into UiO-66 by modification of H_2BDC-X ligand at the benzene ring under analogous reaction conditions, which impacts the gas selectivity and permeability(Demir et al., 2017). Therefore, density functional theory (DFT) was performed using clusters to screen a series of functional groups for selective adsorption of ammonia. The binding energy between UiO-66 or its derivatives and primary, secondary, and tertiary amines (named NH_3, MA, TMA, hereafter), which were a vital indicator for meat and seafood safety, was listed in **Table 6-2**. UiO-66-OH was selected due to its lowest binding energy with three selected amines, 65.64 kJ/mol, 77.42 kJ/mol, 64.64 kJ/mol for NH_3, MA, and TMA, respectively. At last, considering the safety and stability factors, poly(vinyl alcohol) (PVA), a biodegradable synthetic polymer that exhibited excellent chemical resistance, adhesive, film-forming, and mechanical properties, and was generally recognized as safe (GRAS) food package material, was selected to develop MOF-MMM with UiO-66-OH (UiO-66-OH/PVA, hereafter).

Table 6- 1 5 *Relative binding energy for NH_3, methylamine (MA), and trimethylamine (TMA) in UiO-66 as well as functionalized UiO-66 materials determined from periodic PBE-D2 calculations.*

Adsorbate	Adsorbent	Binding energy (kJ/mol)
UiO-66	NH_3	38.4
	MA	48.5
	TMA	37.0
UiO-66-NH_3	NH_3	45.0
	MA	54.2
	TMA	43.7
UiO-66-OH	NH_3	65.6
	MA	77.4
	TMA	64.6
UiO-66-Cl	NH_3	55.8
	MA	67.9
	TMA	54.6
UiO-66-NO_2	NH_3	56.6
	MA	68.3
	TMA	55.5
UiO-66-NH^{2+}	NH_3	56.6
	MA	68.3
	TMA	55.6
UiO-66-Br	NH_3	67.4
	MA	84.1
	TMA	65.8

6.4.2 Synthesis and morphologies of UiO-66-OH/PVA sensor array

UiO-66-OH was solvothermal synthesized following a previous report. The crystallography and morphology were charactered by powder X-ray diffraction (XRD) (**Figure 6-1**). And SEM (**Figure 6-2c**), which were found consistent with previous reports. To develop

MOF-MMM, particle size and surface charge of synthesized UiO-66-OH nanoparticles were characterized by DLS and Zetasizer, respectively (**Table 6-3**). The particle size of UiO-66-OH was 123.93 nm with a polydispersity index (PDI) of 9.8, which is consistent with SEM results and proves the uniformity of synthesized MOF NPs. Additionally, electrostatic interactions between MOF NPs and adsorbed amine molecules were investigated to better understand the adsorption process. The isoelectric point of UiO-66-OH was between ca. pH 3-4, which indicated when the pH value was lower than 3, the MOF NPs carried positive charges (7.4 ± 1.3 mV, pH 2) whereas pH higher than 4 they carried negative charges (-7.8 ± 0.6 mV, pH 5). The previous studies showed that the initial spoilage of meat or seafood occurs at approximately pH 6 and then the pH was further decreased to 4, while the zeta-potential values for ammonia were positive under this condition (shown in **Table 6-3**). The strong electrostatic attraction between UiO-66-OH and ammonia gases enables them to reach maximum adsorption during the food storage period. Besides, π–π stacking and hydrogen bonds between MOF NPs and adsorbed ammonia gas molecules may further improve the adsorption ability.

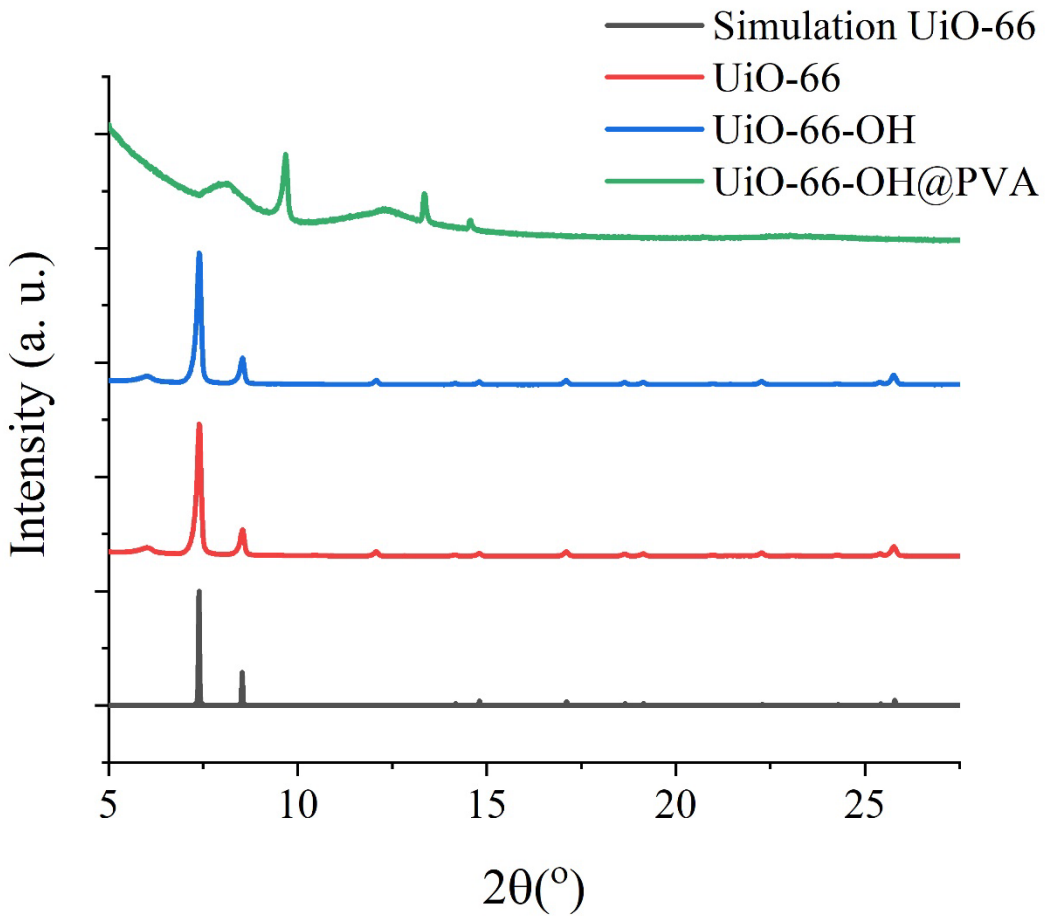


Figure 6-32 *X-ray diffraction (XRD) patterns of synthesized UiO-66-OH@PVA MMM, UiO-66 and UiO-66-OH compared with the simulated one for UiO-66*

Table 6-16 *Particle size and zeta-potential for UiO-66 and UiO-66-OH particles*

Material	Particle size (nm)	PDI	Zeta-potential (mV)		
			pH 2	pH 5	pH 7
UiO-66	143.12	1.64	39.1 ± 1.0	43.2 ± 1.6	48.0 ± 3.6
UiO-66-OH	123.93	9.8	7.4 ± 1.3	-7.8 ± 0.6	-10.4 ± 0.6

XRD was first utilized to examine the MOF particle and MOF-MMM system, and the results showed the same diffraction results for both UiO-66 and UiO-66-OH, which showed a clear crystal peak in the detect range. However, when prepared as a MOF-MMM system, only

the PVA peak was detected, a result consistent with other MOF-MMM-related reports. The results of the thermogravimetric analysis are shown in **Figure 6-3**. The UiO-66 was decomposed at 550-600ºC, but UiO-66-OH started to decompose from 400ºC, without a clear decompose stage. This was due to the defects brought by the hydroxyl groups, which affected the stability of MOF structures. For the MOF-MMM system, the thermogravimetric analysis showed decomposition in the range of 250-300 ºC, which is the thermal decomposition temperature of PVA. This result showed that the factor affecting the thermal stability of the system is mainly PVA. Also in the interval less than 100ºC, there was a 10% mass loss in the MMM prepared with UiO-66-OH since it binds more readily to water in the environment than the MMM prepared with bare UiO-66, resulting in a bigger mass loss due to volatilization of absorbed water during thermogravimetric analysis.

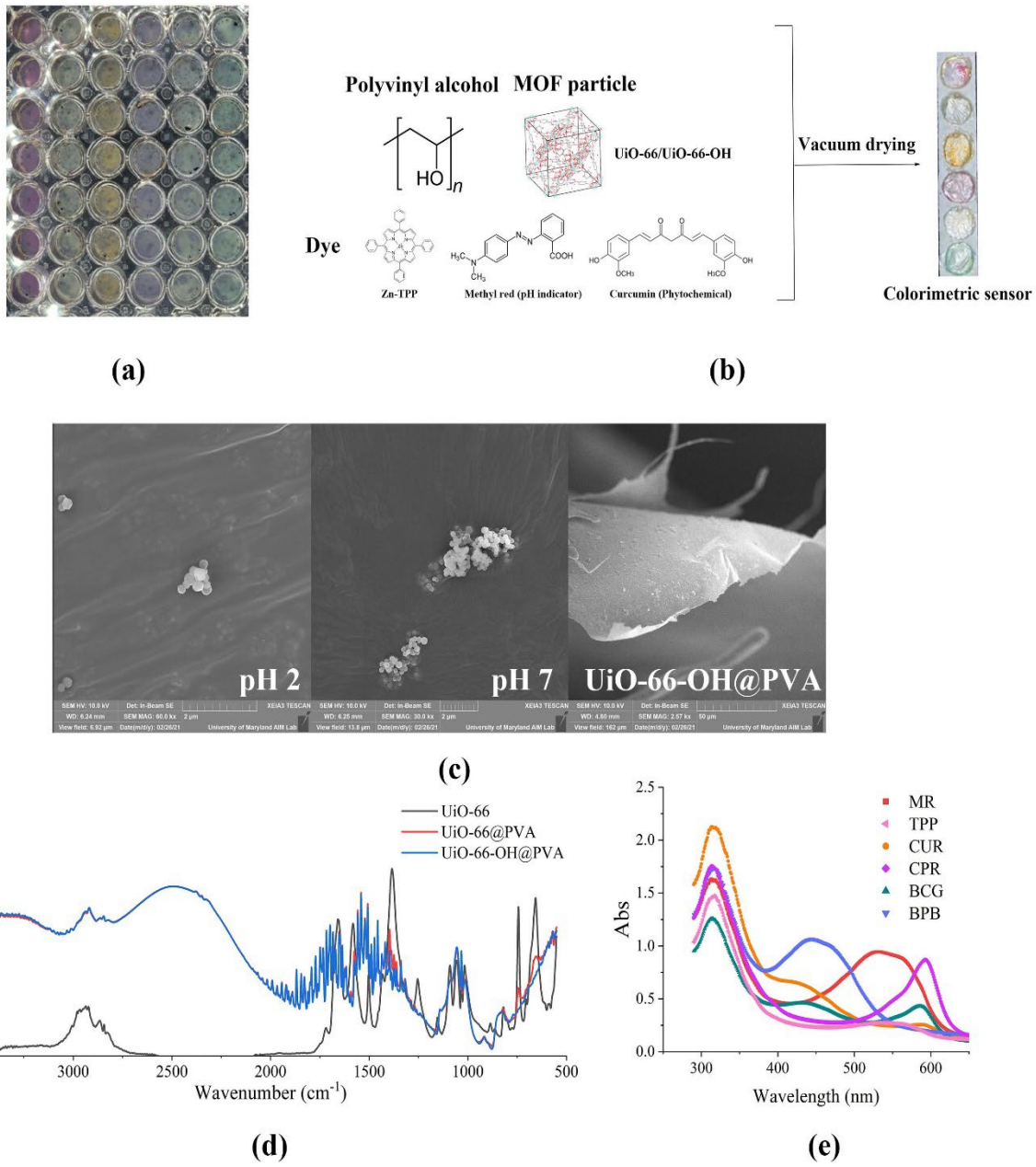


Figure 6-33 *Fabrication and characterization of colorimetric sensor array. (a) Schematic of sensor array in 3D printing mold. Each pore filled with six types of dyes with UiO-66-OH/PVA solution. (b) Schematic showing the fabrication of dye@UiO-66-OH/PVA sensor array. UiO-66-OH are cross-linked with PVA via hydrogen bond, and dye was adopted to the surface of UiO-66-OH. (c)Scanning electron microscopy image of UiO-66-OH NPs and pH2 (left), UiO-66-OH NPs at pH 7(middle) and UiO-66-OH/PVA film. (d) Infrared spectra of UiO-66 NPs, UiO-66@PVA film and UiO-66-OH@PVA film. (3) Spectral scanning of six different dye loaded in UiO-66-OH@PVA film. Scanning range from 300-650 nm.*

The UiO-66-OH/PVA film loaded with three categories of dyes was successfully synthesized (**Figure 6-2a**). The MMM system was directly formed on the PARAFILM M film by using a 3D-printed mold, which achieved a low cost and had the potential for mass production (schematic of sensor array fabrication shown in **Figure 6-2b**). To deposit the gas-sensitive sensors on PARAFILM film, six 100 μL dye@UiO-66-OH/PVA solutions were drop-casting onto the pore of mold, the diameter of each pore was 6 mm and the gap between the neighboring pore was 2 mm. Many studies have proved that gas transfer and sensing stability rely on the microstructure of the nanocomposites and their ability to store dye molecules(Guo et al., 2020; P. Ma, Zhang, Xu, et al., 2021). SEM was applied to observe the morphologies of the MOF particles at acidic to neutral pH values as shown in **Figure 6-2c**. The uniform MOF NPs kept their crystal structure with the particle size of approximately 100 nm and there were no observed changes for MOF NPs in different pH conditions. Meanwhile, no dye aggregation was found in the SEM images, indicating MOF NPs play a critical role as a carrier to disperse the dye, which was demonstrated in previous reports. Such a porous structure was expected to provide a large surface area and gas sensing site. Figure 1d showed the FTIR spectrum of MOF NPs and MOF MMMs. At lower frequencies, peaks due to O-H and C-H bending were mixed with Zr-O peak (main bands at 746 cm^{-1}). A twin-peak at 725 and 620 cm^{-1} was assigned to longitudinal and transverse peaks, respectively. MOF showed absorption bands at 1590 and 1390 cm^{-1} that were assigned to the -COOH groups. The aromatic region (C = C) of methyl red dye appeared at 1445 cm^{-1}.

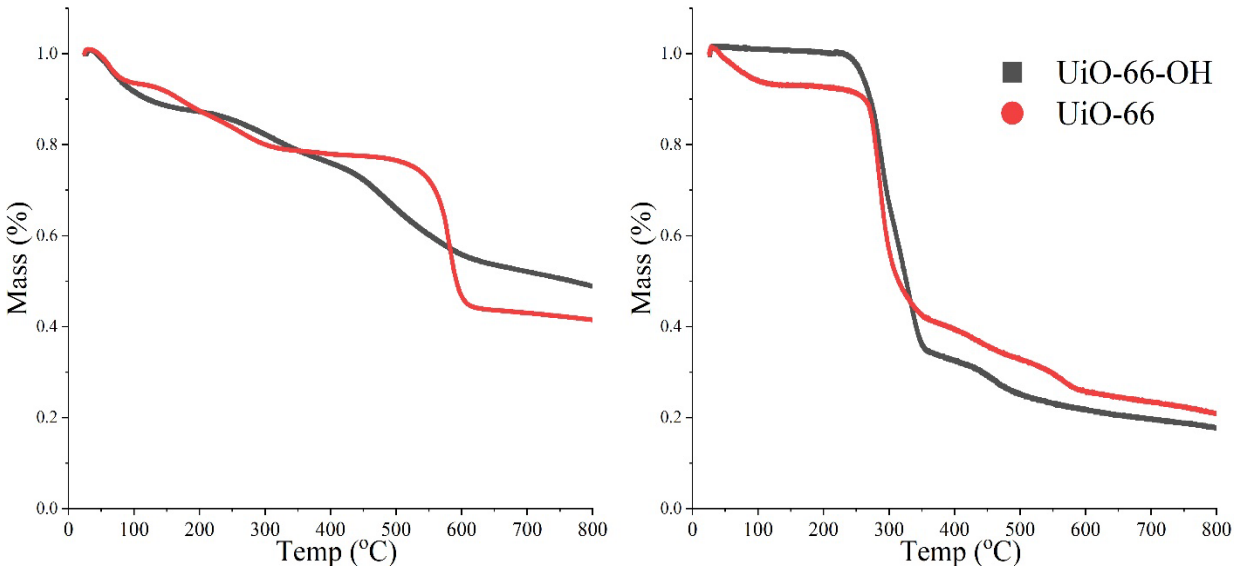


Figure 6-34 *Thermogravimetric analysis, UiO-66 and UiO-66-OH NPs (left) and UiO-66/PVA and UiO-66-OH/PVA (right)*

The maximum absorption peaks of the different dyes were detected using UV-Vis (**Figure 6-2e**). They were in the visible range of 400-650 nm, which indicated that the sensor color was effectively extracted using a CCD camera in the visible band of the mobile device. At the same time, the characteristic peaks of each dye were clearly visible, which indicated that the MOF-MMM system itself had little interference with the color.

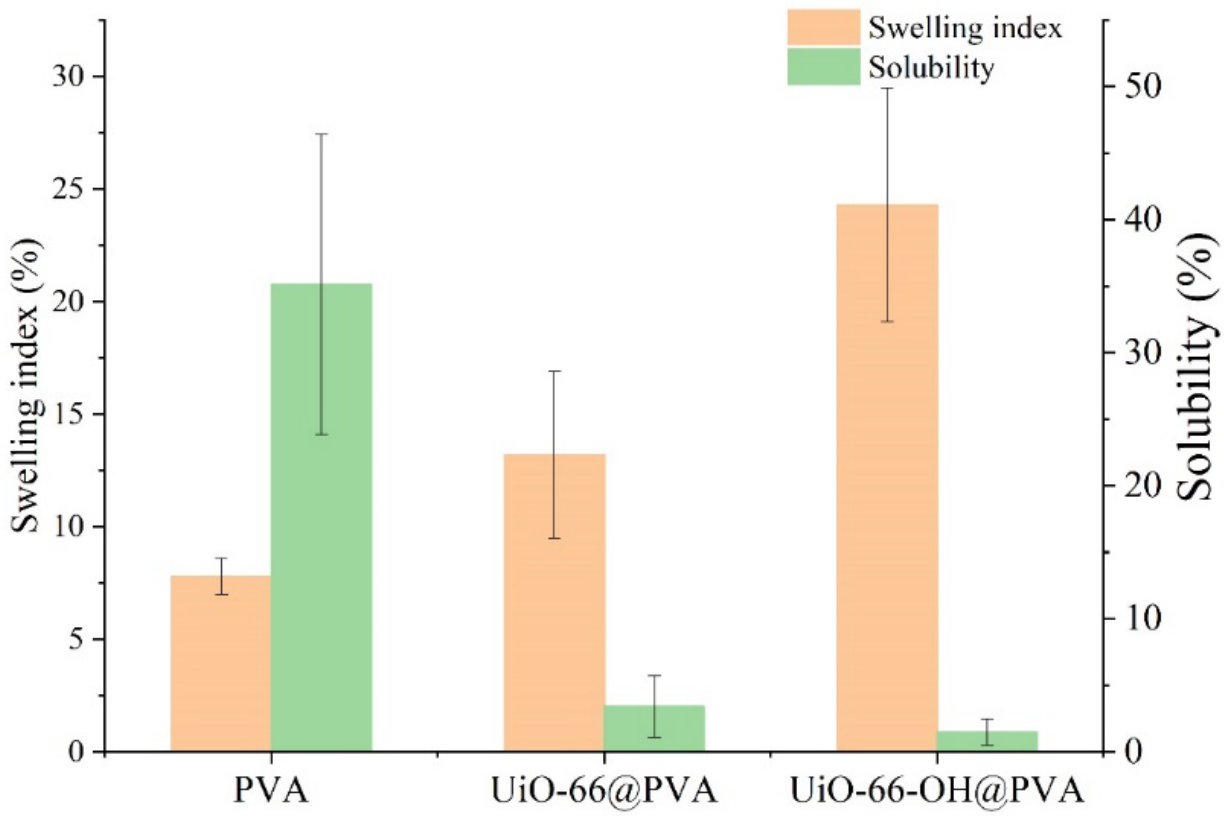


Figure 6-35 *Swelling index (%) and solubility of PVA film with two MOF-MMM films in an aqueous environment.*

To test its ability to satisfy the character requirement as a food package in practical conditions, water stability, thermal stability, mechanical properties were characterized. First, dye leakage and swell index were tested by immersing Nile red-loaded UiO-66-OH/PVA films (NR@UiO-66-OH/PVA) in water with Nile red-loaded PVA film (NR@PVA) as the control group. The swelling index and solubility of the sensor array were presented in **Figures 6-4**. Nile red was selected as a model dye since it has a characteristic absorbance peak at 580 nm at pH 6.3, which is in the working range of the sensor array. UiO-66-OH/PVA showed a significantly higher swelling index (24%) than the PVA film. Previous studies reported PVA showed a strong pH-dependent swelling behavior, having a swelling ratio index in the range of 5%-15% when pH was in the range between 4 to 7 at room temperature. After being mixed with UiO-66-OH NPs,

the water retention capability was slightly increased due to the hydroxyl groups on MOF NPs. Considering the robust water stability of UiO-66 NPs, the MOF MMM intelligent packaging film had a practical acceptable swelling ratio(Pounds et al., 2021). Furthermore, the solubility of the different systems was also tested. For UiO-66-OH/PVA system, the supernatant had no visible color and negligible absorbance at 580 nm, whereas NR@PVA showed red supernatant. Furthermore, with the increased immersion time, the absorbance increased from 0.7 to 2.1. These results indicated that MOF NPs prevented Nile red from leaking out of the MMM whereas weak Van der Waals force between PVA and Nile red could not prevent the leakage, which may ensure the package safety of the sensor array system.

6.4.3Validation and sensitivity of MOF-MMM in standard conditions

Protein was microbially decomposed into peptides and amino acids and further broken down into low-grade amines and ammonia, which may be used as vital indicators in meat and seafood safety. To test and optimize the sensing performance of MOF-MMM, dye@UiO-66-OH/PVA, dye@UiO-66/PVA, and dye@PVA were exposed to methylamine (MA) gas. The sensor array exhibited an obvious pattern change over the test time with an increasing concentration of MA (**Figure 6-5a**). Dye@UiO-66-OH/PVA and dye@UiO-66/PVA exhibited visible color differences with increased MA concentration. These results strongly suggested that our approach hold promises to rapidly identify and quantify VOCs from foods. To quantitatively describe the sensor array response, Euclidean distance (ED) of the circular region of interest (CROI) RGB value was measured under exposure to different MA concentrations and different times (Figure 6.6). The RGB values of the sensor array were extracted by an image recognition and color extraction system based on the Hough circle transform algorithm. In brief, to segment, the CROI from sensor array image, circle candidate area was produced by “voting” in the Hough

parameter space and afterword sorting global maximal from an accumulator matrix. The circumference of the segmented CROI was shown in **Figure 6-5b**. Then, 50 pixels were randomly selected from each CROI and labeled with the name of the dye, and each variance of color components of pixel was computed. During the different exposure times, the time dependence of pattern change was attributed to the increase of the reaction process, as our set-up allows VOCs temporal accumulated in the storage environment. All the MOF-involved sensor arrays showed a significantly higher response than dye@PVA, which was attributed to the 3D porous structure of UiO-66 NPs, which facilitated the gas transfer and provided more reaction sites (see the different scale of the y-axis). Moreover, as a result of DFT calculation, after being modified with a hydroxy group, dye@UiO-66-OH/PVA sensor array showed a higher sensitivity than that of bared UiO-66, which was attributed to the low binding energy between UiO-66-OH and MA. Besides, the limit of detection (LOD) of sensor arrays was calculated. The dye@UiO-66-OH/PVA showed the lowest LOD (80 ppm) and shortest equilibrium time (420 s), which was consistent with the previous results(P. Ma, Zhang, Xu, et al., 2021). Based on the performance of the different sensor arrays, dye@UiO-66-OH/PVA was chosen for all subsequent experiments.

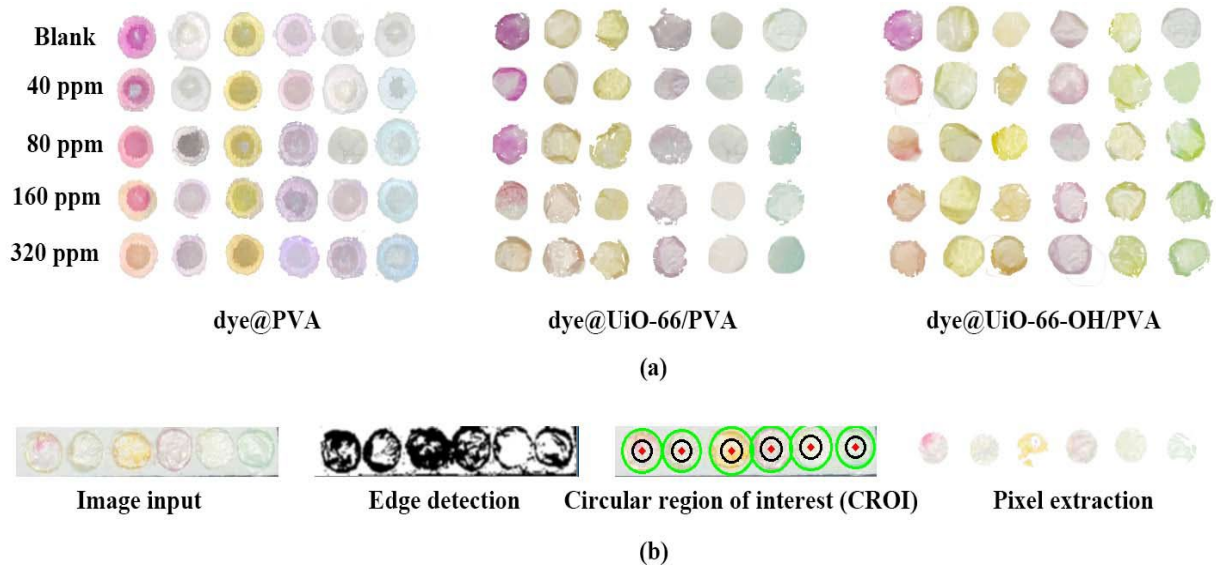


Figure 6-36 *(a) Photoed images of color changes of dye@UiO-66-OH/PVA sensor array exposed to methylamine gas as gas concentration increased from 40 ppm to 320 ppm. (b) Schematic of Hough transform ROI extraction processing.*

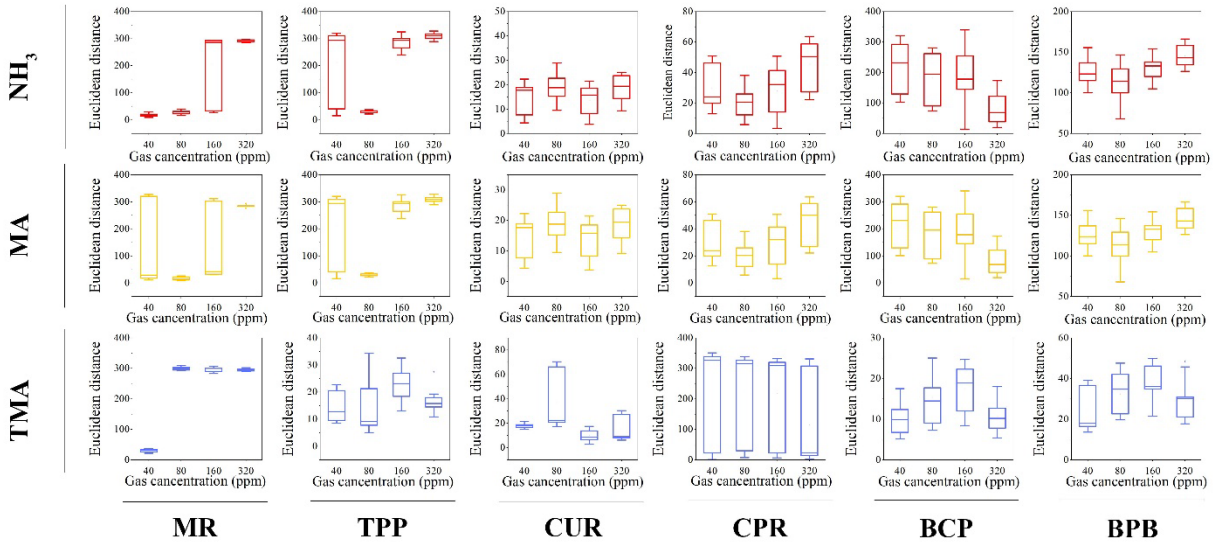


Figure 6-37 *Boxplot of the ED distribution of different dyes based on UiO-66-OH/PVA MOF-MMM for NH_3, MA, TMA at different gas concentrations (from 40 to 320 ppm, n = 10).*

6.4.4 Deep learning-enabled pattern recognition using DCNN

We used the newly designed sensor array to detect the freshness of chicken to create a prototype. The chicken was kept frozen in lunch boxes at 4°C. An iPhone 11 max was used to capture images of the sensor arrays at various time intervals. According to a prior study, chicken

with TVB-N value less than 28 mg/100g was considered fresh, whereas chicken with TVB-N value higher than 28 mg/100g was declared spoiled and inedible(Bekhit, Holman, Giteru, & Hopkins, 2021). The TVB-N value of the chicken was examined using the Conway method to classify the sensor array into these two freshness classes. The photos were then classified as fresh or spoiled based on this criterion. **Figure 6-7a** depicts the general pattern of variations in TVB-N content throughout a 168-hour cold storage period.

Without contacting the chicken samples, the dye@UiO-66-OH/PVA sensor arrays were affixed to the bottom of lunch boxes. Every 24 h, the lunch box was moved out from the refrigerator and the cap was taken off before taking pictures in the photo box. To imitate the use of natural light for taking photos, the lighting conditions in the photo box were programmed in advance. The temperature of the light source and brightness were automatically changed after the sample was placed in the photo box. Subsequently, a total of 6419 photos of chicken breast with sensor array was collected, yielding in a dataset for machine learning chicken freshness evaluation. The dataset was initially randomly split into a training subset and a testing subset with a ratio of 7:3, resulting in 4492 pictures for model training and 1927 images for testing, as described in the method section (**Figure 6-7b**). The input, multiple convolutions, full connection, and output layers of a Fresh/Spolied image classification network with distinct DCNN backbones were built. The trained DCNN extracted features from images that contained sensor arrays and chicken, afterwards, images were classified into one of the two classes, annotated 0 (fresh) and spoiled 1(spoiled) (**Figure 6-7c**).

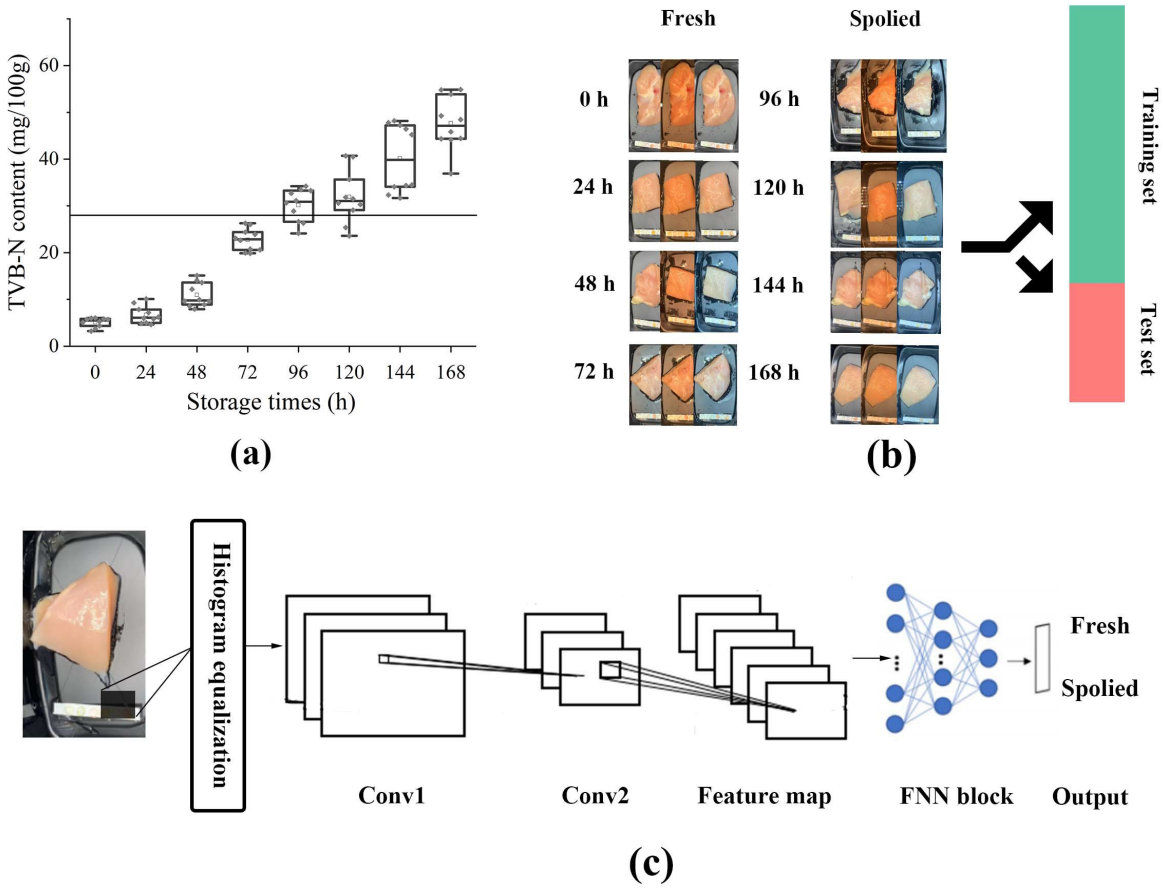


Figure 6-38 *(a) The pattern change of TVB-N content in chicken breast sample during cold storage. (b) The chicken breast sample with sensor array images database structure. The database contained 4492 images for model training and 1927 images for testing labeled with reference TVB-N result; (c) The DCNN models were used for chicken breast freshness classification.*

The ED value approach was used as a baseline to illustrate the superiority of accurate deep learning models. Following our previous research, we randomly selected 50 sensor array images from fresh and spoiled classes to assess the prediction accuracy of ED values(P. Ma, Zhang, Xu, et al., 2021). In the end, the ED values achieved an overall prediction accuracy of 64.27%. When considering that this is a simple binary classification task (Fresh/Spoiled), this accuracy means that the method does not accomplish the task of freshness estimation. Thereafter,

four cutting-edge DCNN models, VGG, Inception V3, WISsR, and Resnet-152 were applied for comparison. WISeR50 achieved the highest accuracy for freshness classification, up to 98.95%, which was 34.68 % higher than the ED values method. It is worth noting that this result was obtained while taking into consideration the extreme light conditions that we performed to interfere with the sample photographing. The accuracies of the other three deep learning algorithms are 97.28%, 97.46%, and 92.2%, for VGG16, ResNet50, and Inception V3, respectively, which are all significantly higher than the baseline (**Table 6-4**).

Table 6- 1 7 *The accuracy comparison results between the ED value method and four state-of-art DCNN models*

Model	Accuracy
Euclidean distance	**64.27%**
VGG16	**97.28%**
ResNet50	**97.46%**
WISeR50	**98.95%**
Inception V3	**92.20%**

To compare more precisely the performance of the different models, we plotted confusion matrices (**Figure 6-8**). For the four neural network models, the vast majority of the data was distributed within the diagonal lattice, which further corroborated the accuracy of the models calculated in the previous section. For three of these models (VGG16, WISeR50, and Inception V3, respectively), there were fewer false positives than false negatives. Considering the potential future application of the freshness sensor system to ensure food safety, false negatives are generally considered to be of greater concern. Here, it is found that the vast majority of trained neural nets tended to be more conservative in freshness analysis, thus further

demonstrating their advantages. In the test dataset composed of 1927 photos, only 5 photos of spoiled chicken were classified as fresh by the WISeR50 model, accounting for only 0.26%.

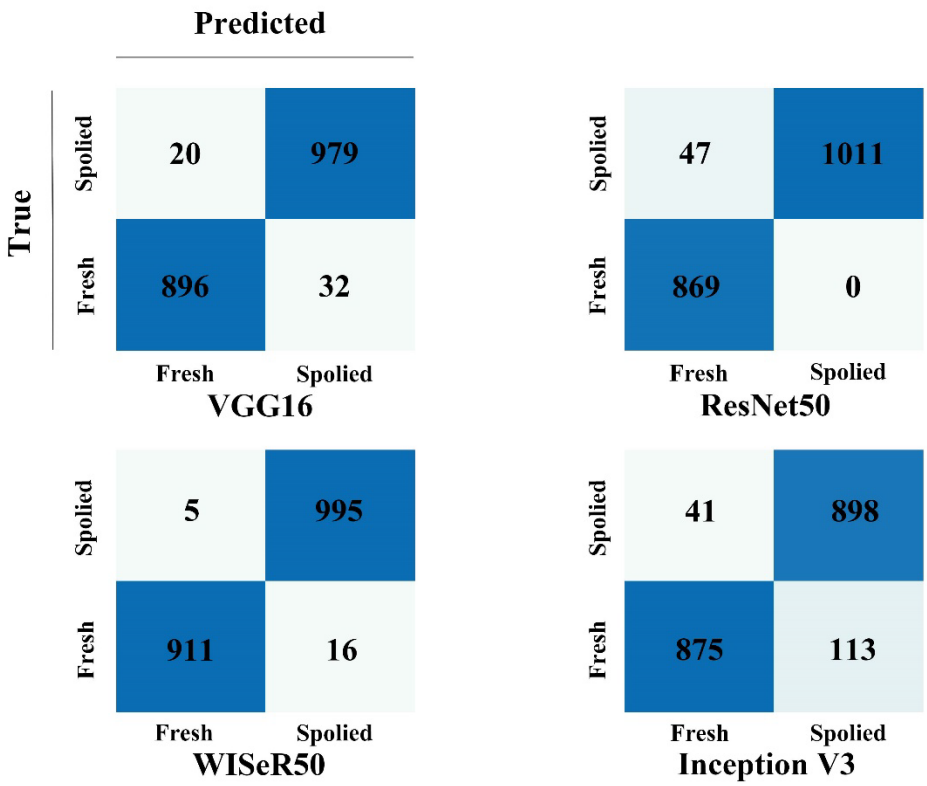


Figure 6-39 *The confusion matrix of four DCNN models.*

DCNN models might be desirable to use in colorimetric sensor array recognition and classification tasks due to their better accuracy. Furthermore, there are a plethora of alternative sensor arrays that might benefit from the DCNN model while also promising to attain improved accuracy. The fundamental benefit of this technique is that it maintains a high level of picture classification accuracy while being simple to set up an image database. Meanwhile, the system can be applied to identify the freshness of other foods in the future by changing the image data set.

Summary and Future Perspectives

In the past decades, many studies have proved the exciting potential of MOFs for their applications in the field of food safety. Though progress has been made, it is expected that MOFs will step into a new age and play more roles in the food industry:

First, the high cost and limited batch production ability of MOFs in the industry is still a challenge of application in the food area. Therefore, more attention needs to be directed toward achieving fast and efficient MOF synthesis. Second, the toxicity of MOF, especially a series of novel, sophisticated synthesis MOFs with modification, needs to be systematically evaluated before applying them in the food industry. Apart from immediate toxicity effects, metabolic pathways and residues' toxicity are also required for the evaluation of MOFs as food additives. Third, MOF-based materials have exhibited exciting potentials in food analysis, including improvement of sample preparation, drug delivery, preparation of sensing devices, and enhancement of detection signals. But, their functional properties could be further improved through chemical modification or by combining recognition elements, including aptamers, antibodies, and enzymes, especially for analysis of small molecules.

Besides MOF, the colorimetric sensor array technology is also a novel detection method in the food scope and needs to be explored. In the past years, various types of sensor array systems have been developed, which could provide information about food processing, quality control, chemical composition, and contamination of foods, ensuring compliance with food and trade laws. Up to now,

the colorimetric sensor array technique faces a great challenge brought by food sample diversity and volatile component complexity, which limits accurate quantification. The characteristics, including repeatability, sensitivity, selectivity, portability, security, precision, accuracy, and method validation, must be carefully and thoroughly addressed to make the colorimetric sensor array approach more analytically valuable. In addition to MOF materials, zeolite, hydrophilic silica aerogel, and other materials also have the potential to improve the sensor array. Colorimetric sensor arrays can only be turned from research platforms to industrial devices after these issues are resolved.

Artificial intelligence, especially neural network technology, has become a consensus in the food industry, government, academia, and other industry, that it holds great promise in the food sector. There is currently a huge divide between industry and academia for food-related neural network systems. In academia, it tends to be mostly independent concept-proof training models, while neural network implementation for practical applications often relies on a huge accumulation of data volume, which needs the help of industry. There is a lack of an effective integrated data management system that can lift the concern of privacy concerns, considerations related to regulatory frameworks, interoperability, and compatibility with existing systems. In addition to this, food data are often multi-sourced and complex. To produce a more comprehensive assessment of food, the combination of deep learning and multisource data fusion including images, spectra, taste, etc, would be considered for food application in the future.

Bibliography

Araiza-Calahorra, A., Akhtar, M., & Sarkar, A. (2018). Recent advances in emulsion-based delivery approaches for curcumin: From encapsulation to bioaccessibility. *Trends in Food Science & Technology*, *71*, 155-169.

Bai, L., Huan, S., Xiang, W., & Rojas, O. J. (2018). Pickering emulsions by combining cellulose nanofibrils and nanocrystals: Phase behavior and depletion stabilization. *Green chemistry*, *20*(7), 1571-1582.

Bai, Y., Dou, Y., Xie, L., Rutledge, W., Li, J., & Zhou, H. (2016). Zr-based metal-organic frameworks: design, synthesis, structure, and applications [Review]. *Chemical Society Reviews*, *45*(8), 2327-2367. https://doi.org/10.1039/c5cs00837a

Bernini, M., Fairen-Jimenez, D., Pasinetti, M., Ramirez-Pastor, A., & Snurr, R. (2014). Screening of bio-compatible metal-organic frameworks as potential drug carriers using Monte Carlo simulations [Article]. *Journal of Materials Chemistry B*, *2*(7), 766-774. https://doi.org/10.1039/c3tb21328e

Blijdenstein, T. B., Veerman, C., & van der Linden, E. (2004). Depletion− flocculation in oil-in-water emulsions using fibrillar protein assemblies. *Langmuir*, *20*(12), 4881-4884.

Bobbitt, N. S., Mendonca, M. L., Howarth, A. J., Islamoglu, T., Hupp, J. T., Farha, O. K., & Snurr, R. Q. (2017). Metal–organic frameworks for the removal of toxic industrial chemicals and chemical warfare agents. *Chemical Society Reviews*, *46*(11), 3357-3385.

Boire, A., Renard, D., Bouchoux, A., Pezennec, S., Croguennec, T., Lechevalier, V., . . . McClements, D. (2019). Soft-Matter Approaches for Controlling Food Protein Interactions and Assembly [Review|Book Chapter]. *Annual Review of Food Science and Technology, Vol 10*, *10*, 521-539. https://doi.org/10.1146/annurev-food-032818-121907

Bossard, L., Guillaumin, M., & Van Gool, L. (2014). Food-101–mining discriminative components with random forests. European conference on computer vision,

Cai, D., Thijssen, J. H., & Clegg, P. S. (2014). Making non-aqueous high internal phase pickering emulsions: influence of added polymer and selective drying. *ACS applied materials & interfaces*, *6*(12), 9214-9219.

Cavka, J., Jakobsen, S., Olsbye, U., Guillou, N., Lamberti, C., Bordiga, S., & Lillerud, K. (2008). A new zirconium inorganic building brick forming metal organic frameworks with exceptional stability [Article]. *Journal of the American Chemical Society*, *130*(42), 13850-13851. https://doi.org/10.1021/ja8057953

Chen, H.-C., Chen, J.-H., Chang, C., & Shieh, C.-J. (2011). Optimization of ultrasound-accelerated synthesis of enzymatic caffeic acid phenethyl ester by response surface methodology. *Ultrasonics sonochemistry*, *18*(1), 455-459.

Chen, Q., He, Q., Lv, M., Xu, Y., Yang, H., Liu, X., & Wei, F. (2015). Selective adsorption of cationic dyes by UiO-66-NH2 [Article]. *Applied Surface Science*, *327*, 77-85. https://doi.org/10.1016/j.apsusc.2014.11.103

Chen, S., Li, Q., McClements, D. J., Han, Y., Dai, L., Mao, L., & Gao, Y. (2020). Co-delivery of curcumin and piperine in zein-carrageenan core-shell nanoparticles: Formation, structure, stability and in vitro gastrointestinal digestion. *Food Hydrocolloids*, *99*, 105334.

Cheng, W., Tang, X., Zhang, Y., Wu, D., & Yang, W. (2021). Applications of metal-organic framework (MOF)-based sensors for food safety: Enhancing mechanisms and recent advances. *Trends in Food Science & Technology*, *112*, 268-282.

Ciocca, G., Napoletano, P., & Schettini, R. (2018). CNN-based features for retrieval and classification of food images. *Computer Vision and Image Understanding*, *176*, 70-77.

Cunha, D., Ben Yahia, M., Hall, S., Miller, S., Chevreau, H., Elkaim, E., . . . Serre, C. (2013). Rationale of Drug Encapsulation and Release from Biocompatible Porous Metal-Organic Frameworks [Article]. *Chemistry of Materials*, *25*(14), 2767-2776. https://doi.org/10.1021/cm400798p

Dechnik, J., Gascon, J., Doonan, C. J., Janiak, C., & Sumby, C. J. (2017). Mixed-matrix membranes. *Angewandte Chemie International Edition*, *56*(32), 9292-9310.

DeCoste, J., Peterson, G., Schindler, B., Killops, K., Browe, M., & Mahle, J. (2013). The effect of water adsorption on the structure of the carboxylate containing metal-organic frameworks Cu-BTC, Mg-MOF-74, and UiO-66 [Article]. *Journal of Materials Chemistry a*, *1*(38), 11922-11932. https://doi.org/10.1039/c3ta12497e

DeCoste, J. B., Demasky, T. J., Katz, M. J., Farha, O. K., & Hupp, J. T. (2015). A UiO-66 analogue with uncoordinated carboxylic acids for the broad-spectrum removal of toxic chemicals. *New Journal of Chemistry*, *39*(4), 2396-2399.

Deng, X., Cao, S., & Horn, A. L. (2021). Emerging Applications of Machine Learning in Food Safety. *Annual Review of Food Science and Technology*, *12*, 513-538.

Dong, Z., Sun, Y., Chu, J., Zhang, X., & Deng, H. (2017). Multivariate metal–organic frameworks for dialing-in the binding and programming the release of drug molecules. *Journal of the American Chemical Society*, *139*(40), 14209-14216.

Dubbeldam, D., Calero, S., Ellis, D., & Snurr, R. (2016). RASPA: molecular simulation software for adsorption and diffusion in flexible nanoporous materials [Article]. *Molecular Simulation*, *42*(2), 81-101. https://doi.org/10.1080/08927022.2015.1010082

Dubbeldam, D., Calero, S., & Vlugt, T. (2018). iRASPA: GPU-accelerated visualization software for materials scientists [Review]. *Molecular Simulation*, *44*(8), 653-676. https://doi.org/10.1080/08927022.2018.1426855

Düren, T., Bae, Y.-S., & Snurr, R. Q. (2009). Using molecular simulation to characterise metal–organic frameworks for adsorption applications. *Chemical Society Reviews*, *38*(5), 1237-1247.

Ege, T., & Yanai, K. (2018). Image-based food calorie estimation using recipe information. *IEICE TRANSACTIONS on Information and Systems*, *101*(5), 1333-1341.

Fang, R., Dhakshinamoorthy, A., Li, Y., & Garcia, H. (2020). Metal organic frameworks for biomass conversion. *Chemical Society Reviews*, *49*(11), 3638-3687.

Fu, F., Wu, Y., Zhu, J., Wen, S., Shen, M., & Shi, X. (2014). Multifunctional Lactobionic Acid-Modified Dendrimers for Targeted Drug Delivery to Liver Cancer Cells: Investigating the Role Played by PEG Spacer [Article]. *Acs Applied Materials & Interfaces*, *6*(18), 16416-16425. https://doi.org/10.1021/am504849x

Fu, Q., Wen, L., Zhang, L., Chen, X., Pun, D., Ahmed, A., . . . Zhang, H. (2017). Preparation of ice-templated MOF–polymer composite monoliths and their application for wastewater treatment with high capacity and easy recycling. *ACS applied materials & interfaces*, *9*(39), 33979-33988.

Furukawa, H., Ko, N., Go, Y. B., Aratani, N., Choi, S. B., Choi, E., . . . Kim, J. (2010). Ultrahigh porosity in metal-organic frameworks. *Science*, *329*(5990), 424-428.

Férey, G. (2008). Hybrid porous solids: past, present, future. *Chemical Society Reviews*, *37*(1), 191-214.

Gandara-Loe, J., Ortuño-Lizarán, I., Fernández-Sanchez, L., Alió, J. L., Cuenca, N., Vega-Estrada, A., & Silvestre-Albero, J. (2018). Metal–organic frameworks as drug delivery platforms for ocular therapeutics. *ACS applied materials & interfaces*, *11*(2), 1924-1931.

Gangu, K. K., Maddila, S., Mukkamala, S. B., & Jonnalagadda, S. B. (2016). A review on contemporary Metal–Organic Framework materials. *Inorganica Chimica Acta*, *446*, 61-74.

Gao, P. F., Zheng, L. L., Liang, L. J., Yang, X. X., Li, Y. F., & Huang, C. Z. (2013). A new type of pH-responsive coordination polymer sphere as a vehicle for targeted anticancer drug delivery and sustained release. *Journal of Materials Chemistry B*, *1*(25), 3202-3208.

Ghalei, B., Sakurai, K., Kinoshita, Y., Wakimoto, K., Isfahani, A. P., Song, Q., . . . Kusuda, H. (2017). Enhanced selectivity in mixed matrix membranes for CO 2 capture through efficient dispersion of amine-functionalized MOF nanoparticles. *Nature Energy*, *2*(7), 1-9.

Ghani, M., Picó, M. F. F., Salehinia, S., Cabello, C. P., Maya, F., Berlier, G., . . . Palomino, G. T. (2017). Metal-organic framework mixed-matrix disks: versatile supports for automated solid-phase extraction prior to chromatographic separation. *Journal of Chromatography A*, *1488*, 1-9.

Giannakoudakis, D. A., & Bandosz, T. J. (2019). Defectous UiO-66 MOF nanocomposites as reactive media of superior protection against toxic vapors. *ACS applied materials & interfaces*, *12*(13), 14678-14689.

Gomez-Gualdron, D., Moghadam, P., Hupp, J., Farha, O., & Snurr, R. (2016). Application of Consistency Criteria To Calculate BET Areas of Micro- And Mesoporous Metal-Organic Frameworks [Article]. *Journal of the American Chemical Society*, *138*(1), 215-224. https://doi.org/10.1021/jacs.5b10266

Grimmer, N., Coville, N., de Koning, C., Smith, J., & Cook, L. (2000). Zirconium bis-indenyl compounds. Synthesis and X-ray crystallography study of 1-and 2-substituted bis(R-indenyl)zirconium dichloride metallocenes [Article]. *Journal of Organometallic Chemistry*, *616*(1-2), 112-127. https://doi.org/10.1016/S0022-328X(00)00570-2

Guo, L., Wang, T., Wu, Z., Wang, J., Wang, M., Cui, Z., . . . Chen, X. (2020). Portable Food-Freshness Prediction Platform Based on Colorimetric Barcode Combinatorics and Deep Convolutional Neural Networks. *Advanced Materials*, *32*(45), 2004805.

Gurkov, T., Marinova, K., Zdravkov, A., Oleksiak, C., & Campbell, B. (1998). Gradual disintegration of protein lumps contained in thin emulsion films: Role of the surface diffusion. *Trends in Colloid and Interface Science XII*, 263-268.

Harman, G. E., & Uphoff, N. (2019). Symbiotic root-endophytic soil microbes improve crop productivity and provide environmental benefits. *Scientifica*, *2019*.

Hassoun, M. H. (1995). *Fundamentals of artificial neural networks*. MIT press.

He, C., Liu, D., & Lin, W. (2015). Nanomedicine Applications of Hybrid Nanomaterials Built from Metal-Ligand Coordination Bonds: Nanoscale Metal-Organic Frameworks and Nanoscale Coordination Polymers [Review]. *Chemical Reviews*, *115*(19), 11079-11108. https://doi.org/10.1021/acs.chemrev.5b00125

He, Q., Shahabi, H., Shirzadi, A., Li, S., Chen, W., Wang, N., . . . Chen, Y. (2019). Landslide spatial modelling using novel bivariate statistical based Naïve Bayes, RBF Classifier, and RBF Network machine learning algorithms. *Science of the total environment*, *663*, 1-15.

He, Q., & Shi, J. (2011). Mesoporous silica nanoparticle based nano drug delivery systems: synthesis, controlled drug release and delivery, pharmacokinetics and biocompatibility [Article]. *Journal of Materials Chemistry*, *21*(16), 5845-5855. https://doi.org/10.1039/c0jm03851b

Horcajada, P., Chalati, T., Serre, C., Gillet, B., Sebrie, C., Baati, T., . . . Gref, R. (2010). Porous metal-organic-framework nanoscale carriers as a potential platform for drug delivery and imaging [Article]. *Nature Materials*, *9*(2), 172-178. https://doi.org/10.1038/NMAT2608

Horcajada, P., Gref, R., Baati, T., Allan, P., Maurin, G., Couvreur, P., . . . Serre, C. (2012). Metal-Organic Frameworks in Biomedicine [Review]. *Chemical Reviews*, *112*(2), 1232-1268. https://doi.org/10.1021/cr200256v

Horcajada, P., Serre, C., Maurin, G., Ramsahye, N. A., Balas, F., Vallet-Regi, M., . . . Férey, G. (2008). Flexible porous metal-organic frameworks for a controlled drug delivery. *Journal of the American Chemical Society*, *130*(21), 6774-6780.

Horcajada, P., Serre, C., Vallet-Regí, M., Sebban, M., Taulelle, F., & Férey, G. (2006). Metal–organic frameworks as efficient materials for drug delivery. *Angewandte chemie*, *118*(36), 6120-6124.

Howarth, A. J., Liu, Y., Li, P., Li, Z., Wang, T. C., Hupp, J. T., & Farha, O. K. (2016). Chemical, thermal and mechanical stabilities of metal–organic frameworks. *Nature Reviews Materials*, *1*(3), 1-15.

Ikem, V., Menner, A., & Bismarck, A. (2008). High Internal Phase Emulsions Stabilized Solely by Functionalized Silica Particles [Article]. *Angewandte Chemie-International Edition*, *47*(43), 8277-8279. https://doi.org/10.1002/anie.200802244

Imam, N., & Cleland, T. A. (2020). Rapid online learning and robust recall in a neuromorphic olfactory circuit. *Nature Machine Intelligence*, *2*(3), 181-191.

Imanifard, S., Zarrabi, A., Zarepour, A., Jafari, M., Khosravi, A., & Razmjou, A. (2017). Nanoengineered Thermoresponsive Magnetic Nanoparticles for Drug Controlled Release [Article]. *Macromolecular Chemistry and Physics*, *218*(23), Article ARTN 1700350. https://doi.org/10.1002/macp.201700350

Janzen, M. C., Ponder, J. B., Bailey, D. P., Ingison, C. K., & Suslick, K. S. (2006). Colorimetric sensor arrays for volatile organic compounds. *Analytical chemistry*, *78*(11), 3591-3600.

Jarai, B. M., Stillman, Z., Attia, L., Decker, G. E., Bloch, E. D., & Fromen, C. A. (2020). Evaluating UiO-66 Metal–Organic Framework Nanoparticles as Acid-Sensitive Carriers for Pulmonary Drug Delivery Applications. *ACS applied materials & interfaces*, *12*(35), 38989-39004.

Ji, Z., Wang, H., Canossa, S., Wuttke, S., & Yaghi, O. M. (2020). Pore chemistry of metal–organic frameworks. *Advanced Functional Materials*, *30*(41), 2000238.

Joachims, T. (1998). *Making large-scale SVM learning practical*.

Johansson, L., Singh, T., Leong, T., Mawson, R., McArthur, S., Manasseh, R., & Juliano, P. (2016). Cavitation and non-cavitation regime for large-scale ultrasonic standing wave particle separation systems–In situ gentle cavitation threshold determination and free radical related oxidation. *Ultrasonics sonochemistry*, *28*, 346-356.

Kagan, C. R. (2016). At the nexus of food security and safety: opportunities for nanoscience and nanotechnology. In: ACS Publications.

Kalaj, M., Bentz, K. C., Ayala Jr, S., Palomba, J. M., Barcus, K. S., Katayama, Y., & Cohen, S. M. (2020). MOF-polymer hybrid materials: From simple composites to tailored architectures. *Chemical reviews*, *120*(16), 8267-8302.

Katz, M., Brown, Z., Colon, Y., Siu, P., Scheidt, K., Snurr, R., . . . Farha, O. (2013). A facile synthesis of UiO-66, UiO-67 and their derivatives [Article]. *Chemical Communications*, *49*(82), 9449-9451. https://doi.org/10.1039/c3cc46105j

Katz, M. J., Mondloch, J. E., Totten, R. K., Park, J. K., Nguyen, S. T., Farha, O. K., & Hupp, J. T. (2014). Simple and compelling biomimetic metal–organic framework catalyst for the degradation of nerve agent simulants. *Angewandte Chemie*, *126*(2), 507-511.

Kim, K., Kim, S., Ryu, J., Jeon, J., Jang, S., Kim, H., . . . Choi, S. (2017). Processable high internal phase Pickering emulsions using depletion attraction [Article]. *Nature Communications*, *8*, Article ARTN 14305. https://doi.org/10.1038/ncomms14305

Kim, Y.-J., Kim, H.-S., Chon, J.-W., Kim, D.-H., Hyeon, J.-Y., & Seo, K.-H. (2018). New colorimetric aptasensor for rapid on-site detection of Campylobacter jejuni and Campylobacter coli in chicken carcass samples. *Analytica chimica acta*, *1029*, 78-85.

Kittitheeranun, P., Sajomsang, W., Phanpee, S., Treetong, A., Wutikhun, T., Suktham, K., . . . Ruktanonchai, U. (2015). Layer-by-layer engineered nanocapsules of curcumin with improved cell activity [Article]. *International Journal of Pharmaceutics*, *492*(1-2), 92-102. https://doi.org/10.1016/j.ijpharm.2015.06.040

Kuo, C.-J., Wang, D.-C., Chen, T.-T., Chou, Y.-C., Pai, M.-Y., Horng, G.-J., . . . Chen, C.-C. (2019). Improving Defect Inspection Quality of Deep-Learning Network in Dense Beans by Using Hough Circle Transform for Coffee Industry. 2019 IEEE International Conference on Systems, Man and Cybernetics (SMC),

Leong, T., Wooster, T., Kentish, S., & Ashokkumar, M. (2009). Minimising oil droplet size using ultrasonic emulsification. *Ultrasonics sonochemistry*, *16*(6), 721-727.

Leong, T. S., Martin, G. J., & Ashokkumar, M. (2017). Ultrasonic encapsulation–a review. *Ultrasonics sonochemistry*, *35*, 605-614.

Li, J., Wu, Q., Wang, X., Chai, Z., Shi, W., Hou, J., . . . Wang, X. (2017). Heteroaggregation behavior of graphene oxide on Zr-based metal-organic frameworks in aqueous solutions: a combined experimental and theoretical study [Article]. *Journal of Materials Chemistry a*, *5*(38), 20398-20406. https://doi.org/10.1039/c7ta06462d

Libbrecht, M. W., & Noble, W. S. (2015). Machine learning applications in genetics and genomics. *Nature Reviews Genetics*, *16*(6), 321-332.

Likas, A., Vlassis, N., & Verbeek, J. J. (2003). The global k-means clustering algorithm. *Pattern recognition*, *36*(2), 451-461.

Lin, Q., & Buccella, D. (2018). Highly selective, red emitting BODIPY-based fluorescent indicators for intracellular Mg 2+ imaging. *Journal of Materials Chemistry B*, *6*(44), 7247-7256.

Lissant, K. (1966). The geometry of high-internal-phase-ratio emulsions. *Journal of colloid and interface science*, *22*(5), 462-468.

Liu, F., Ma, C., Gao, Y., & McClements, D. (2017). Food-Grade Covalent Complexes and Their Application as Nutraceutical Delivery Systems: A Review [Review]. *Comprehensive Reviews in Food Science and Food Safety*, *16*(1), 76-95. https://doi.org/10.1111/1541-4337.12229

Liu, Y., Liu, J., Chang, M., & Zheng, C. (2012). Theoretical studies of CO2 adsorption mechanism on linkers of metal-organic frameworks [Article]. *Fuel*, *95*(1), 521-527. https://doi.org/10.1016/j.fuel.2011.09.057

Liu, Y., & Peng, X. (2017). Recent advances of supercapacitors based on two-dimensional materials [Article]. *Applied Materials Today*, *8*, 104-115. https://doi.org/10.1016/j.apmt.2017.05.002

Luo, G., Chen, W., Lei, Q., Qiu, W., Liu, Y., Cheng, Y., & Zhang, X. (2016). A Triple-Collaborative Strategy for High-Performance Tumor Therapy by Multifunctional Mesoporous Silica-Coated Gold Nanorods [Article]. *Advanced Functional Materials*, *26*(24), 4339-4350. https://doi.org/10.1002/adfm.201505175

Lv, S., Zhou, H., Bai, L., Rojas, O. J., & McClements, D. J. (2021). Development of food-grade Pickering emulsions stabilized by a mixture of cellulose nanofibrils and nanochitin. *Food Hydrocolloids*, *113*, 106451.
Ma, P., Li, A., Yu, N., Li, Y., Bahadur, R., Wang, Q., & Ahuja, J. K. (2021). Application of machine learning for estimating label nutrients using USDA Global Branded Food Products Database,(BFPD). *Journal of Food Composition and Analysis*, 103857.
Ma, P., Zeng, Q., Tai, K., He, X., Yao, Y., Hong, X., & Yuan, F. (2017). Preparation of curcumin-loaded emulsion using high pressure homogenization: Impact of oil phase and concentration on physicochemical stability [Article]. *Lwt-Food Science and Technology*, *84*, 34-46. https://doi.org/10.1016/j.lwt.2017.04.074
Ma, P., Zeng, Q., Tai, K., He, X., Yao, Y., Hong, X., & Yuan, F. (2018). Development of stable curcumin nanoemulsions: effects of emulsifier type and surfactant-to-oil ratios [Article]. *Journal of Food Science and Technology-Mysore*, *55*(9), 3485-3497. https://doi.org/10.1007/s13197-018-3273-0
Ma, P., Zhang, J., Liu, P., Wang, Q., Zhang, Y., Song, K., . . . Shen, L. (2020). Computer-assisted design for stable and porous metal-organic framework (MOF) as a carrier for curcumin delivery. *LWT*, *120*, 108949.
Mamoshina, P., Vieira, A., Putin, E., & Zhavoronkov, A. (2016). Applications of Deep Learning in Biomedicine [Review]. *Molecular Pharmaceutics*, *13*(5), 1445-1454. https://doi.org/10.1021/acs.molpharmaceut.5b00982
Marefati, A., Bertrand, M., Sjoo, M., Dejmek, P., & Rayner, M. (2017). Storage and digestion stability of encapsulated curcumin in emulsions based on starch granule Pickering stabilization [Article]. *Food Hydrocolloids*, *63*, 309-320. https://doi.org/10.1016/j.foodhyd.2016.08.043
Matsuda, Y., Hoashi, H., & Yanai, K. (2012). Recognition of multiple-food images by detecting candidate regions. 2012 IEEE International Conference on Multimedia and Expo,
McClements, D. (2018). Enhanced delivery of lipophilic bioactives using emulsions: a review of major factors affecting vitamin, nutraceutical, and lipid bioaccessibility [Review]. *Food & Function*, *9*(1), 22-41. https://doi.org/10.1039/c7fo01515a
McClements, D., & Li, Y. (2010). Structured emulsion-based delivery systems: Controlling the digestion and release of lipophilic food components [Article]. *Advances in Colloid and Interface Science*, *159*(2), 213-228. https://doi.org/10.1016/j.cis.2010.06.010
McClements, D. J., & Decker, E. A. (2000). Lipid oxidation in oil-in-water emulsions: Impact of molecular environment on chemical reactions in heterogeneous food systems. *Journal of food science*, *65*(8), 1270-1282.
Mei, L., Teng, Z., Zhu, G., Liu, Y., Zhang, F., Zhang, J., . . . Wang, Q. (2017). Silver Nanocluster-Embedded Zein Films as Antimicrobial Coating Materials for Food Packaging [Article]. *Acs Applied Materials & Interfaces*, *9*(40), 35297-35304. https://doi.org/10.1021/acsami.7b08152
Menner, A., Ikem, V., Salgueiro, M., Shaffer, M., & Bismarck, A. (2007). High internal phase emulsion templates solely stabilised by functionalised titania

nanoparticles [Article]. *Chemical Communications*(41), 4274-4276. https://doi.org/10.1039/b708935j

Meroni, D., Gasparini, C., Di Michele, A., Ardizzone, S., & Bianchi, C. L. (2020). Ultrasound-assisted synthesis of ZnO photocatalysts for gas phase pollutant remediation: role of the synthetic parameters and of promotion with WO3. *Ultrasonics Sonochemistry*, 105119.

Miklitz, M., & Jelfs, K. (2018). pywindow: Automated Structural Analysis of Molecular Pores [Article]. *Journal of Chemical Information and Modeling*, *58*(12), 2387-2391. https://doi.org/10.1021/acs.jcim.8b00490

Moghadam, P., Li, A., Wiggin, S., Tao, A., Maloney, A., Wood, P., . . . Fairen-Jimenez, D. (2017). Development of a Cambridge Structural Database Subset: A Collection of Metal-Organic Frameworks for Past, Present, and Future [Article]. *Chemistry of Materials*, *29*(7), 2618-2625. https://doi.org/10.1021/acs.chemmater.7b00441

Muller, M., Zhang, X., Wang, Y., & Fischer, R. (2009). Nanometer-sized titania hosted inside MOF-5 [Article]. *Chemical Communications*(1), 119-121. https://doi.org/10.1039/b814241f

Murray, B. S. (2019). Pickering emulsions for food and drinks. *Current Opinion in Food Science*, *27*, 57-63.

Nagata, S., Kokado, K., & Sada, K. (2015). Metal–organic framework tethering PNIPAM for ON–OFF controlled release in solution. *Chemical Communications*, *51*(41), 8614-8617.

Oh, S., Wu, Y., Tran, D., Lee, I., Lei, Y., & Liu, D. (2016). Influences of cation and anion substitutions on oxidative coupling of methane over hydroxyapatite catalysts [Article]. *Fuel*, *167*, 208-217. https://doi.org/10.1016/j.fuel.2015.11.058

Orellana-Tavra, C., Baxter, E., Tian, T., Bennett, T., Slater, N., Cheetham, A., & Fairen-Jimenez, D. (2015). Amorphous metal-organic frameworks for drug delivery [Article]. *Chemical Communications*, *51*(73), 13878-13881. https://doi.org/10.1039/c5cc05237h

O'Keeffe, M., & Yaghi, O. M. (2012). Deconstructing the crystal structures of metal–organic frameworks and related materials into their underlying nets. *Chemical reviews*, *112*(2), 675-702.

Park, D.-H., Heo, J.-M., Jeong, W., Yoo, Y. H., Park, B. J., & Kim, J.-M. (2018). Smartphone-based VOC sensor using colorimetric polydiacetylenes. *ACS applied materials & interfaces*, *10*(5), 5014-5021.

Peng, J., Simon, J. R., Venema, P., & Van Der Linden, E. (2016). Protein fibrils induce emulsion stabilization. *Langmuir*, *32*(9), 2164-2174.

Ploegmakers, J., Japip, S., & Nijmeijer, K. (2013). Mixed matrix membranes containing MOFs for ethylene/ethane separation Part A: Membrane preparation and characterization [Article]. *Journal of Membrane Science*, *428*, 445-453. https://doi.org/10.1016/j.memsci.2012.11.014

Qin, J., Chao, K., Kim, M. S., Lu, R., & Burks, T. F. (2013). Hyperspectral and multispectral imaging for evaluating food safety and quality. *Journal of Food Engineering*, *118*(2), 157-171.

Qiu, C., McClements, D. J., Jin, Z., Qin, Y., Hu, Y., Xu, X., & Wang, J. (2020). Resveratrol-loaded core-shell nanostructured delivery systems: Cyclodextrin-based metal-organic nanocapsules prepared by ionic gelation. *Food Chemistry*, *317*, 126328.

Qiu, S., Xue, M., & Zhu, G. (2014). Metal–organic framework membranes: from synthesis to separation application. *Chemical Society Reviews*, *43*(16), 6116-6140.

Quinlan, J. R. (1986). Induction of decision trees. *Machine learning*, *1*(1), 81-106.

RAPPE, A., CASEWIT, C., COLWELL, K., GODDARD, W., & SKIFF, W. (1992). UFF, A FULL PERIODIC-TABLE FORCE-FIELD FOR MOLECULAR MECHANICS AND MOLECULAR-DYNAMICS SIMULATIONS [Article]. *Journal of the American Chemical Society*, *114*(25), 10024-10035. https://doi.org/10.1021/ja00051a040

Ren, J., Dyosiba, X., Musyoka, N. M., Langmi, H. W., Mathe, M., & Liao, S. (2017). Review on the current practices and efforts towards pilot-scale production of metal-organic frameworks (MOFs). *Coordination Chemistry Reviews*, *352*, 187-219.

Roy, D., Brooks, W. L., & Sumerlin, B. S. (2013). New directions in thermoresponsive polymers. *Chemical Society Reviews*, *42*(17), 7214-7243.

Safaei, M., Foroughi, M. M., Ebrahimpoor, N., Jahani, S., Omidi, A., & Khatami, M. (2019). A review on metal-organic frameworks: Synthesis and applications. *TrAC Trends in Analytical Chemistry*, *118*, 401-425.

Sarkar, A., & Dickinson, E. (2020). Sustainable food-grade Pickering emulsions stabilized by plant-based particles. *Current Opinion in Colloid & Interface Science*.

Schaate, A., Roy, P., Godt, A., Lippke, J., Waltz, F., Wiebcke, M., & Behrens, P. (2011). Modulated synthesis of Zr-based metal–organic frameworks: from nano to single crystals. *Chemistry–A European Journal*, *17*(24), 6643-6651.

Shearer, G., Chavan, S., Ethiraj, J., Vitillo, J., Svelle, S., Olsbye, U., . . . Lillerud, K. (2014). Tuned to Perfection: Ironing Out the Defects in Metal-Organic Framework UiO-66 [Article]. *Chemistry of Materials*, *26*(14), 4068-4071. https://doi.org/10.1021/cm501859p

Shen, M., Forghani, F., Kong, X., Liu, D., Ye, X., Chen, S., & Ding, T. Antibacterial applications of metal–organic frameworks and their composites. *Comprehensive Reviews in Food Science and Food Safety*.

Shi, L., Chen, H., Jiang, M., Wang, L., Wu, X., Huang, L., & Liu, C. (2019). CPGAVAS2, an integrated plastome sequence annotator and analyzer. *Nucleic acids research*, *47*(W1), W65-W73.

Smaldone, R., Forgan, R., Furukawa, H., Gassensmith, J., Slawin, A., Yaghi, O., & Stoddart, J. (2010). Metal-Organic Frameworks from Edible Natural Products [Article]. *Angewandte Chemie-International Edition*, *49*(46), 8630-8634. https://doi.org/10.1002/anie.201002343

Stock, N., & Biswas, S. (2012). Synthesis of metal-organic frameworks (MOFs): routes to various MOF topologies, morphologies, and composites. *Chemical reviews*, *112*(2), 933-969.

Su, F., Jia, Q., Li, Z., Wang, M., He, L., Peng, D., . . . Fang, S. (2019). Aptamer-templated silver nanoclusters embedded in zirconium metal–organic framework for targeted antitumor drug delivery. *Microporous and mesoporous materials*, *275*, 152-162.

Su, H., Sun, F., Jia, J., He, H., Wang, A., & Zhu, G. (2015). A highly porous medical metal-organic framework constructed from bioactive curcumin [Article]. *Chemical Communications*, *51*(26), 5774-5777. https://doi.org/10.1039/c4cc10159f

Sui, X., Bi, S., Qi, B., Wang, Z., Zhang, M., Li, Y., & Jiang, L. (2017). Impact of ultrasonic treatment on an emulsion system stabilized with soybean protein isolate and lecithin: Its emulsifying property and emulsion stability. *Food hydrocolloids*, *63*, 727-734.

Sun, C., Liu, F., Yang, J., Yang, W., Yuan, F., & Gao, Y. (2015). Physical, structural, thermal and morphological characteristics of zeinquercetagetin composite colloidal nanoparticles [Article]. *Industrial Crops and Products*, *77*, 476-483. https://doi.org/10.1016/j.indcrop.2015.09.028

Sun, C., Xu, C., Mao, L., Wang, D., Yang, J., & Gao, Y. (2017). Preparation, characterization and stability of curcumin-loaded zein-shellac composite colloidal particles [Article]. *Food Chemistry*, *228*, 656-667. https://doi.org/10.1016/j.foodchem.2017.02.001

Tai, S., Zhang, W., Zhang, J., Luo, G., Jia, Y., Deng, M., & Ling, Y. (2016). Facile preparation of UiO-66 nanoparticles with tunable sizes in a continuous flow microreactor and its application in drug delivery [Article]. *Microporous and Mesoporous Materials*, *220*, 148-154. https://doi.org/10.1016/j.micromeso.2015.08.037

Tatsuma, A., & Aono, M. (2016). Food image recognition using covariance of convolutional layer feature maps. *IEICE TRANSACTIONS on Information and Systems*, *99*(6), 1711-1715.

Tayal, A., Chen, Y., Song, C., Hiroi, S., Kumara, L., Palina, N., . . . Sakata, O. (2018). Local Geometry and Electronic Properties of Nickel Nanoparticles Prepared via Thermal Decomposition of Ni-MOF-74 [Article]. *Inorganic Chemistry*, *57*(16), 10072-10080. https://doi.org/10.1021/acs.inorgchem.8b01230

Tcholakova, S., Denkov, N., & Lips, A. (2008). Comparison of solid particles, globular proteins and surfactants as emulsifiers. *Physical Chemistry Chemical Physics*, *10*(12), 1608-1627.

Tian, C., Asghar, S., Xu, Y., Chen, Z., Zhang, J., Ping, Q., & Xiao, Y. (2018). Tween 80-modified hyaluronic acid-ss-curcumin micelles for targeting glioma: Synthesis, characterization and their in vitro evaluation [Article]. *International Journal of Biological Macromolecules*, *120*, 2579-2588. https://doi.org/10.1016/j.ijbiomac.2018.09.034

Tikekar, R., Pan, Y., & Nitin, N. (2013). Fate of curcumin encapsulated in silica nanoparticle stabilized Pickering emulsion during storage and simulated digestion [Article]. *Food Research International*, *51*(1), 370-377. https://doi.org/10.1016/j.foodres.2012.12.027

Valenzano, L., Civalleri, B., Chavan, S., Bordiga, S., Nilsen, M., Jakobsen, S., . . . Lamberti, C. (2011). Disclosing the Complex Structure of UiO-66 Metal Organic Framework: A Synergic Combination of Experiment and Theory [Article]. *Chemistry of Materials*, *23*(7), 1700-1718. https://doi.org/10.1021/cm1022882

Wang, P.-L., Xie, L.-H., Joseph, E. A., Li, J.-R., Su, X.-O., & Zhou, H.-C. (2019). Metal–Organic Frameworks for Food Safety. *Chemical reviews*, *119*(18), 10638-10690.

Wang, S., McGuirk, C. M., d'Aquino, A., Mason, J. A., & Mirkin, C. A. (2018). Metal–organic framework nanoparticles. *Advanced Materials*, *30*(37), 1800202.

Wei, Y., Sun, C., Dai, L., Mao, L., Yuan, F., & Gao, Y. (2019a). Novel Bilayer Emulsions Costabilized by Zein Colloidal Particles and Propylene Glycol Alginate, Part 1: Fabrication and Characterization [Article]. *Journal of Agricultural and Food Chemistry*, *67*(4), 1197-1208. https://doi.org/10.1021/acs.jafc.8b03240

Wei, Y., Sun, C., Dai, L., Mao, L., Yuan, F., & Gao, Y. (2019b). Novel Bilayer Emulsions Costabilized by Zein Colloidal Particles and Propylene Glycol Alginate. 2. Influence of Environmental Stresses on Stability and Rheological Properties [Article]. *Journal of Agricultural and Food Chemistry*, *67*(4), 1209-1221. https://doi.org/10.1021/acs.jafc.8b04994

Wei, Z., Wang, C., Liu, H., Zou, S., & Tong, Z. (2012). Halloysite nanotubes as particulate emulsifier: Preparation of biocompatible drug-carrying PLGA microspheres based on pickering emulsion [Article]. *Journal of Applied Polymer Science*, *125*, E358-E368. https://doi.org/10.1002/app.36456

Winarta, J., Shan, B., Mcintyre, S. M., Ye, L., Wang, C., Liu, J., & Mu, B. (2019). A decade of UiO-66 research: a historic review of dynamic structure, synthesis mechanisms, and characterization techniques of an archetypal metal–organic framework. *Crystal Growth & Design*, *20*(2), 1347-1362.

Wu, C., Liang, Y., Hu, W., Yuan, M., Bai, X., Liu, F., . . . Haick, H. (2019). Interface-Regulated Contact Electrification for Power-Free and Highly Selective Gas Sensing. *Advanced Intelligent Systems*, *1*(6), 1900066.

Wu, H., Chua, Y. S., Krungleviciute, V., Tyagi, M., Chen, P., Yildirim, T., & Zhou, W. (2013). Unusual and highly tunable missing-linker defects in zirconium metal–organic framework UiO-66 and their important effects on gas adsorption. *Journal of the American Chemical Society*, *135*(28), 10525-10532.

Wu, M., & Yang, Y. (2017). Metal-Organic Framework (MOF)-Based Drug/Cargo Delivery and Cancer Therapy [Article]. *Advanced Materials*, *29*(23), Article ARTN 1606134. https://doi.org/10.1002/adma.201606134

Wu, Y., Luo, Y., Zhou, B., Mei, L., Wang, Q., & Zhang, B. (2019). Porous metal-organic framework (MOF) Carrier for incorporation of volatile antimicrobial essential oil [Article]. *Food Control*, *98*, 174-178. https://doi.org/10.1016/j.foodcont.2018.11.011

Xiao, J., Lo, C., & Huang, Q. (2015). Kafirin Nanoparticle-Stabilized Pickering Emulsions as Oral Delivery Vehicles: Physicochemical Stability and in Vitro

Digestion Profile [Article]. *Journal of Agricultural and Food Chemistry*, *63*(47), 10263-10270. https://doi.org/10.1021/acs.jafc.5b04385
Xiao, J., Lu, X., & Huang, Q. (2017). Double emulsion derived from kafirin nanoparticles stabilized Pickering emulsion: Fabrication, microstructure, stability and in vitro digestion profile [Article]. *Food Hydrocolloids*, *62*, 230-238. https://doi.org/10.1016/j.foodhyd.2016.08.014
Xiao-wei, H., Xiao-bo, Z., Ji-yong, S., Zhi-hua, L., & Jie-wen, Z. (2018). Colorimetric sensor arrays based on chemo-responsive dyes for food odor visualization. *Trends in Food Science & Technology*, *81*, 90-107.
Xiao-wei, H., Zhi-hua, L., Xiao-bo, Z., Ji-yong, S., Han-ping, M., Jie-wen, Z., . . . Holmes, M. (2016). Detection of meat-borne trimethylamine based on nanoporous colorimetric sensor arrays. *Food chemistry*, *197*, 930-936.
Xu, H., Sommer, S., Broge, N. L. N., Gao, J., & Iversen, B. B. (2019). The chemistry of nucleation: in situ pair distribution function analysis of secondary building units during UiO-66 MOF formation. *Chemistry*, *25*, 2051-2058.
Xu, Y., Tang, C., Liu, T., & Liu, R. (2018). Ovalbumin as an Outstanding Pickering Nanostabilizer for High Internal Phase Emulsions [Article]. *Journal of Agricultural and Food Chemistry*, *66*(33), 8795-8804. https://doi.org/10.1021/acs.jafc.8b02183
Yan, X., Ma, C., Cui, F., McClements, D. J., Liu, X., & Liu, F. (2020). Protein-stabilized Pickering emulsions: Formation, stability, properties, and applications in foods. *Trends in Food Science & Technology*.
Yang, M., Liu, X., Luo, Y., Pearlstein, A. J., Wang, S., Dillow, H., . . . Zhou, B. (2021). Machine learning-enabled non-destructive paper chromogenic array detection of multiplexed viable pathogens on food. *Nature Food*, *2*(2), 110-117.
Yehia, H., Pisklak, T., Ferraris, J., Balkus, K., & Musselman, I. (2004). Methane facilitated transport using copper (II) biphenyl dicarboxylate-triethylenediamine/poly (3-acetoxyethylthiophene) mixed matrix membranes. Abstracts of Papers of the American Chemical Society,
Yu, X., Wang, J., Wen, S., Yang, J., & Zhang, F. (2019). A deep learning based feature extraction method on hyperspectral images for nondestructive prediction of TVB-N content in Pacific white shrimp (Litopenaeus vannamei). *Biosystems engineering*, *178*, 244-255.
Zhang, J., Mei, L., Chen, N., Yuan, Y., Zeng, Q., & Wang, Q. (2020). Study on beta-lactoglobulin microgels adsorption onto a hydrophobic solid surface by QCM-D [Article|Proceedings Paper]. *Food Hydrocolloids*, *98*, Article UNSP 105320. https://doi.org/10.1016/j.foodhyd.2019.105320
Zhang, N., Gao, Y., Xu, X., Bao, T., & Wang, S. (2021). Hydrophilic carboxyl supported immobilization of UiO-66 for novel bar sorptive extraction of non-steroidal anti-inflammatory drugs in food samples. *Food Chemistry*, 129623.
Zhang, W., Liao, P., Lin, R., Wei, Y., Zeng, M., & Chen, X. (2015). Metal cluster-based functional porous coordination polymers [Review]. *Coordination Chemistry Reviews*, *293*, 263-278. https://doi.org/10.1016/j.ccr.2014.12.009

Zhang, Y., Feng, X., Yuan, S., Zhou, J., & Wang, B. (2016). Challenges and recent advances in MOF–polymer composite membranes for gas separation. *Inorganic Chemistry Frontiers*, *3*(7), 896-909.

Zhou, L., Zhang, C., Liu, F., Qiu, Z., & He, Y. (2019). Application of Deep Learning in Food: A Review. *Comprehensive Reviews in Food Science and Food Safety*, *18*(6), 1793-1811.

Zhu, F. (2019). Starch based Pickering emulsions: Fabrication, properties, and applications. *Trends in Food Science & Technology*, *85*, 129-137.

Zhu, X., Gu, J., Wang, Y., Li, B., Li, Y., Zhao, W., & Shi, J. (2014). Inherent anchorages in UiO-66 nanoparticles for efficient capture of alendronate and its mediated release. *Chemical Communications*, *50*(63), 8779-8782.